U.PORTO
FEUP FACULDADE DE ENGENHARIA
UNIVERSIDADE DO PORTO

U.PORTO
INSTITUTO DE CIÊNCIAS BIOMÉDICAS ABEL SALAZAR
UNIVERSIDADE DO PORTO

# Development of a novel 3D-scaffold to promote bone regeneration

**Rafaela Maria Da Silva Presa**

Dissertation for the Degree of Master of Science in Bioengineering at Faculdade de Engenharia da Universidade do Porto and Instituto de Ciências Biomédicas Abel Salazar da Universidade do Porto

Integrated Master in Bioengineering

# Development of a novel 3D-scaffold to promote bone regeneration

Rafaela Maria Da Silva Presa

Dissertation for the Degree of Master of Science in Bioengineering at Faculdade de Engenharia da Universidade do Porto and Instituto de Ciências Biomédicas Abel Salazar da Universidade do Porto

Integrated Master in Bioengineering

Supervisor: Doctor Aureliana Sousa

Co-supervisor: Doctor Marco Araújo

September 2019

*“So remember to look up at the stars and not down at your feet. Try to make sense of what you see and wonder about what makes a universe exist.*

*Be curious.*

*And however difficult life may seem, there is always something you can do and succeed at. It matters that you don’t just give up.”*

*Stephen Hawking*

*Page intentionally left in blank*

# Acknowledgments

First of all, I have to thank to my supervisor with all my heart. Thank you Filipa for your openness, your closeness, your support, your freedom, your advices, your sudden but always very accurate ideas. Thank you for being the person you are and for allowing a relationship where openness is great for sharing thoughts, ideas, moods, everything.

I could not fail to mention two other very important people who appeared with the beginning of this adventure, Marco and Filipa. Without you this way would not have been so good, full of laughter, happy moments, much help, companionship, camaraderie and friendship. Thank you for being two fantastic and wildest healthy humans there can be.

Marco, my co-supervisor, thank you for being who you are, for the good heart you are! Thank you for everything, for your help in developing my work, for all the support, for all the advices and for the good working environment that you have helped to create every day.

Filipa, thank you for being the sweet person you are. Thank you for sharing this adventure with me and always being someone with whom I could share the good and bad times. Thank you for the advices, support and all the help, but above all for the great team spirit and mutual help.

I have to thank to Manel for all the help that allowed me to develop my work and Eduardo for the support and good team spirit and work environment provided.

An acknowledgment to Susana Olhero and Paula Torres from CICECO for providing the CaP powders and the robocasting.

I have to acknowledge the support of Ricardo Vidal from the Biointerfaces and Nanotechnology i3S Scientific Platform, Maria Lázaro from the Bioimaging i3S Scientific Platform, member of the national infrastructure PPBI - Portuguese Platform of Bioimaging (PPBI-POCI-01-0145- FEDER-022122) and Daniela Silva from the Image, Microstructure and Microanalysis Unit (IMCROS) from the Materials Centre of the University of Porto (CEMUP).

All this, to end by thanking two of the most important people in my life - my parents. Thank you, mom and dad, for all understanding, support, affection, open mind and help. Without you, that wouldn't be possible.

The research described in this thesis was financially supported in the framework of FCT- Fundação para a Ciência e Tecnologia *project 2BBone - Sintering-free*

*Bifunctional CaP-based Biomaterials for Bone Cancer Treatment and Regeneration* (PTDC/CTM-CER/29940/2017

# Abstract

Bone Engineering has been one of the most explored and successful fields of research on Tissue Engineering (TE). Besides trauma lesions and bone infections, also several diseases such as Osteoporosis and Bone Cancer significantly affect the functionality of the tissue thus impairing bone intrinsic regeneration ability. The appearance of large defects on bone tissue and the occurrence of fractures can result in a negative impact on quality of life of the patients, with a lot of co-morbidities associated. Considering the composition of natural bone, one of the approaches that has emerged as a successful alternative are scaffolds resulting from the combination of polymers, which act as a support matrix, with ceramic powders, which provide similar properties to the mineral phase of bone.

Such biomaterials can be explored due to their characteristics such as biodegradability profile, bioactivity and osteoconductive properties. With the rise of advanced additive manufacturing technologies such as robocasting, 3D porous scaffolds can be tailored to the specific need of each patient. With this technique is possible to produce a highly ordered and interconnected macroporous structure, which was demonstrated to be essential to provide the ideal conditions that allow the local delivery of cells, growth factors, drugs as well as providing the ideal mechanical properties for a load-bearing tissue such as bone.

In this work, we were able to test *in vitro* stability of a scaffold composed of chitosan and a biphasic powder of Hydroxyapatite (HA) and β-Tricalcium Phosphate (β-TCP) as well as the influence of the application of specific magnetic conditions on human Mesenchymal Stem Cells (hMSCs) behavior. The *in vitro* stability and also the mechanical properties were altered after sterilization process rendering scaffold with properties that were not ideal. We then developed an alternative strategy using a biphasic powder of HA and β-TCP in combination with Konjac Glucomannan (KGM) to produce a 3D-scaffold through robocasting. KGM is a natural polysaccharide which is nontoxic, biodegradable, biocompatible, has good film-forming ability and also displays interesting viscoelastic properties for the use in 3D printing systems. Furthermore, it can be chemically functionalized with specific moieties which represents an important advantage for the design of a multi-functional scaffold.

Our results show that this newly developed strategy renders non-sintered 3D scaffolds which are cytocompatible, stable under *in vitro* conditions, allows the

adherence and proliferation of hMSC. Although further studies are needed, these scaffolds proved to be able to allow hMSCs differentiation into the osteogenic lineage and there is some indication that may display osteoinductive properties. We were also able to functionalize KGM with dopamine as a proof-of-concept to future hyperthermia induction approaches. As an alternative strategy, polydopamine particles have also been successfully synthesized for future incorporation in the scaffolds.

Altogether, the results obtained in the scope of this thesis, suggest that this newly developed hybrid organic-inorganic scaffold is a promising candidate to be used on biomedical engineering approaches.

*Page intentionally left in blank*

# List of Contents

# Abbreviation List

3D - Three-Dimensional
ALP - Alkaline Phosphatase
AM - Additive Manufacturing
ATR-FTIR - Attenuated total reflection - Fourier-transform infrared spectroscopy
BCA – Bicinchoninic acid
BCP - Biphasic Calcium Phosphate
BM – Basal Medium
BTE – Bone Tissue Engineering
BSA - Bovine Serum Albumin
CAD - Computer Aided Design
CaP - Calcium Phosphate
DAPI - 4',6-diamidino-2-phenylindole
DMEM - Dulbecco's Modified Eagle Medium
DMSO - Dimethyl sulfoxide
DNA - Deoxyribonucleic Acid
DWA – Direct Write Assembling
ECM - Extracellular Matrix
EDC - 1-(3-Dimethylaminopropyl)-3-ethylcarbodiimide hydrochloride
EDTA – Ethylenediamine tetraacetic acid
EM – Expansion Medium
FBS - Fetal Bovine Serum
GO – Graphene Oxide
HA – Hydroxyapatite
hDNFs – human Dermal Neonatal Fibroblasts
hMSCS – human Mesenchymal Stem Cells
$^{1}$H-NMR – Proton Nuclear Magnetic Resonance
ISO - International Organization for Standardization
KGM – Konjac Glucomannan
α-MEM - α-Minimum Essential Medium
MES - 2-(N-morpholino) ethanesulfonic acid
MNPs – Magnetic Nanoparticles
NIR – Near Infrared Region

NHS - N-Hydroxysuccinimide

PBS - Phosphate-Buffered Saline

PFA – Paraformaldehyde

PMMA - Polymethylmethacrylate

PS - Particle Size

PSD - Particle Size Distribution

PVA – Polyvinyl Alcohol

P/S – Penicillin/Streptomycin

RPM – Rotations per minute

RT - Room Temperature

SAC0 – Succinic Anhydride

SEC – Size exclusion chromatography

SEM - Scanning Electron Microscopy

SDS – Sodium dodecyl sulfate

TCP - Tricalcium Phosphate

TE – Tissue Engineering

TEM – Transmission electron microscopy

UV-Vis - Ultraviolet–visible spectroscopy

XRD - X-Ray Diffraction

# List of Figures

# List of Tables

*Page intentionally left in blank*

# Introduction

## 1. Bone Tissue – Organization and Composition

The human body is composed by a multiplicity of cells that form different types of tissues [1], [2]. Bone is composed of a highly specialized form of connective tissue whose primary functions are to provide mechanical support for muscular activity (thus allowing locomotion), physical protection of organs and soft tissues, storage facility for systemic mineral homeostasis (inorganic ions such as calcium), as well as harboring the bone marrow [2].

### 1.1 Bone Organization

Morphologically, the bone of the mature skeleton consists of cortical (or compact) bone (80%) and cancellous (or trabecular) bone (20%). In cortical bone, densely concentric lamellae are formed by packed collagen fibril. Cancellous bone has a loosely organized, porous matrix (Figure 1) [3].

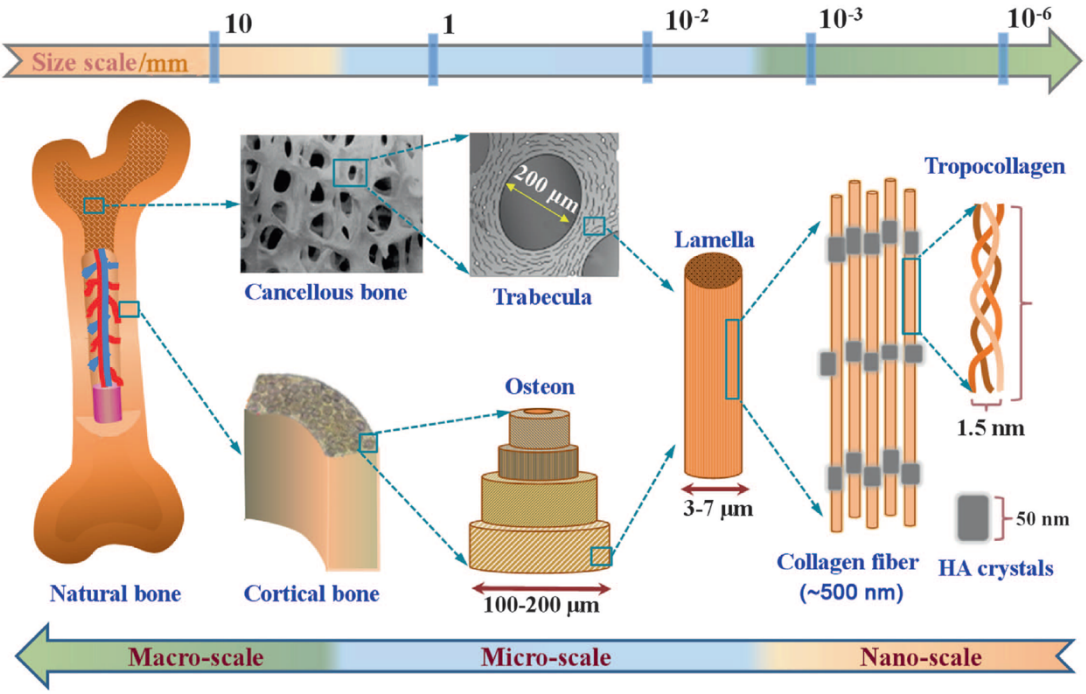


**Figure 1 – The chemical composition and multi-scale structure of natural bone.** Bone is constituted by cortical bone, the densest tissue that is organized in concentric lamellae. The cancellous bone has a porous matrix. These structural differences lead to distinct function: Cortical bone provides mechanical and protective functions and cancellous bone provides metabolic functions. At a nano-scale is possible verify the two main components of the bone – Collagen – organic matrix and Hydroxyapatite – inorganic matrix. Retrieved from [4].

Structural and functional differences between cortical and cancellous bone are related to their primary functions. Cortical bone provides mechanical and protective functions and cancellous bone provides metabolic functions [3]. The distribution of the two types of bone tissue is different in the human skeleton, depending, primarily, on the principal function of the bone in question [1].

## 1.2 Bone Composition

### 1.2.1 Extracellular matrix

Bone extracellular matrix is composed of 5% of water, approximately 70% of crystals of calcium phosphate for structural reinforcement and stiffness, (inorganic phase) and 25% of proteins that together with 2% of lipids constitute the organic phase that provides flexibility and toughness to bone [5]. The inorganic phase is mainly constituted by Hydroxyapatite crystals ($Ca_{10}(PO_4)_6(OH)_2$) since calcium and phosphate ions combine in a process of nucleation, but significant amounts of bicarbonate ($HCO_3^-$), sodium ($Na^+$), potassium ($K^+$), citrate ($C_6H_5O_7^{3-}$), magnesium ($Mg^{2+}$), carbonate ($CO_3^{2-}$), fluoride ($F^-$), zinc ($Zn^{2+}$), barium ($Ba^{2+}$), and strontium ($Sr^{2+}$) ions are also present. Together with collagen, the noncollagenous matrix proteins form a scaffold for hydroxyapatite deposition. Hydroxyapatite gives to bones their hardness, resistance and strength, while the collagen fibers give them flexibility, that they are not brittle [1], [2].

The organic matrix is composed by collagenous proteins (90%), predominantly type I collagen, and noncollagenous proteins including osteocalcin, osteonectin, osteopontin, fibronectin and bone sialoprotein II, bone morphogenetic proteins (BMPs) and growth factors. There are also small leucine-rich proteoglycans [6]. In contrast with another tissues, bone tissue is poor in cells. The small number of cells is entrenched in a fibrous collagen rich matrix which forms a surface for the adherence of the inorganic salt crystals and have a crucial role in the maintenance of a healthy and functional tissue [1].

### 1.2.2 Cells

Although the cells represent a small volume of the bone tissue, it is constituted by four types of cells: osteoblasts, osteoclasts, osteocytes and bone lining cells [1], [2].

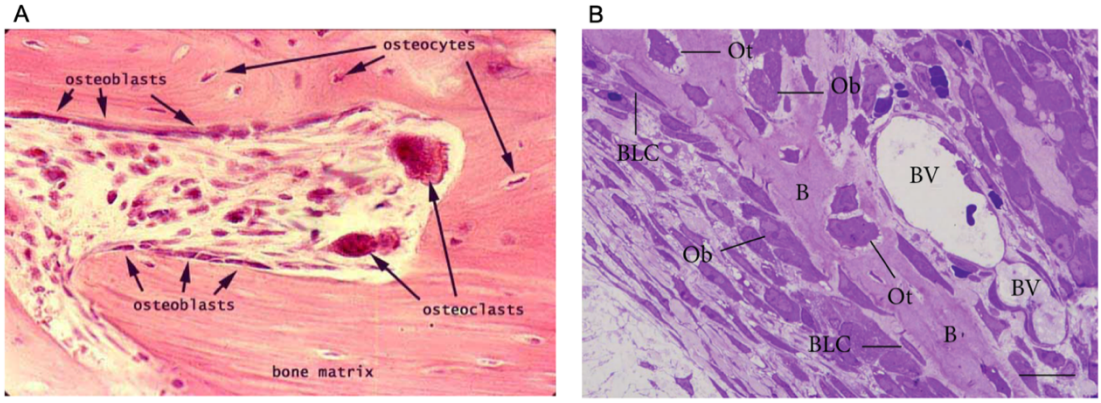


**Figure 2 – Micrographs of bone portions.** A – On this histological image, osteoblasts are visible on the surface of the bone matrix, together with giant osteoclasts. Osteocytes are visible entrapped on the bone matrix. B – On this image a portion of a bony trabecula (B) is observed with Osteoblasts (Ob) and bone lining cells (BLC) present on bone surface while osteocytes (Ot) are observed entrapped in the bone matrix. Blood vessels (BV) are visible, too. Retrieved from [2], [7].

Osteoblasts are cuboidal differentiated cells found on the surface of new bone (Figure 2) responsible for the production of the extracellular matrix (ECM) of bone, and its subsequent mineralization process. Osteoblasts produce the organic matrix of bone (osteoid). Some of the osteoblasts become trapped in the lacunae within the matrix of bone and differentiate into osteocytes. Old osteoblasts become inactive, thin and elongated lining cells which lies on the bone surface. The repair process and formation of new bone requires the differentiation and the proliferation of osteoblasts [8].

The osteocyte is a mature osteoblast represent 90% of bone cells in the skeleton of an adult human [8]. They are uniform in shape and size that can be found inside the bone matrix (Figure 2) and is responsible for its maintenance, through the growth of new arms on the cell and the packing of osteoblasts and osteoclasts, they become responsible for communication between other analogous cells and bone lining cells by developing long branches, forming a wide network of intercellular communication. Osteocytes also have mechanosensitive functions since they can detect mechanical pressure allowing the adaptation of bone to daily mechanical forces. By this way, these cells seem to act as orchestrators of bone remodeling, through regulation of osteoblast and

osteoclast activities. Moreover, a chemotactic signal to osteoclastic bone resorption is the osteocyte apoptosis [2].

Bone lining cells are flat, elongated, inactive cells that cover bone surfaces that are undergoing neither bone formation nor resorption (Figure 2B). Little is known regarding the function of these cells; however, it has been speculated that bone lining cells can be precursors for osteoblasts and participate in osteoclast differentiation [2], [8].

Osteoclasts originate from hematopoietic stem cells, they are large multinucleated cells, responsible for resorbing the mineralized bone matrix and they move from different locations on the bone surface dissolving the bone (Figure 2A) [8].

## 1.3 Bone Remodeling

Bone is a highly dynamic tissue. Due to this particular characteristic, bone is being continuously remodeled [2]. As described above, the cells of the bone tissue interact intensively. Moreover, the osteoclasts not only are responsible for the bone resorption, but for the bone formation. Osteoclasts have the capability to communicate with osteoblasts – through the release of coupling factors - in a crosstalk that regulates the local recruitment and bone forming activity of osteoblasts [2], [9].

The bone remodeling cycle (Figure 3) is a highly complex process where there is a very important crosstalk between all the components of the tissue to ensure this process [9]. There are direct and indirect communication among the cells, as well as between the cells with the matrix through the release of several factors. This process is known by coupling process and the factors involved are designated by coupling factors [2].

Bone matrix not only acts as a support for bone cells and to the inorganic phase, but can also release several molecules that interfere in the bone cells activity and, consequently, has a participation in the bone remodeling. The molecules involved are, predominantly, adhesion molecules, such as integrins [10], [11].

Without the interaction between the bone matrix and the osteoclasts, the resorption process doesn't occur [11], [12]. Another important aspect is the role

of the integrins in the interaction osteocyte-bone matrix. These interactions are essential for the function of these cells, whereby signals induced by tissue deformation are generated and amplified [13].

Then, the remodeling process occurs due to the coordination actions of osteoblasts, osteoclasts, osteocytes, bone lining cells and the bone matrix [14].

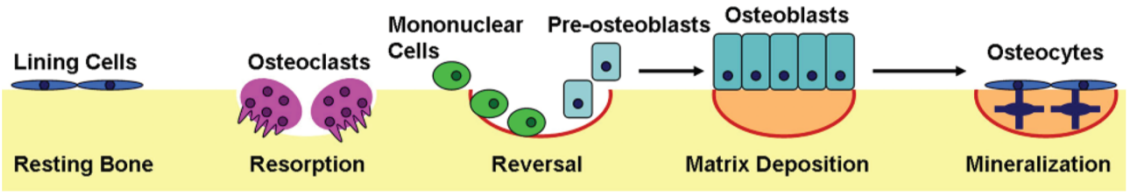


**Figure 3 – Bone remodeling cycle**. Bone remodeling begins when osteoclasts resorb bone mineral and matrix. Mononuclear cells prepare the resorbed surface for osteoblasts, which generate newly synthesized matrix as they differentiate. Matrix mineralization and the differentiation of some osteoblasts into osteocytes completes the remodeling cycle. Adapted from [15].

The remodeling process starts with the action of the osteoclasts, mediated by osteoclastogenic factors, that initiate bone resorption (Figure 3). During this phase, osteoclasts release some factors that inhibit the activity of the osteoblast in order to completely remove the damaged or aged bone tissue. After this phase, coupling factors and matrix-derived factors are released and with that the recruitment of osteoblasts and their differentiation is locally controlled by osteoclasts and bone matrix. At this time bone formation occurs (Figure 3).

This particular characteristic of the bone tissue is very important for the maintenance of the bone volume and bone balance [16]. Moreover, the dynamic of the bone is essential for fracture healing, skeleton adaptation to mechanical use and calcium homeostasis [2].

However, when an imbalance between bone resorption and bone formation occurs several bone diseases can appear. Thus, an equilibrium between these two process is necessary and, as previously described, it depends a lot on the action of several components and factors [14], [17].

## 1.4 Bone-related therapeutic needs

There are different diseases affecting the bone tissue, that leads to alterations in the bone remodeling process or are in fact a consequence of the impaired balance between these processes.

Between them, hip fracture is the most devastating type of fracture because it is associated with increased morbidity and mortality rates. Within one year of a hip fracture, 40% of patients are unable to walk independently, 60% need assistance with at least one essential activity of daily living (dressing, bathing) and 80% are unable to perform an instrumental activity of daily living, such as driving or housecleaning. In the same period of time, 14-36% of the patients die. When the fracture occur the risk of death is higher [18].

When multiple fractures occur, the patient can develop kyphosis (i.e. vertebral deformities), abdominal protrusion and a loss of >1.5 in of mature height. Respiratory problems and poor nutritional habits may occur due to thoracic and abdominal compression, respectively [18]. All of these aspects are physical and functional components that dramatically impact the quality of life of the patient. Moreover, an emotional component can be added. Depression and anxiety are typical symptoms revealed by the patients that suffer from skeletal-related events [19].

When an imbalance between the activity of osteoblasts and osteoclasts occurs, the situations that can appear and cause more impact are: bone destructions exceed bone formation or vice-versa (Figure 4).

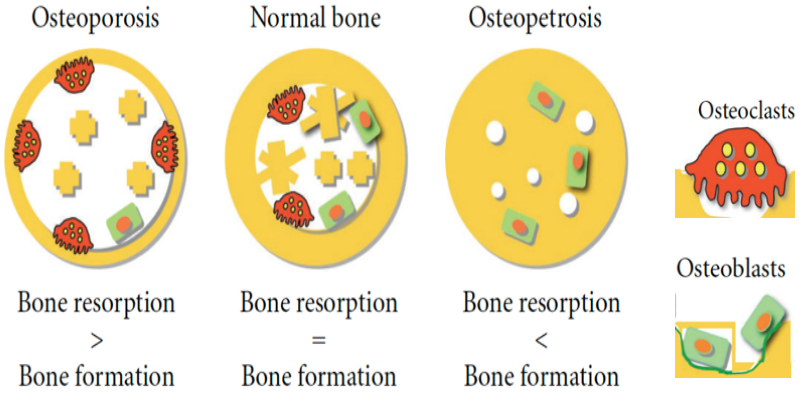


**Figure 4 - Balance of bone resorption and bone formation**. If the balance between bone formation and resorption is lost by the uncontrolled production of regulators, bone structure would be strikingly damaged and the subject would be susceptible to osteoporosis. Adapted from [20].

When bone resorption is excessive, without the corresponding amount of new formed bone different causes can be behind. Diseases, such as osteoporosis, periodontitis, Paget's disease, bone cancer and inflammatory disease lead to the described alteration in the bone homeostasis [1], [2], [18], [21].

These diseases have distinctive causes but, in terms of bone tissue, they lead to the same panorama: loss of bone mass and density. Then, there is a very high risk of fracture, multi-fractures can occur at the same time, impaired healing of the fracture and large defects on bone tissue, namely when the cause is a trauma or some type of cancers (Figure 5) [2], [9], [16], [18], [22].

The occurrence of fractures in a frequent manner compromises a lot the daily life of these patients. Moreover, the complications associated with the healing of the fractures increase the morbidities and, inclusively, the mortality of the patients [18], [19], [22].

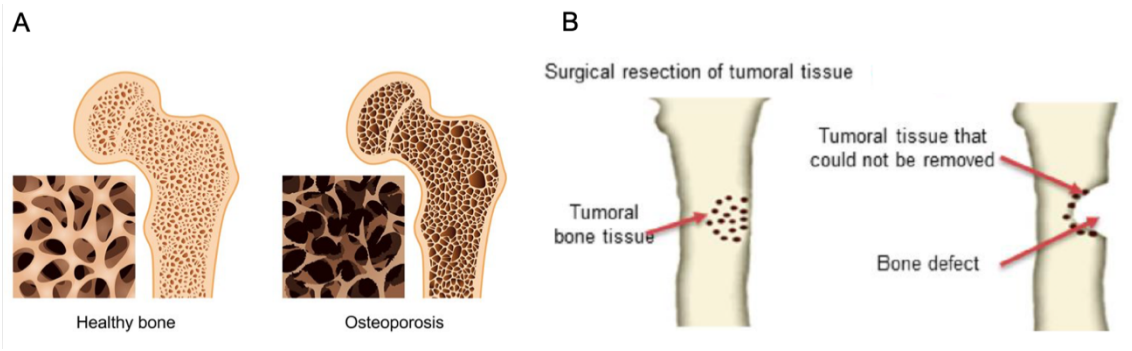


**Figure 5 - Defects on bone tissue.** A) Osteoporosis – A progressive loss of bone mass leads to changes in bone structure that can result in fractures. B) Bone cancer – The remotion of the tumor mass leads to the appearance of defects on bone tissue. Moreover, there are the problem of cancer cells remain on the tumor site and the recurrence of the tumor can occur. Adapted from [23], [24].

Osteopetrosis is a rare bone disease, where genetic mutations affect the resorption activity of the osteoclasts and new bone tissue starts accumulate in a disproportional manner [2].

When certain types of cancer affect a person, the skeletal system will be affected too. In the particular case of cancer, the surgical procedure of tumor's resection leads to the appearance of big defects, that the bone by itself doesn't have the capability of regenerate (Figure 5B) [9], [16], [25], [26]. Then, the bone tissue stays fragilized and the risk of fractures or infections highly increase. In these cases, the loss of bone mass is higher than in other pathologies and occurs more rapidly. Moreover, due to the anti-cancer therapies that are administrated to these patients, the healing process becomes more difficult [18], [22].

However, for these patients there is an extra problem. There is always the problem of the recurrence of the tumor [25]–[28]. As mentioned before, these patients are the ones who present the major bone defects. This is mainly

because, nowadays there aren't a consensus on the clinical field about the concept of clear margins – the amount of healthy tissue in the neighborhood of the tumor that have to be removed to avoid the recurrence of the tumor. There are a lot of physicians that suggest a radical position, meaning the removal of high amounts of healthy tissue that is surrounding the tumor [29].

All the diseases that affect the bone tissue compromise its regenerative capability. In these situations, the ability of mesenchymal stem cells to differentiate into osteoblasts and form new bone is reduced [22]. As a result, there is a huge need to develop solutions in order not only to treat the background disease, but also to promote the regenerative bone process.

In the case of bone cancer, rather than advances in the promotion of bone tissue regeneration, new solutions are needed to eliminate the problem of recurrence of the tumor and thus to end the non-unanimity of medical opinions.

## 2. Bone healing- traditional approaches

Currently, the most used strategy is the use of bone grafts to fill space left by the fracture/tumor and to enhance healing. As first option and considered the gold standard are the autografts (bone harvest from the patient) followed by the allografts (donor bone) [9], [22], [30].

An autograft combine all the properties required in a bone graft material: it is osteoinductor (with the release of bone morphogenetic proteins and other growth factors), osteogenic (osteoprogenitor cells) and osteoconductive (scaffold) [30]. However, there are limitations associated to the use of bone grafts. Harvesting requires an additional surgical procedure that is an additional morbidity, with well-documented complications and discomfort for the patient. Furthermore, their availability is always limited [9], [22], [30]. Regarding the allograft, the problem of potential transmission of pathogens and rejections is the principal limitation [9], [22], [30]. Using the bone grafts strategy, the surgery is the cornerstone of the treatment and there are risk of secondary complications, such as infection and thromboembolism [22]. Moreover, the fractures frequently do not heal, may require multiple surgeries and frequently re-fracture the same site. Because of that, the treatment of these fractures is still a challenging, namely due

to the diminished capacity for fracture healing [22]. Therefore there is still a strong need to develop bone graft substitutes to avoid these limitations [9].

More limited are the patients that suffer of bone cancer. Currently, these patients are treated with two different therapies. These patients have to undergo to cycle(s) of chemotherapy and radiotherapy, in order to avoid the recurrence of the tumor. This therapy is a systemic therapy with a lot of side effects [25]–[27]. All of the solutions mentioned above are applied in patients to promote the regeneration of the bone. However, these patients need solutions that will have to undergo beyond the promotion of bone regeneration.

The bone graft substitutes are generating great interesting as alternatives to autologous or allogeneic bone grafts. They consist of scaffolds made of synthetic or natural biomaterials that promote the migration, proliferation and differentiation of bone cells for bone regeneration [30].

## 3. Tissue Engineering based approaches

Tissue engineering (TE) is an exciting and multidisciplinary field with the objective of developing biological substitutes to restore, replace or regenerate tissue form and function. Cells, scaffolds and growth factors are generally referred to as the main components of TE (Figure 6). Scaffolds provide the three-dimensional structural support for cell attachment and subsequent tissue development, in a favorable biological environment for the growth and differentiation of cells [31].

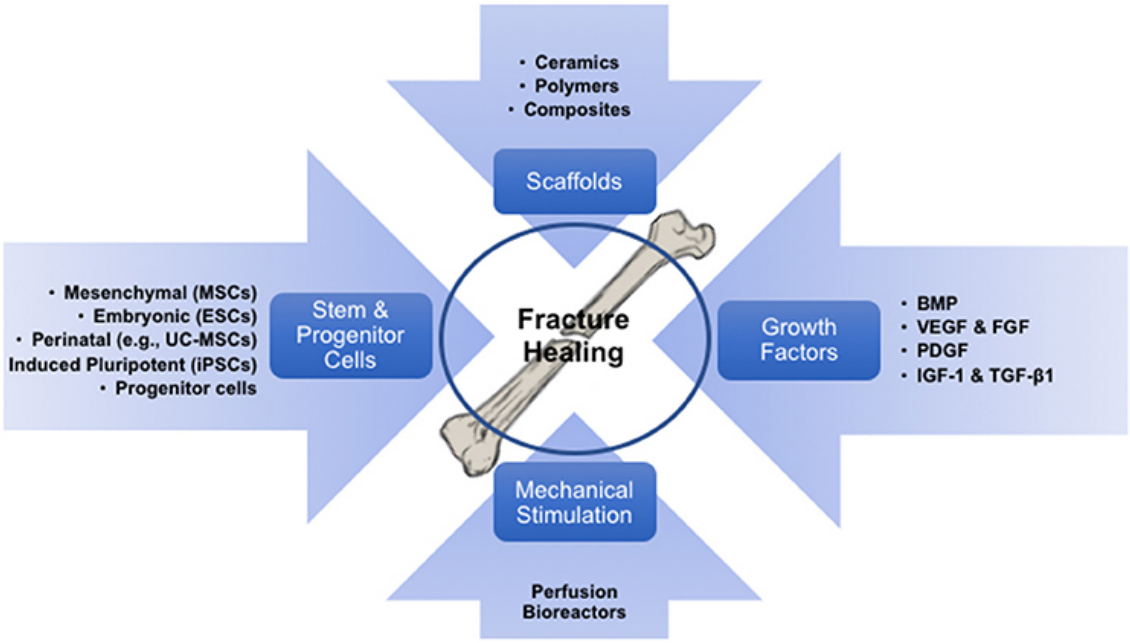


**Figure 6 - Tissue Engineering approach on Bone Tissue.** Diagram illustrating the concept of skeletal tissue regeneration via scaffold-based tissue engineering strategies, involving its components (cells, biomaterials/scaffolds and growth factors), and the required exposure to mechanical environments to pre-conditioning the engineered implants. Retrieved from [32].

Approaches of TE are currently trying to achieve the gold standard solution needed for bone regeneration. The development of 3D porous scaffolds is one of the most promising biomaterial-based strategies for bone defect regeneration. The interconnected macropores are essential to supply sufficient space for cellular activity, nutrient transport and cell-cell interactions [28].

There are three essential elements required for bone tissue engineering: osteogenic cells, growth factors and a scaffold matrix that possesses all the characteristics necessary for new bone growth, i.e. (i) osteoconductivity (passive scaffold to promote vascular ingrowth and bone apposition), (ii) osteogenicity (containing osteoprogenitor cells) and (iii) osteoinductivity (provide signals to induce osteogenic differentiations of local stem cells) [33]–[36].

Because of that, the main principle of Bone Tissue Engineering (BTE) strategy is to seed cells in an artificial 3D porous matrix (Figure 7), working as a scaffold to sustain cell proliferation, differentiation and to provide guidance for tissue regeneration and growth. After implantation the natural tissue regeneration process will ideally take place, integrating the implant, leading to vascularization. The structure of the scaffold dissolves while new tissue is formed in its place [37].

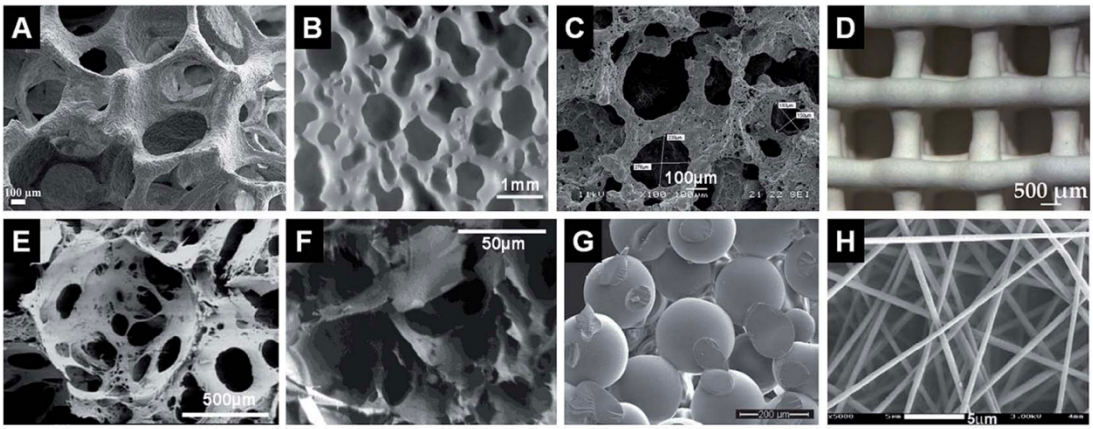


**Figure 7 – Different types of porous scaffolds used in BTE.** Representative internal structures of porous scaffolds produced via (A) polymer sponge replication, (B) impregnate sintering, (C) gel-cast foaming, (D) solid free-form fabrication, (E) solvent casting and particulate leaching, (F) phase separation, (G) microsphere sintering and (H) electrospinning. Retrieved from [38].

## 3.1 Materials/ Biomaterials

To produce the matrix/scaffold there is a wide range of biomaterials such as collagen, hydroxyapatite (HA), β-tricalcium phosphate (β-TCP), calcium-phosphate cements and glass ceramics [30].

However, the range of materials that can be used is much higher. The materials used in BTE can be classified according two aspects: chemical composition and biological behavior. In relation to the chemical composition the materials can be subdivided in ceramics, metals, polymers, and composites, with varied degree of bioactivity. Therefore, biomaterials can be classified into four categories according to the nature of their interaction with the surrounding tissue: a) bioinert, their implantation on the body do not cause any reaction or interaction with the biological tissue, meaning that the host won´t recognize them as a strange body (ex: titanium, zirconia and alumina); b) biotolerant, they are moderately accepted by the recipient tissue which encapsulates the implant with a fibrous interface (ex: stainless steel, glass, chromium-cobalt fibers and polymethylmethacrylate (PMMA)); c) bioactive, they may cause a reaction or have an effect on the living environment, also due to their composition are capable of forming a direct link with the tissue (ex: hydroxyapatite, bioactive glasses); d) biodegradable/reabsorbable, those that suffer of slow degradation and gradual substitution of the host tissue (ex: tricalcium phosphate and bioactive glass) [39].

### 3.1.1 Calcium Phosphates

The materials that are used in bone regeneration should be the most similar to the natural composition of the tissue and mimic very well its structure and properties [9]. This aspect is critical on a tissue like bone, because the material that is used will highly influence the bone remodeling process [16]. Because of that, calcium phosphates (CaPs) are widely used. Their composition is similar to the mineral phase of bone and they have some key bone properties, such as biodegradability, bioactivity and osteoconductivity [9].

CaPs can be HA, β-TCP or an intimate mixture between the both, that is designated as biphasic calcium phosphate (BCP) [9]. The different types of BCPs differ one from another in the ratios of HA and β-TCP that constitute the mixture [9]. Depending on the desired effect, this difference between BCPs is crucial to the successful performance of the material. It is demonstrated that the composition of the CaP material has direct consequences on its performance, including its ability to be resorbed by osteoclasts, affecting osteoclast differentiation and activity [9], [16].

β-TCP exhibits excellent biodegradability and osteoconductivity, it can be resorbed by osteoclastic cells and subsequently replaced by new bone formation via osteoblasts [16]. On the other hand, HA has good biocompatibility but poorer resorption characteristics, meaning that HA is relatively stable in a bone defect due to slower bone remodeling kinetics [16]. Therefore, the chemical composition of CaPs affects the crosstalk between osteoclasts and osteoblasts and as a result, a scaffold containing these components should have important roles in the induction of the remodeling process. Even though this type of scaffolds should demonstrate effects on the bone regeneration process, there are some components, such as metallic ions, graphene oxide (GO) and polydopamine, that are being added to the scaffolds to enhance bone tissue regeneration. Metallic ions that are being used are gold, iron oxide (magnetite) and silver [25], [26], [28], [40], [41].

Although calcium phosphate materials have excellent characteristics, when applied to bone regeneration they need a “carrier” to act as the structural base of the scaffolds and improve their mechanical properties [42]. As a result,

the hybrid ceramic-polymer/hydrogel materials are emerging as ideal materials to be used on BTE [43].

### 3.1.2 Polymers

Polymers and their composites are considered as the most promising candidate materials to be used as scaffolds for bone regeneration (Table 1). Their advantageous biocompatibility and biodegradability over most metals and ceramics makes of them very attractive materials. More importantly, polymers possess highly flexible design capacity and their various properties can be easily tailored to meet specific requirements through manipulating their chemical compositions and structures. Moreover, polymers have been widely used in BTE due to their similarity with extracellular matrices [44].

**Table 1 –** Examples of commonly used polymers for BTE. Retrieved from [44].

| Polymer | Characteristics |
|---|---|
| Collagen | Major component of natural bone tissue. Excellent biocompatibility and cell-binding properties. Relatively weak mechanical stiffness and rapid bidegradation rate. Some crosslinking agents can be toxic |
| Gelatin | Denaturalized form of collagen. Similar properties as collagen |
| Silk fibroin (SF) | Structural protein of silk fibers. Flexible processibility, high mechanical strength and thermal stability. Easy chemical modification. May contain residue contaminant which can cause biocompatibility issue |
| Chitosan | Positively charged polysaccharide. Good biocompatibility. Antibacterial properties. Relatively weak mechanical strength and stability |
| Alginate | Negatively charged polysaccharide. Adjustable mechanical and biological properties by varying the content of two monomers. Crosslinkable and injectable. Relatively difficult to sterilize and to handle |
| Hyaluronic acid (HA) | Negatively charged glycosaminoglycan. Soluble in water. Good biocompatibility. Easy manipulation. Can be crosslinked to form hydrogel |
| Poly(lactic acid) (PLA), poly(glycolic acid) (PGA), and copolymer PLGA | Aliphatic polyesters. Approved by FDA for various clinical uses. Tunable physical and mechanical properties by adjusting the copolymer ratio. Possible adverse tissue reactions due to acidic degradation products. Hydrophobic and lack of cellular adhesion |
| Polycaprolactone (PCL) | High crystallinity and good mechanical strength. Slow degradation rate (years). Poor water wettability and lack of cell adhesion |
| Poly(vinyl alcohol) (PVA) | Polyalcohol synthesized by hydroxylation of polyvinyl acetate. Tunable water solubility and crystallinity by changing hydroxylation degree |
| Poly(propylene fumarate) (PPF) | Possess multiple unsaturated double bonds. Crosslinkable *in situ* and injectable. Variable mechanical properties and degradation rate. Crosslinking agents can be toxic |
| Polyurethane (PU) | Remarkable mechanical properties. Broad and variable range of mechanical, biological and physical properties |

#### 3.1.2.1 Chitosan

Chitosan is one of the most well-known natural polymer and nowadays is widely used in different areas, alongside other polymers like hyaluronic acid, alginate, agar, polyvinyl alcohol (PVA) and poly (ethylene glycol) [45]. Chitosan is used because of its bioactivity, non-toxicity, biocompatibility, biodegradability

and low-allergenicity [40], [46]–[48]. Moreover, chitosan and its derivates showed to have improved physical properties such as high surface area, porosity, tensile strength and conductivity. In addition, they can be easily molded into different shapes and forms (films, fibers, sponges, beads, powder, gel and solutions) [48].

Chitosan-based biomaterials are a popular target for tissue engineering. They have certain mechanical and structural properties for providing the proper functioning of the repaired tissues. For example, Chitosan-â-tricalcium phosphate composite exhibited efficacy in enhancing osteogenesis, vascularization and repair of bone defects in combination with mesenchymal stem cells [48].

#### 3.1.2.2 Konjac Glucomannan

Konjac Glucomannan (KGM) is an essential natural polysaccharide and the main component of the roots and tubers of the Amorphophallus konjac plant (Figure 8A-B). KGM comprises a back-bone chain of glucose and mannose monomers in a molar ratio of 1:1.6 with ~5–10% acetyl-substituted residues at the side C-6 position. It has a highly branched chain (Figure 8D) [49].

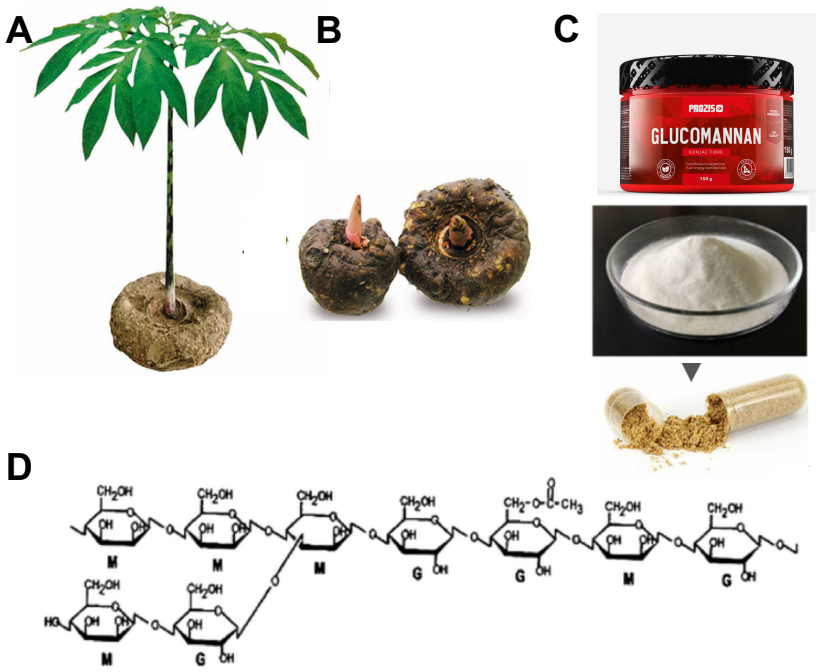


**Figure 8 - Konjac Glucomannan.** A) and B) Plant and roots of the Amorphophallus konjac plant from where the polymer is extracted; C) KGM in powder formulation used in different areas, namely food industry; D) Chemical structure of KGM. Adapted from [50], [51].

Due to its demonstrated healthy benefits such as improvement of glucose metabolism, regulation of lipid metabolism, promotion of intestinal activity and

cholesterol reduction, the applications of this polymer have widely increased (Figure 8C). Moreover, KGM is identified as a safe material by the Food and Drug Administration [49]. Since KGM has characteristic high viscosity, good water imbibing, biocompatibility, biodegradability, non-toxic and excellent gelling film forming, it is widely used in food, chemical, medical and pharmaceutical areas. The findings of the benefits of KGM encourage more applications of KGM in biomaterial field, namely as a controlled release matrix [49], [52], [53]. The excellent gelation properties makes KGM unique and superior in relation to other natural macromolecules [53].

Having in consideration all the characteristics and potentialities of KGM, this material can be more elastic polymer than the routinely used in the fabrication of bone scaffolds, providing a matrix much more versatile that can support for a longer time the attach, migration and proliferation of cells and follow the regeneration process of big defects on bone tissue. Moreover, and thinking always on a bi/multifunctional material, this type of matrix can be an excellent reservoir of drugs/molecules to a controlled release and can be easily functionalized. KGM offers a great versatility, allowing the production of tailored multifunctional scaffolds.

In the case of bone cancer, the combination of tissue engineering methodologies and specific local tumor treatments can provide an alternative treatment option to heal large bone defects resulting from tumor resection. A potentially innovative therapeutic strategy would rely on the use of multifunctional scaffolds that have enhanced osteogenic capacity for bone regeneration combined with the ability to locally destroy residual tumor cells. In this way, with only one strategy it is possible mitigate the limitations and complications associated at each disease condition [27].

### 3.1.3 Other Agents

Other interesting materials can present bifunctional effects and act as anti-cancer agents. Between them, it is important to highlight. metallic ions, due to their magnetic properties, GO and polydopamine which are photosensitive agents [26], [28], [41]. Their mode of action will be provided by the application of an external magnetic field - for magnetic materials - or a laser – for photosensitive agents - which will increase the temperature - hyperthermia effect - and kill the

cancer cells. This effect is very selective (there isn't the risk of kill the healthy cells if the temperature achieved isn't higher than 43°C/45°C [54]–[56], destruction of the immune system and other side effects), localized and minimal invasive [28], [57].

Metallic ions naturally present in bone composition, such as strontium, magnesium, zinc, copper and even silver, have vital roles in the formation, growth, and repair of bone, and thus can be incorporated in the polymeric bases of the scaffolds. In recent years various studies demonstrated that adding these elements to CaP materials, can lead to controlled degradation, increase the mechanical strength of the materials, and positively influence the biological response, improve the performance process after implantation [58], [59].

## 3.2 Fabrication techniques- General Overview

In an organ, cells and their ECM are usually organized into 3D tissues. Therefore, in tissue engineering, the production of a highly porous 3D matrix is often necessary to accommodate cells and to guide their growth and tissue regeneration in three dimensions. Different techniques have been used to fabricate 3D porous ceramics scaffolds for tissue engineering and regenerative medicine [60].

Traditional techniques are relatively simple methods, including solvent casting and particulate leaching, gas foaming, fiber meshes and fiber bonding, phase separation, melt molding, emulsion freeze drying, solution casting and freeze drying [61], [62]. However, most of these methods are incapable of producing fully continuous interconnectivity and uniform pore morphology within a scaffold. In these techniques it is very difficult control the pore geometry, pore size, the spatial distribution and overall porosity of the scaffolds [63]. In addition, the use of organic solvents may cause toxic effects on cells during subsequent culture [64], [65].

Recently, to overcome these obstacles, advanced additive manufacture (AM) techniques have emerged. AM is a diverse group of manufacturing techniques that build objects by adding material in a layer-by-layer fashion (Figure 9).

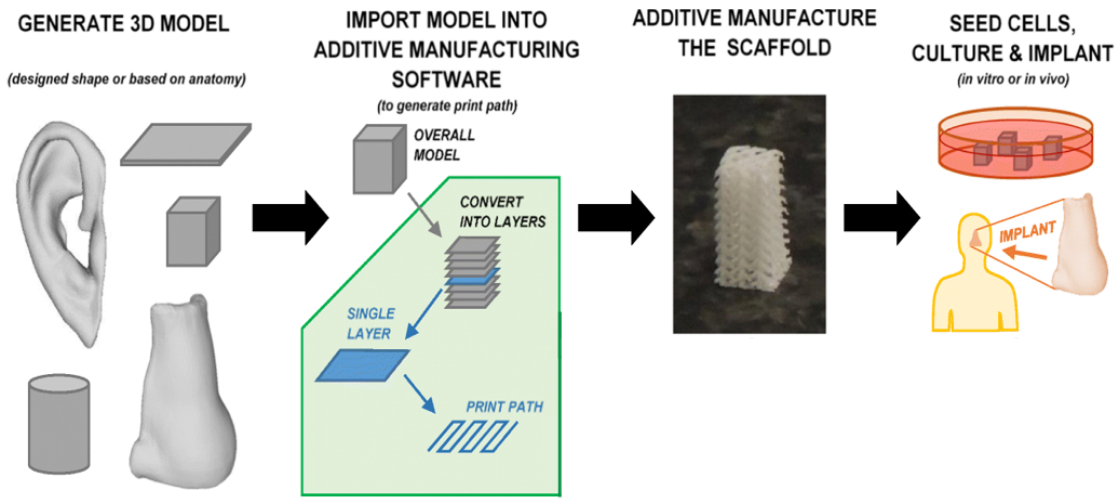


**Figure 9 – AM technique.** Overall procedure for additive manufacturing a tissue engineering construct, with the building of objects through the addiction of material in a layer-by-layer fashion. Through this process it is possible produce a wide variety of objects with complex shapes. Adapted from [66].

Implementation of this simple idea makes a myriad of applications possible, where complex shapes such as those in aerospace and biomedical engineering are possible of being produced with a short time of production runs. It is therefore unsurprising that additive manufacturing has received a significant amount of interest, speculation, and investment from industry and academia, and in recent years it has entered the public consciousness. This has resulted in rapid development of the technology, which has progressed well beyond sensationalized press articles and preliminary prototypes, and is already a disruptive technology in the real world.

### 3.2.1 Robocasting

Most work on additive manufacturing has focused on metals and polymers, both of which are currently being embraced in industry. On the other hand, additive manufacturing of ceramic materials is less well developed [42], [43]. Robocasting emerged as a distinct AM and the use of ceramics starts to be developed. The use of ceramics in Robocasting is based on the following principle (Figure 10): green 3D objects are built by extruding a filament of paste (known as an “ink”) through a fine nozzle while the nozzle’s position is controlled by a computer in accordance with a Computer Aided Design (CAD) model. Objects are built up in a layer-by-layer fashion. As the object is built the extruded filament impinges on the printed part and fuses with it due to surface tension.

Thus, in robocasting the rheology of the ink is a key feature in order to print a self-supporting structure. Robocasting has shown to be a promising technique in producing a range of ceramic materials with relatively good mechanical properties. Furthermore, the flexibility of robocasting opens up a number of possibilities of new microstructures and materials that have yet to be explored [42], [43]. The most recent work developed on the robocasting technique reports the formulation of inks based on a hydrogel which acts as a carrier for a ceramic powder [43].

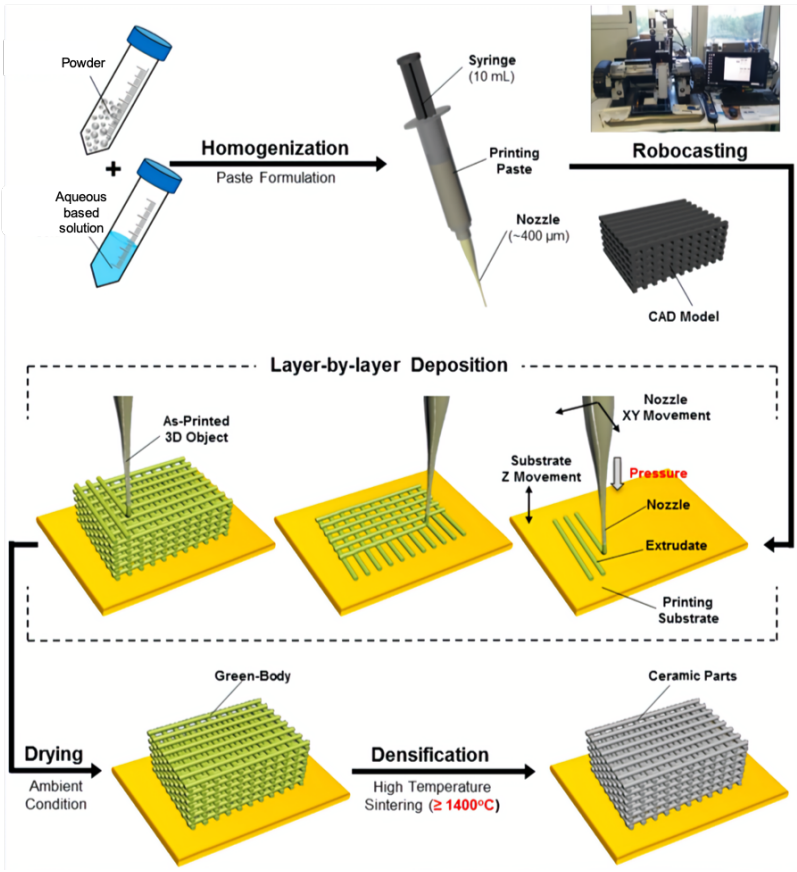


**Figure 10 – Robocasting technique.** The traditional step by step of a produced structure through Robocasting – Ink Formulation, Layer by Layer Deposition of a structure codified by a CAD Model, Drying of the Green Body and Sinterization of the structure. Adapted from [29].

In this work scaffolds will be produced through Robocasting or Direct Write Assembling (DWA). This is an easy and fast fabrication method and considered very promising for biomedical applications. With a 3D-printing technique it is possible to produce a structure with characteristics, such as porosity, that could improve nutrition, transporting and cell ingrowth [25], [46].

## 4. Experimental Strategy Rationale

The scaffolds produced in this work are sintering-free scaffolds (in the production process the last step of the Figure 10 doesn't occur). In this way, the incorporation of drugs, growth factors and other types of molecules and elements which can enhance the anti-cancer therapy is possible during the scaffold fabrication. In a traditional methodology, as a final step, the scaffolds are submitted to high temperatures to improve the mechanical properties. However, any component sensitive to the temperature will be destroyed.

Furthermore, it is not necessary to use traditional methods - soaking methods - to functionalize the material and to be subjected to its limitations. In such methodology the scaffold, after the sintering step, is immersed on a solution containing the desirable component. This usually gives limited functionalization yields. The functionalization efficiency depends on the concentration of the solution that is used, the soaking time and the interaction between the scaffold and the component. Components such as GO and polydopamine are usually deposited in thin layers through coating processes. In this way, the functionalization occurs only on the surface of the scaffold or in specific zones – if the sandwich method is applied. Thus, the surface area limits the process of functionalization.

The development of non-sintered scaffolds allows a more homogeneous distribution of the elements and a more efficient incorporation, specially when dealing with temperature-sensitive components. The increase of the amount of therapeutic component incorporated in the scaffold will provide an increase on the efficacy of the material in promoting regeneration, kill cancer cells or treat an infection. Moreover, non-sintered scaffolds are more cost-effective materials which if efficiently functionalized, can provide a decrease in the therapeutic time of the disease, as well as in the dosage of the therapeutic agent.

For example, this type of scaffolds is very attractive to be functionalized with agents such as magnetic nanoparticles, polydopamine. There are yet some works on the literature that report the use of these components on a multifunctional scaffold to promote bone regeneration and death of cancer cells. Zhang et al. demonstrated that the incorporation of iron oxide and GO into the scaffolds had an important role in the stimulation of osteogenic differentiation

of rabbit bone marrow stromal cells and the scaffolds produced have potential application in killing the residual human bone tumor cells by magnetothermal treatment [25]. Wu et al. verified that the integration of magnetic nanoparticles in the CaP scaffolds can promote the differentiation and proliferation of osteoblast cells [41]. Ma et al. reported in their work the importance of the incorporation of GO in the scaffolds to promote the regeneration of big bone defects and the potential to kill cancer cells [26]. A work performed by the same authors reveled that with the functionalization of scaffolds with polydopamine is possible induce tumor cell death *in vitro*, and significantly inhibited tumor growth in mice. Moreover these scaffolds could support the attachment and proliferation of rabbit bone mesenchymal stem cells, and significantly facilitated the formation of new bone tissue in rabbit bone defects [28].

Despite of the demonstrated effects of these materials, there are still some concerns related with their long-term safety. For instance, metallic nanoparticles are poorly biometabolized and have pertinent issues related to the safety of the metal itself [57]. Iron oxide nanoparticles are the most used and studied. They have excellent properties such as superparamagnetism, biocompatibility and biodegradability [40]. The carbon-based materials have been demonstrated to induce many toxic responses such as oxidative stress and pulmonary inflammation [57]. These are the problems associated with most of the current photothermal agents, promoting an increasing interest on the use of polydopamine [28].

Polydopamine is a polymer imitating melanin that occurs naturally in organs and tissues, such as hair, skin, brain medulla, iris of eyes, and brain medulla. Owing to its satisfactory non long-term toxicity during their retention in rats, biocompatibility and biodegradability, a high median lethal dose polydopamine has greater potential for biomedical application. Furthermore, it has a high photothermal conversion efficiency of 40% (much higher than previously reported photothermal agents), suggesting that dopamine is a favorable photothermal agent for tumor therapy [28], [57].

## 5. Aim of the thesis

The main goal of the work performed in this thesis is to produce and validate free-sintering 3D additive manufactured scaffolds, produced by robocasting to be used in bone tissue engineering. Moreover, the development of a bifunctional 3D material/scaffold: a material that at the same time can promote the regeneration of the bone and kill the cancer cells that remain on the tumor site, and that can prevent the recurrence of the tumor is a further goal.

The specific objectives included:

1. the *in vitro* testing of scaffolds composed by chitosan and CaP powders that had already been developed in the scope of the project in which this thesis is inserted but were not yet validated for *in vitro* culture.
2. Inclusion of magnetic nanoparticles on the chitosan/ biphasic CaP and assessment of the influence of magnetic conditions on MSCs behavior.
3. Overcome the limitations of the existent scaffolds by designing innovative KGM printed scaffolds, in order to find an alternative to the complex handling of chitosan scaffolds and their sterilization process.
4. In vitro testing of scaffolds of KGM and BCPs for a bone regeneration approach (cell delivery).
5. Development and optimization of functionalization of KGM with polydopamine as a photosensitive agent to allow the induction of localized hyperthermia to induce cancer cell death while preserving healthy cells. Strategies include:
    - Production of polydopamine nanoparticles for a further incorporation on the scaffolds ink;
    - Functionalization of the KGM molecules with dopamine;

# Materials and Methods

## 1. Materials

For producing KGM-BCP scaffolds: KGM was purchased from Prozis, Portugal. Biphasic Calcium Phosphate (BCP) powders – containing HA and β-TCP in their composition were kindly provided by the Department of Materials and Ceramics Engineering, CICECO - University of Aveiro, Portugal. For obtaining MNPs scaffolds: Chitosan (Low molecular weight, Sigma-Aldrich) and Calcium phosphate (CaP) powders - HA and β-TCP – were provided by Department of Materials and Ceramics Engineering, CICECO University of Aveiro, Portugal). For KGM functionalization and polydopamine synthesis: NaCl (VWR, Pennsylvania, USA), succinic anhydride – SAC0 (Sigma-Aldrich, Missouri, USA), N-Hydroxysuccinimide - NHS (Sigma-Aldrich, Missouri, USA), 1-(3-Dimethylaminopropyl)-3-ethylcarbodiimide hydrochloride **-** EDC (Alfa Aesar, Massachusetts, USA) and Dopamine hydrochloride (Sigma-Aldrich, Missouri, USA), hydroxylamine hydrochloride (Sigma-Aldrich, Missouri, USA), 25 % (v/v) ammonia solution (Merck, Darmstadt, Germany), 96% ethanol (Valente e Ribeiro, Belas, Portugal), MWCO 3.5 kDa dialysis membrane (Spectra/Por®, SpectrumLabs) were purchased and used as received.

## 2. Chitosan-CaP ink preparation loaded with magnetic nanoparticles (MNPs scaffolds)

The prepared inks consisted in a mixture of 5 wt% chitosan solution containing 10 wt% of citric acid, HA and β-TCP powders non-doped/doped with iron, 1.5 wt% genipin as reticulating agent and 25 mg/mL magnetic nanoparticles solution (fluidMAG-Chitosan, Chemicall, Germany). The amount of ceramic added to the chitosan solution differ if the CaP powders are doped or not. If the ceramic powders are doped, the quantity of solids added is 40 wt%, while if the powders don't have iron ions in the composition the amount decrease to 34 wt%. 1 wt% of this quantity are Magnetic Nanoparticles dried in an oven. The inks were prepared by mixing the several components using a planetary centrifugal mixer (ARE-250, Thinky Corp., Tokyo, Japan). The inks that contained non-doped

ceramic powders were designed as BMNPs, while the ones composed by iron doped ceramic powders were named FeMNPs. This type of ink have been very well characterized as reported in previous studies [67].

# 3. Preparation of the hybrid KGM-BCP printable ink (KGM scaffolds)

## 3.1 Preparation of KGM solution

KGM solutions with concentrations ranging from 0.2-3 wt%, (0.2 wt%, 0.5 wt%, 1 wt%, 2 wt%, 3 wt), in $dH_2O$ have been prepared by overnight stirring (1400 rpm) at room temperature (RT) using a thermomixer (eppendorf thermomixer comfort). KGM solutions with similar concentration have also been prepared in a 0.36% (w/v) $Na_2CO_3$ in order to study the influence of the KGMs' deacetylation in the gelation features of the polymer. The concentration of the aqueous KGM solution was optimized to achieve an adequate viscosity for printing, through the manual extrusion of the solution with syringes.

## 3.2 Preparation of the KGM-BCP ink

After adjusting the concentration of the KGM solution, BCP powders in 30 and 40 wt% have been added in order to obtain a printable KGM-BCP ink. For the preparation of these hybrid organic-inorganic printable inks, an adequate amount of KGM was mixed with 30 wt% or 40 wt% BCP powders and allowed to stir overnight in $dH_2O$ (1400 rpm) at room temperature using a thermomixer (eppendorf thermomixer comfort). After this initial screening, the best KGM-BCP ink formulation (3 wt% KGM with 40 wt% BCP) was prepared using a planetary centrifugal mixer (ARE-250, Thinky Corp., Tokyo, Japan) to obtain an ink with improved homogeneity.

## 4. Robocasting of MNPs scaffolds and KGM scaffolds

3-D scaffolds consisting of a mesh of ceramic rods were constructed layer-by-layer via direct write assembly of the ink using a robotic deposition device (3-D Inks, Stillwater, OK). The ink was deposited through cylindrical metallic deposition nozzles (EFD Inc., East Providence, RI) with a diameter d = 410 μm, at a printing speed of 10 mm $s^{-1}$ (Figure 12B and C).

The external dimensions of the MNPs scaffolds were about 9×9×3 (Figure 11A) in a total of 12 layers. Each structure consisted of 9 individual scaffolds of 3×3×3 mm (Figure 11B and D), which were produced with a pore size of 500 μm. After printing, samples were placed at 37°C overnight with controlled humidity (80%) to promote chitosan crosslinking by genipin. On the following day, the scaffolds were placed at 37°C for 24h.

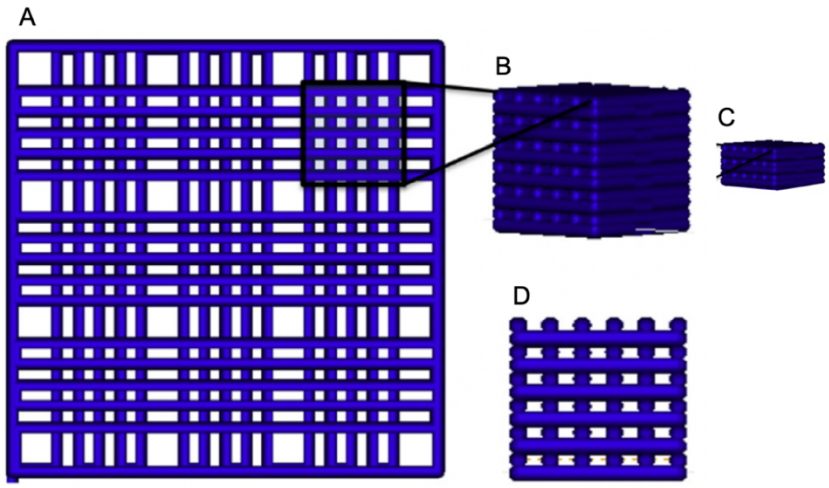


**Figure 11- CAD Model.** The external dimensions of the scaffolds were about 15 × 15 × 3 (A) in a total of 12 layers being 9 individual scaffolds of 3 × 3 × 3 mm (B) and (D), or 6 layers and 9 individual scaffolds of 3 × 3 × 1.5 mm (C) and (D). Adapted from [36].

For the KGM scaffolds the external dimensions were about 9×9×1.5 mm (Figure 11A) in a total of 6 layers. Each structure consisted of 9 individual scaffolds of 3×3×1.5 mm (Figure 11C and D), which were produced with a pore size of 500 μm. After printing, samples were placed in an ethanol bath to promote the assembly of the structure (Figure 12D). After 1h, the scaffolds were placed at 37°C overnight with controlled humidity (80%) to promote the increase of their mechanical properties (Figure 12E).

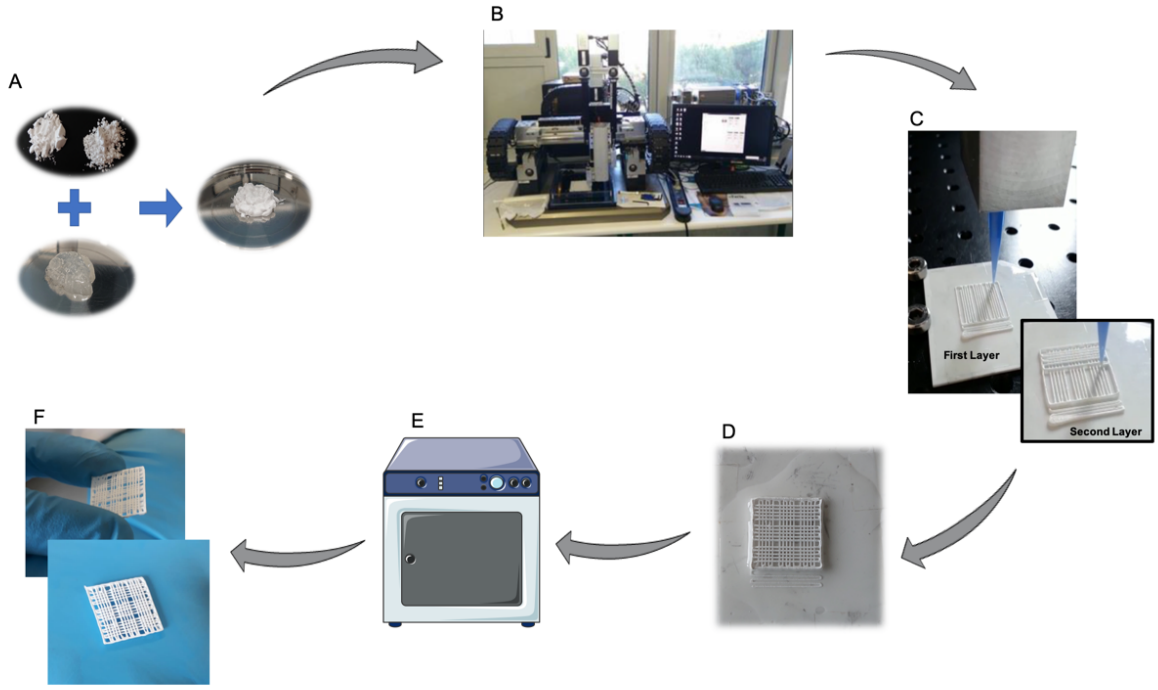


**Figure 12 – KGM scaffolds production cycle.** A) Production of the ink through the mixture of the ceramic powders on the KGM solution. B) Robocasting machine where the ink is extruded through a syringe with a nozzle of 410 µm. C) Layer by Layer Deposition of the ink. D)Ethanol bath for 1h after printing of the structure to improve its' mechanical properties. E) Scaffolds are placed 24h in an oven at 37°C with 80% of humidity. F) Final structure.

# 5. Characterization of hybrid organic-inorganic KGM scaffolds and its components

## 5.1 Rheology

Rheological measurements of the ink and KGM solution were made using a Kinexus Pro Rheometer (Malvern, Pennsylvania, USA). The apparent viscosity of the ink, as well as of the KGM solution, was measured in viscometry mode using a cone and plate sensor system (4°/40 mm) and 150 µm gap size. Samples were placed in the bottom plate geometry and analysed in manual viscometry mode applying different shear stress (0.1, 1, 5, 10, 20, 50, 75, 100, 200, 300 and 400 Pa).

## 5.2 $^{1}$H NMR

$^{1}$H NMR spectra of KGM was recorded using a 400 MHz spectrometer AVANCE III (Bruker). The polymer was dissolved (13.3 mg/mL) in deuterated water ($D_2O$, Euriso-top) and transferred to NMR tubes. 3-(trimethylsilyl)

propionic-2,2,3,3-d4 acid sodium salt (TSP-d4, Euriso-top) used as internal standard (δ = 0 ppm).

## 5.3 Size exclusion chromatography (SEC)

Molecular weight was determined on an Agilent 1260 HPLC system equipped with quaternary pump (G1311B), injector (G1329B), column oven (G1316A), refractive index (G1362A) and dual-angle static light scattering (G7800A) detectors. Standard and samples were dissolved in the mobile phase (0.1M $NaN_3$: 0.01M $NaH_2PO_4$, pH 6.6) at 1 g/L. Separation was carried out with four columns (PSS, Germany): Suprema precolumn (5µm, 8x50mm), Suprema 30Å (5µm, 8x300mm), Suprema 100Å (5µm, 8x300mm) and Suprema ultrahigh (10µm, 8x300mm) at a flow rate of 1 mL/min after a 100 µL injection. Column oven and light scattering detector were kept at 30ºC, while refractive index detector was maintained at 40ºC. Detectors were calibrated with a polyethylene oxide standard (PSS, Germany) of 106 kDa (Mp) and polydispersity index 1.05. Refractive index increments (dn/dc) were calculated from the RI detector assuming accurate sample concentrations.

## 5.4 Attenuated total reflectance- Fourier-transform-infrared spectroscopy (ATR-FTIR)

ATR-FTIR spectra were acquired using a PerkinElmer Frontier FTIR Spectrometer (Massachusetts, USA) from 4000 to 400 $cm^{-1}$ and with 4 $cm^{-1}$ resolution.

## 5.5 Powder X-ray diffraction (XRD)

The amorphous/crystalline nature of the calcinated powders, as well as quantitative analysis of phase composition were determined using a High-Resolution X-ray Diffractometer (PANalytical X'Pert PRO) with Cu Kα radiation (k = 1.5406 Å) produced at 45 kV and 40 mA, which scanned the diffraction angles (2θ) between 5º and 70º with a step size of 0.0260º, time per step 198,645 s. A spectra-fitting software called HighScorePlus was utilized to quantify the percentages of crystalline phases for the calcined powders. This software requires crystallographic information files to fit and quantify each specific phase

within a XRD spectrum. The files utilized in the evaluation of the powders were; HA (# 04-015-7245), β–TCP (#04-006-9376).

### 5.6 Particle Size distribution

Particle size and particle size distributions of the ceramic powders were evaluated using a particle size analyzer (COULTER LS230, UK) with Fraunhofer optical model. For that, the ceramic powders were suspended at low concentration on an electrolyte solution.

### 5.7 Scanning electron microscopy (SEM)

The samples were placed, with a carbon tape, in adequate supports for SEM visualization. Before the visualization the samples were coated with palladium gold. The micro and macroporosity of the scaffolds were assessed through SEM using a High resolution (Schottky) Environmental Scanning Electron Microscope with X-Ray Microanalysis and Electron Backscattered Diffraction analysis: Quanta 400 FEG ESEM / EDAX Genesis X4M.

### 5.8 Measurement of pore size, fiber diameter and grain size of the produced KGM scaffolds

The measurement of pore size, fiber diameter and grain size were performed on SEM images with Fiji, through the execution of a set scale on the images following the scale bar provided by the SEM equipment.

## 6. KGM functionalization with photothermal moieties

### 6.1 Synthesis of carboxylated KGM (KGM-SAC0)

A 1 wt% solution of KGM (100 mg; 0,00006 mmol) in $dH_2O$ was treated with succinic anhydride (257 mg; 0,003 mol) added in two portions (t=0 and t=2h) at 0 ºC. The molar ratio of KGM: succinic anhydride is 1:4, calculated based on the weight of the most abundant monomer of KGM. After the addition of each portion, the pH was adjusted to 7.0 and the mixture allowed to stir for a total of 4h at room temperature. The polymer was precipitated by the addition of 99% ethanol (150 mL) and centrifuged at 4000 rpm and 20 ºC for 10 min (Eppendorf

centrifuge 5810R, rotor A-4-62). The precipitated polymer was further washed with acetone (3x 25 mL) and centrifuged in similar conditions. The white precipitate was dissolved in water, transferred to a MWCO 3500 dialysis membrane and purified through dialysis for 3 days against decreasing, changing the solution 2-3 times per day. The dialyzed solution was frozen, lyophilized, and stored at -20ºC until further use. The product was obtained as a white fluffy solid (75 mg).

## 6.2 Functionalization of KGM-SAC0 with dopamine (KGM-SAC0-Dopamine)

A solution of 1 wt% KGM-SAC0 (36 mg; 0,138 mmol) in MES buffer (0.1M MES, 0.3M NaCl, pH 6.5), was treated with EDC.HCl (29 mg; 0,152 mmol, 1.1 eq) and NHS (17,5 mg; 0,152 mmol; 1.1 eq), following the addition of dopamine hydrochloride (31,5 mg; 0,166 mmol; 1.2 eq) at 4 ºC under argon. The mixture was allowed to stir overnight at room temperature and protected from light. The reaction was quenched with $NH_2OH.HCl$ (10,58 mg; 0,152 mmol, 1.1 eq) and the resultant solution was transferred to a MWCO 3500 dialysis membrane and dialysed for 3 days against decreasing NaCl concentrations, changing the solution 2-3 times per day. The resultant solution was frozen, lyophilized, and stored at -20 ºC until further use. The product was obtained as a yellowish fluffy solid (38 mg).

## 6.3 Synthesis of Polydopamine particles

The reaction medium was prepared by mixing 4 mL of 25% (v/v) ammonia solution, 80 mL of 96% vol. ethanol and 180 mL of deionized water under mild stirring at 30 °C. After 30 min, a solution of dopamine hydrochloride (1g; 0,005 mol) in $dH_2O$ (20 mL) was added and the reaction allowed to proceed for 24 h at 30 ºC. The color of this solution immediately turned to pale yellow and gradually changed to dark brown, indicating polymerization of dopamine [68]. The resultant suspension was centrifuged at 25 000 rpm and the pellet washed with water (3x). The precipitate was resuspended in water and freeze-dried, giving a black powder (112 mg).

### 6.4 Characterization of the obtained materials

The incorporation of SAC0 and Dopamine was confirmed through $^{1}H$ NMR analysis and ATR-FTIR, following the procedures described in sections **5.2** and **5.4**. Dopamine particles were characterized through ATR-FTIR. Transmission Electron Microscopy (TEM) and Ultra-violet visible spectroscopy (UV-Vis) of the dopamine particles were performed at Universidad de Vigo by Laura Marín Caba from the research group TeamNanotech.

## 7. *In vitro* studies

### 7.1 Cell culture

human Dermal Neonatal Fibroblasts (hDNFs) were purchased from ZenBio and human mesenchymal stromal cells were purchased from Lonza. Cells were thawed and maintained in culture at 37°C in a humidified atmosphere with 5% v/v $CO_2$ in air.

Primary hDNFs used for cytotoxicity assays were cultured in Dermal Fibroblast Culture Medium (DMEM, Invitrogen) with 10% v/v FBS, 1% v/v Penicillin/Streptomycin (P/S) and 1% v/v Amphotericin B.

hMSCs were expanded in an Expansion Medium (EM) before the seeding on the scaffolds. EM consisted of α-Minimum Essential Medium (α-MEM, Gibco, California, USA), 10%vol of heat-inactivated Mesenchymal Stem Cell Fetal Bovine Serum (MSC FBS, Gibco, California, USA) and 1% v/v Penicillin/Streptomycin (P/S).

Cells were trypsinized when 70-80% confluence was reached. For culture on-top of the scaffolds, hMSCs were seeded at a concentration of 1,4 $x10^4$ cells per scaffold. 300 µL of the respective cell culture medium was added to each well and samples were incubated for different periods of time.

### 7.2 Cytotoxicity

To evaluate scaffolds cytotoxicity, KGM scaffolds were tested in direct (samples) and indirect (leachables) contact assays according to the ISO 10993-5 standard practices. Samples were sterilized in 70% vol. ethanol and washed three times in ultrapure water prior to this assay. hDNF cells were seeded in

culture wells for 24h at a density of $2x10^4$ cells/well, 24h later, samples (direct contact) and culture medium that already have been in contact with samples (indirect contact) were incubated with the cells for another 24h. The culture medium was then removed from the wells and fresh basal medium with 20% v/v resazurin (Sigma-Aldrich, Missouri, USA) was added. Cells were incubated (37°C, 5% v/v $CO_2$) for 2h, after which 3 x 100 µL per well were transferred to a black 96-well plate and measured (Ex at 530 nm, Em at 590 nm) using a micro-plate reader (Synergy MX, BioTek, New Hampshire, USA). The control consisted in cells alone.

## 7.3 hMSCs culture on 3D MNPs scaffolds and 3D KGM scaffolds

Prior to cell seeding, the scaffolds were sterilized using 70% vol. ethanol for at least 15 min and washed three times with ultrapure water. hMSCs were seeded on the MNPs scaffolds by placing a droplet of 10 µL per scaffold containing 25 000 cells. For KGM scaffolds, hMSCs were seeded by placing a droplet of 20 µL per scaffold containing 13 600 cells. hMSCs were allowed to adhere before adding 300 µL of Basal Medium (BM) per well. Basal Medium is composed by α-MEM (Gibco, California, USA), 10%vol of heat-inactivated fetal bovine serum (FBS, Gibco, California, USA) and 1% v/v Penicillin/Streptomycin (P/S).

After 7 days in BM, in half of the scaffolds the culture medium was switched to Osteogenic Medium (Figure 13). Osteogenic medium is composed of BM supplemented with $5\times10^5$ M Ascorbic Acid (Sigma, Missouri, USA), 0.1µM of dexamethasone (Sigma, Missouri, USA) and 0.01M of β-glycerophosphate (Sigma, Missouri, USA).

Medium was changed every 2 days for up to 21 days of culture for MNPs scaffolds and 28 days for KGM scaffolds.

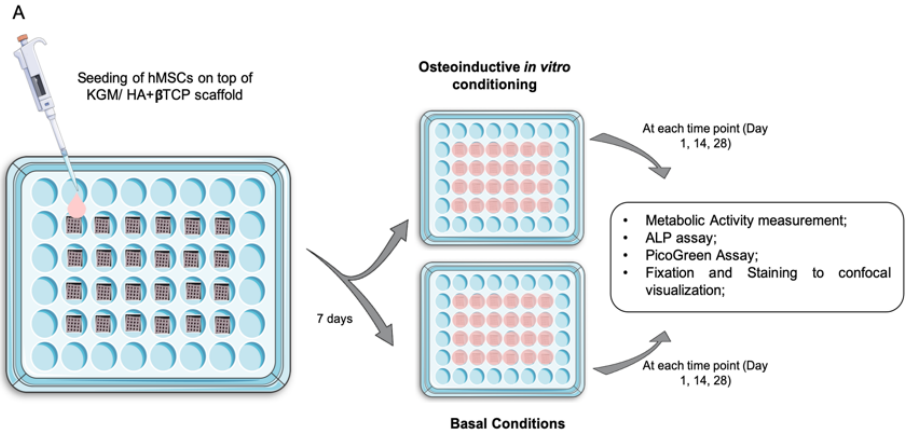


**Figure 13 – Schematic Illustration of hMSCs culture on 3D KGM scaffolds.** The cells were seeded on top of scaffolds with a drop of 20 µL. After promoting the attachment of the cells to the scaffolds, 300 µL of Basal medium was added to the wells. After 7 days the osteoinduction was initiated. In half of the samples the basal medium was changed to an osteogenic medium – basal medium enriched with dexamethasone, β-glycerophosphate and ascorbic acid. At each time point cells were collect to performed the assays described on the figure.

For the MNPs scaffolds, in the same day that the culture medium was switched to osteogenic medium, half of the samples were submitted to an external magnetic field of 25 mT, by placing the plate where the samples are in the middle of plates where magnets were placed wrapped in cotton (so that there is no attraction between the magnets and interferences on the magnetic field applied are minimized) – Figure 14.

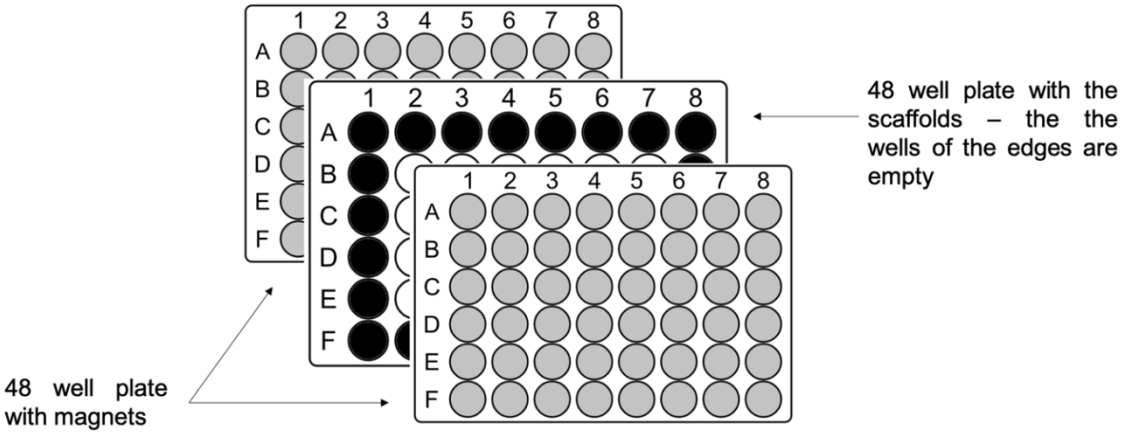


**Figure 14 – Experimental Set-up of the MNPs scaffolds.** Half of these scaffolds were submitted to an external magnetic field of 25 mT placing the well plate containing the scaffolds in the middle of well plates with magnets.

## 7.4 Metabolic activity

Metabolic activity, for both type of scaffolds, was estimated using a resazurin-based assay. At different time-points, the culture medium was removed from the wells and fresh medium with resazurin (20 % (v/v), Sigma) was added (500 µL/well). Samples were incubated (37ºC, 5 % (v/v) $CO_2$) for 3h, after which 100 µL/well were transferred to a black 96 well plate and the fluorescence signal was measured ($\lambda_{ex} \approx 530$ nm, $\lambda_{em} \approx 590$ nm) using a micro-plate reader (Synergy MX, BioTek).

## 7.5 Biochemical analysis

### 7.5.1 Alkaline phosphatase (ALP) activity

Cells were collected from the scaffolds through a trypsinization – the scaffolds were transferred to eppendorfs and incubated for 5 min. The scaffolds were then removed and a pellet of cells was obtained through centrifugation (5 min. at 1200 rpm). The supernatant was discarded and the dry pellet was obtained.

Briefly, cells were lysed with 50 µL of 1% (v/v) Triton X-100 (CALBIOCHEM, San Diego, USA) and 1×PBS was used to dilute the suspension to 0.1 % (v/v). The homogenized lisates were transferred to a 96-well plate – 20 µL in each well. ALP substrate – p-nitrophenyl phosphate, disodium -100 mg capsules (Sigma- Aldrich, Missouri, USA) was added to each well, and incubated for 1h at 37°C protected from light. Absorbance, was measured (405 nm) using a micro-plate reader (Synergy MX, BioTek, New Hampshire, USA). For each time-point (1, 14 and 28 days) a minimum of 3 samples per condition was analyzed.

### 7.5.2 Protein quantification

Total protein content was quantified using the BCA Protein Assay kit (Pierce™, Thermo Scientific) following the manufacturer protocol. Briefly, a standard curve was generated using BSA solutions, in a concentration range from 0 mg/mL to 2 mg/mL. Samples and standards were incubated for 2h at 37°C

with BCA working reagent and absorbance was measured at 570 nm in a microplate reader (SynergyTM Mx, BioTek).

### 7.5.3 DNA quantification

For the quantification of the total double-stranded DNA (dsDNA) content, the scaffolds were trypsinized, washed with PBS, and the suspension was centrifuged (1200 rpm, 5 min) to allow recovery of hMSCs. Samples were then stored at 20°C until further analysis. The dsDNA quantification was performed using the Quant-iT PicoGreen dsDNA kit (Molecular Probes, Invitrogen), according to the manufacturer's instructions. Briefly, the frozen samples were thawed and lysed in 1% v/v Triton X-100 (in PBS) for 1 h at 250 rpm and 4°C. Then, they were transferred to a black 96-well plate with clear bottom (Greiner) and diluted in TE buffer (200 mM Tris–HCl, 20 mM EDTA, pH 7.5). After adding the Quant-iT PicoGreen dsDNA reagent, samples were incubated for 5 min at RT in the dark, and fluorescence was measured using a microplate reader ($\lambda_{ex}$ z 480, $\lambda_{em}$ z 520 nm).

## 7.6 Viability assay

Viability was evaluated through Live/Dead Assay, using Ethidium homodimer-1 (Invitrogen) and Calcein-AM (Invitrogen) dissolved in DMEM without phenol red (2.5µL Ethidium and 2µL Calcein per mL of medium) and kept protected from light. The assay was performed at defined timepoints. Briefly, media was removed, samples were washed with DMEM without phenol red and then incubated in the Ethidium/Calcein solution for 45 min, at 37°C. This solution was then replaced by DMEM without phenol red. Immediately after incubation, cells were visualized with a confocal laser scanning microscope (CLSM, Leica SP5, Leica Microsystems, Wetzlar, Germany) using LCS software (Leica Microsystems, Wetzlar, Germany). The scanned Z-series were projected onto a single plane and pseudo-colored using ImageJ.

## 7.7 Immunostainings

The 3D structures were stained with combinations of primary antibodies present on Table 2, DNA and filamentous actin (F-ACTIN). Briefly, cell culture

medium was removed and samples were washed with PBS, fixed for 15 - 20 min in a paraformaldehyde (PFA, EMS, Pennsylvania, USA) solution (4 % (w/v) in PBS), and permeabilized with Triton X-100 (CALBIOCHEM, San Diego, USA) (0.1 % (v/v) in PBS) for 5 min. Samples were then incubated for 30 min. in a bovine serum albumin (BSA, VWR International, Pennsylvania, USA) solution (1 % (w/v) in PBS). The 3D structures were incubated overnight at 4ºC in a humidified atmosphere with BSA (1 % (w/v) in PBS) with combinations of different primary antibodies. Then, samples were washed with PBS and incubated with the BSA solution for 40 min. at RT with the secondary antibodies present on Table 2. Samples were subsequently washed with PBS solution and DNA was counterstained with a solution of 4',6-diamidine-2′-phenylindole dihydrochloride (DAPI) (0.1 mg/ml) in anti-fading mounting medium (VECTASHIELD, Vector Laboratories) 10 min before confocal microscope visualization (CLSM, Leica SP5, Leica Microsystems, Wetzlar, Germany) using LCS software (Leica Microsystems, Wetzlar, Germany). The scanned Z-series were projected onto a single plane and pseudo-colored using ImageJ.

Adobe Photoshop CC software was used for the image adjustments, namely the correction of channels levels and brightness and contrast.

**Table 2** - List of primary and secondary antibodies used in this study.

| **Primary antibody** | **Manufacturer** | **Dilution** |
|---|---|---|
| Anti-Collagen Type I (Rabbit) | Rockland Immunochemicals | 1:200 |
| anti-hAlkaline Phosphatase - Monoclonal Mouse $IgG_1$ | R&D Systems | 1:33 |
| Flash Phalloidin™ Green 488 | BioLegend | 1:100 |
| **Secondary Antibody** | | |
| Alexa Fluor® 647 (Chicken anti-mouse) | Life Technologies | 1:1000 |
| Alexa Fluor® 594 (Goat anti-rabbit) | Life Technologies | 1:1000 |

## 8. Statistical analysis

Statistical analyses were performed using GraphPad Prism 8.1.2(227) 4 software. For the quantification data and metabolic activity measurements, the non-parametric Mann– Whitney test was used. All tests were performed using a 99% confidence interval.

# Results and Discussion

The main goal of the project on which this thesis is inserted comprises the development of bioceramic scaffolds by 3D-printing. Such scaffolds should incorporate thermal sensitizer materials and/or drugs to hold in the same component multi-functionalities: (1) bone regeneration, (2) hyperthermia therapy to destroy cancer cells and (3) local infection treatments after bone surgeries.

The development of multifunctional bone substitute relies in the fabrication of CaP scaffolds without sintering step, leading to a sintering-free bifunctional biomaterial. As a consequence, the addition of temperature sensitive biomolecules becomes feasible. For instance, the inclusion of drugs or other active molecules can be accomplished during ink preparation for 3D-printing process, improving functional properties of bone substitutes with reducing processing time and related costs. The structural integrity and osteogenic activity of the scaffolds is achieved by using high concentrated CaP aqueous based inks containing natural and sustainable polymers such as chitosan or KGM. In the specific case of chitosan-based scaffolds, a crosslinking agent was used as an additive to achieve scaffolds with minimal structural integrity to be manipulated.

Direct assembling by 3D-printing allowed fabrication of scaffolds analogous to bone defect geometries, with controlled porosity, shape and size. Functionalization of the scaffolds to be used for hyperthermia was also explored in this work as a proof-of-concept.

## 1. Chitosan-CaP scaffolds loaded with magnetic nanoparticles (MNPs scaffolds)

The production of Chitosan-CaP scaffolds has been previously optimized [67] and the main goal for this thesis was to investigate the *in vitro* behavior of these scaffolds.

In order to obtain scaffolds suitable for treatment through hyperthermia, two different strategies were followed, namely photothermal and magnetothermal additives. Magnetothermal effect was investigated by adding commercial magnetic nanoparticles in the extrudable ink. This effect has been widely explored by the scientific community in nanoparticles fabrication for nanofluid

hyperthermia [69], [70]. The second strategy was the inclusion of iron as doping agent, since it provides magnetic properties [25]. In order to induce hyperthermia, an alternate magnetic field is normally used, however we used a static magnetic field that is able to influence the MNP but is not able to induce temperature alteration. The main parameter to be tested with this specific set of experiments is the magnetic field effect on hMSC behavior and not the temperature effect.

The validation of such scaffolds for *in vitro* cell culture conditions is essential for the development of this strategy. Aspects of culture conditions stability and scaffold manipulation were evaluated. Furthermore, the addition of iron and/or magnetic nanoparticles and posterior application of a static magnetic field effects on hMSC viability and metabolic activity were also assessed. Powders and inks used to fabricate these scaffolds were characterized in Marques et al., 2018 and on a previously worked by the same team [71].

## 1.1 hMSCs viability and metabolic activity on MNPs scaffolds

After scaffold sterilization, previously optimized cell density was used to perform the initial seeding. Briefly, 25 000 hMSC cells concentrated in a 10 µL droplet was added to each scaffold and cells were let to adhere on top of MNPs scaffolds for 30 min. After this time, culture media was added to the individual scaffolds. After 7 days, samples for each scaffold composition (BMNPs, BMNPs with magnets, FeMNPs and FeMNPs with magnets) were divided into osteoinductive conditions and basal conditions as described previously in section **7.3**.

After 1 and 21 days a qualitative Live/Dead assay (Figure 15) was performed. Calcein (green) marks live cells while Ethidium homodimer is able to stain dead cells in red. It is important to highlight, however, that this is not a quantitative assay, nor an adequate assay to take valid conclusions in terms of cell morphology. Our results show that cells were not only able to adhere to all scaffolds formulations (Figure 15 Day1) in different extents, but an increase of hMSCs number was also detected when comparing confocal images of day 1 with images obtained after 21 days in culture. This suggests that all the different scaffolds allowed the proliferation of hMSCs both in Basal and Osteogenic conditions.

The highest seeding efficiency was observed in iron-doped scaffolds (FeMNPs and FeMNPs w/ magnets), where the majority of the observed live cells adhered to the scaffold fiber suggesting that iron doping was beneficial to the initial attachment of hMSCs. After 21 days, all the conditions showed increased cell density when comparing with the initial timepoint. Particularly, the FeMNPs scaffolds presented higher cell density possibly due to the increase initial cell attachment.

According to the Live/Dead assay visual inspection, BMNPs scaffolds presented apparent lower initial cell seeding efficiency when compared to iron doped scaffolds. However, in the latter, the hMSCs were able to recover and occupy the scaffold fiber after 21 days, mainly in the scaffolds subjected to magnetic conditions, meaning that the difference on initial seeding was not biologically relevant.

In this work, the application of an external magnetic field was performed with the objective to achieve results similar to some studies reported in the literature. Wang et al., showed that the incorporation of $Fe_3O_4$ nanoparticles into the scaffold can lead to minimal magnetic forces in the scaffold under application of an external magnetic field, that continually stimulate osteoblastic cell proliferation, differentiation, osteogenic gene expression and secretion of new natural extracellular matrices [27]. However, the obtained results weren't enough to corroborate the studies reported on the literature.

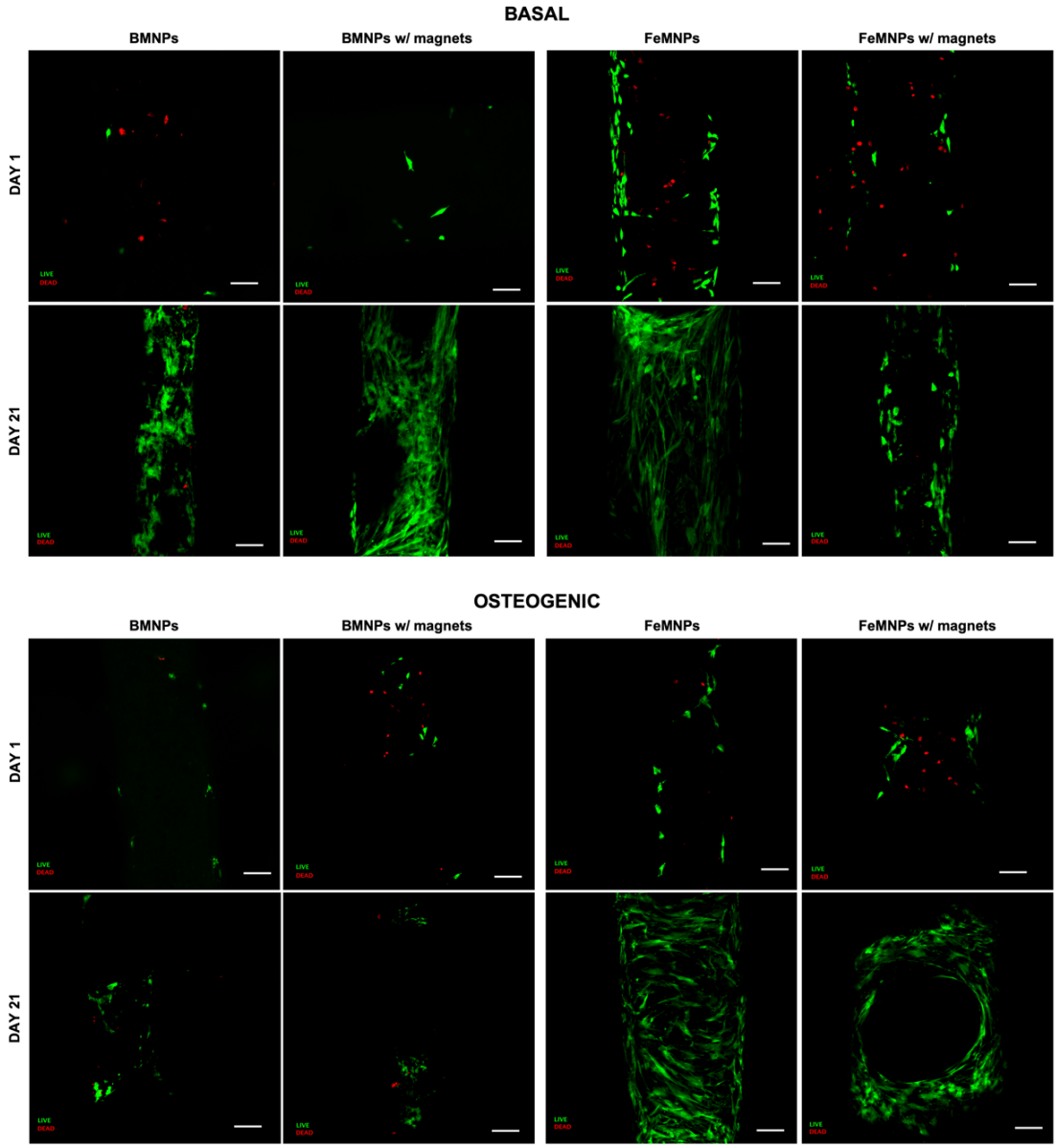


**Figure 15 – Live/Dead assay of hMSCs on MNPS scaffolds.** Representative confocal microscopy images of live/dead staining of hMSCs seeded on MNPSs scaffolds at day 1 and day 21 of culture for basal and osteogenic conditions (Scale bars: 100 μm).

Using a resazurin assay we studied the metabolic activity of hMSCs on the different scaffolds (Figure 16). As expected, metabolic activity at the initial timepoint was comparable among all the conditions reflecting homogeneous seeding efficiency. The only condition that presented lower metabolic activity at day 1 was BMNPs with magnets in the basal media probably reflecting an experimental error. There is a statistically significative increase when comparing day 1 to day 21 for every condition tested in concordance with the live/dead assay but surprisingly, after 21 days in culture, for BMNPs, BMNPs with magnets and FeMNPs, metabolic activity levels of the osteogenic condition are statistically

significantly higher than the ones of the same scaffolds in the basal media. This was not expected since differentiated osteoblasts rarely divide compared with the more immature cells. Thus, a lower metabolic activity in cells cultured in osteogenic media would be expected [72]. Further studies are needed to understand the significance of these results, namely quantification of DNA and/or number of cells per scaffold to allow the normalization of the results from resazurin assay. Metabolic activity is not always directly related to cell number (although often used in the literature as a direct measurement). For example, senescent cells present higher levels of metabolic activity than non-senescent cells for the same number of cells and even different stages of differentiation can influence cell metabolic activity.

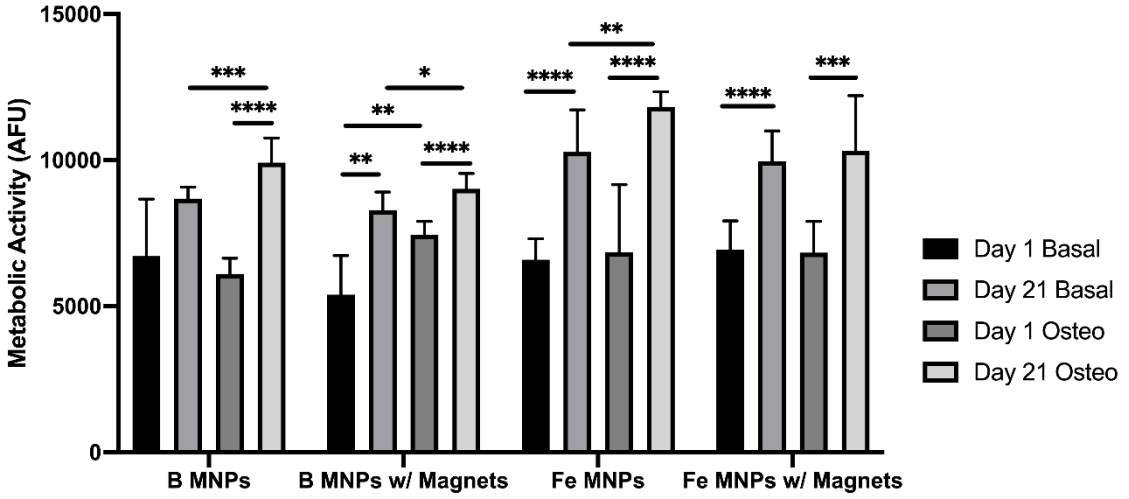


**Figure 16** - **hMSCs metabolic cell activity on the different scaffolds.** Metabolic Cell Activity during the differentiation assay for basal and osteogenic conditions. An increase on the metabolic cell activity from day 1 to day 21 is verified for both conditions and for all the types of scaffolds. Statistically significant differences are marked with * ($p < 0.05$), ** ($p < 0.01$), *** ($p < 0.001$) or **** ($p < 0.0001$). When nothing is indicated means not statistically significant.

With these preliminary experiments, we obtained very important clues for designing future studies. However, definitive conclusions cannot be achieved.
When analyzing the statistical differences on the metabolic activity caused by the application of an external magnetic field (Supplementary Table S1) - comparing the values obtained for BMNPs and BMNPs w/ magnets with the ones obtained for FeMNPs and FeMNPs w/ magnets, as well as the influence of the presence of iron on the powders (BMNPs scaffolds vs. FeMNPs scaffolds) (Supplementary Table S2) - it could be suggested that iron seems to have influence on the metabolic cell activity only for the osteogenic condition, when the scaffolds are

not under the influence of a magnetic field. The application of it doesn't seem to have a significant impact on the metabolic cell activity, except when the scaffolds have iron incorporated and are under osteogenic induction.

## 1.2. hMSCs morphology and Collagen type I deposition on MNPs scaffolds

Cellular morphology was evaluated through F-actin staining, at day 1 and 21, for all the scaffolds tested (Figure 17).

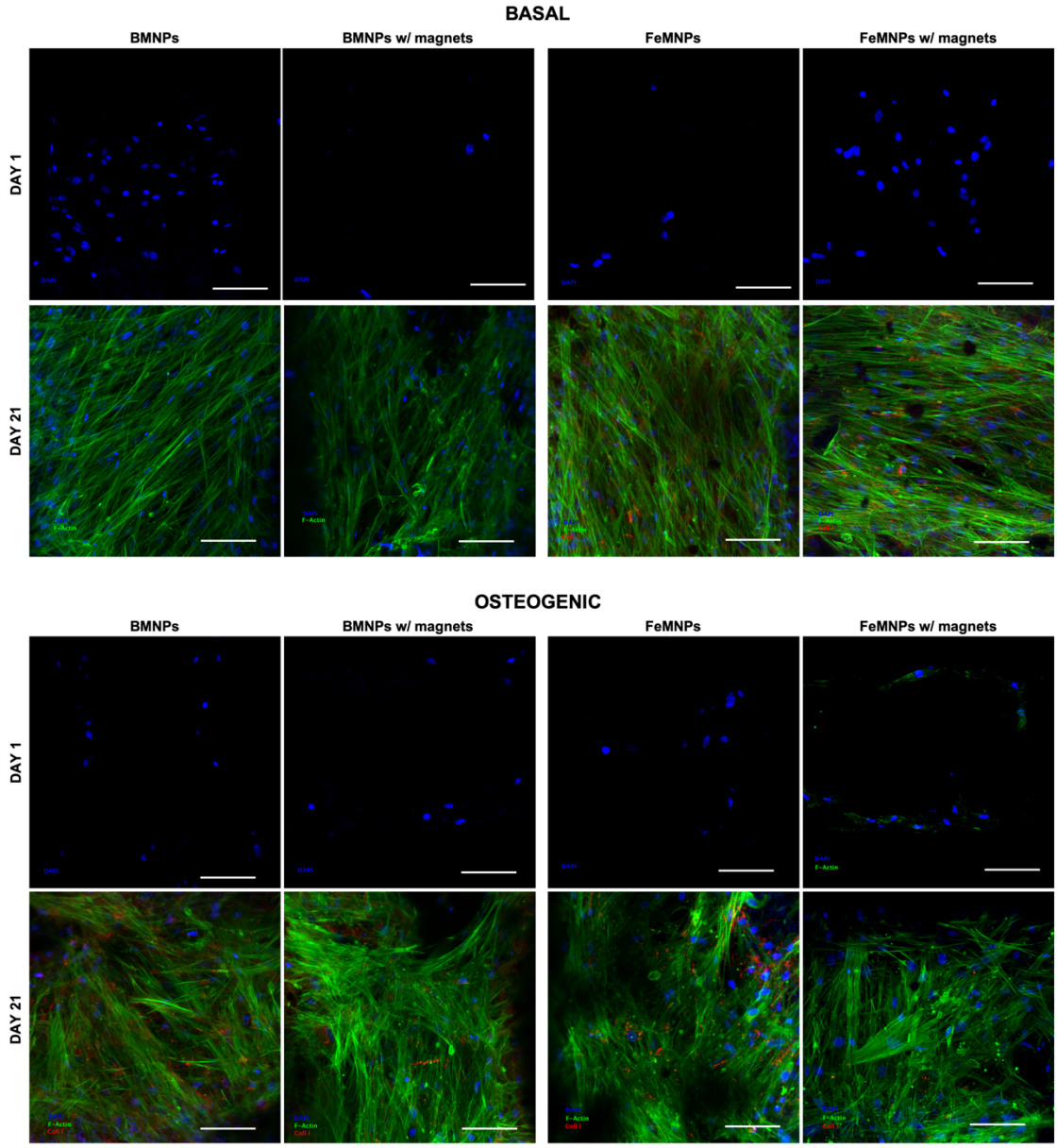


**Figure 17 – Cells Morphology.** Representative confocal microscopy images from the two timepoints, for both conditions and for all type of scaffolds, stained for nuclei (blue), F-actin (green) and Collagen type I (red). Analyzing the images, it is possible to observe the proliferation and migration of the cells from day 1 to day 21, for all conditions. Moreover, the expression of Collagen type I is seen in certain conditions at day 21 of culture. (Scale bars: 100 µm)

At day 1, similar results were obtained for all conditions. Cells were able to spread and acquired a typical hMSC morphology. In accordance to what was suggested by the viability and metabolic activity assays (Figures 15 and 16), hMSC were able to proliferate on both basal and osteogenic conditions with a visible increase on total cell numbers from day 1 to day 21 (Figure 17) displaying full occupancy of the scaffolds. In fact, no pores can be observed since the hMSCs proliferate and occupy the interior of the scaffold pores. A Collagen type I mesh is also present after 21 days for some conditions. Though no proliferation marker (such as Ki67) was used in this study, it can clearly be observed the difference on the number of cells throughout time in culture. Comparing the morphology and orientation of hMSCs in the several scaffolds, no differences could be identified.

Overall the results obtained with these chitosan-based scaffolds were not conclusive. Many experiments could have been done such as ALP expression to assess the efficiency of hMSC differentiation, DNA and protein quantification and gene expression analysis. However, we decided against it since these scaffolds, when in contact with culture media, revealed to be very complex to manipulate during the experiments. We lost numerous scaffolds during the experiments and since no striking evidence of the effectiveness of this strategy arose during these experiments we decided to re-design the fabrication of the scaffolds and explore other biomaterials and strategies that could constitute a better alternative to our scientific problem.

# 2. Preparation and characterization of the hybrid organic-inorganic KGM scaffolds

In order to solve the problems related with the manipulation of the chitosan-CaP scaffolds, a new strategy was developed with the use of KGM as the polymeric support for the ceramic powders. All the components used in scaffold composition were characterized regarding their structural and physico-chemical properties – the polymer, the powders, the ink formulation and the scaffolds itself.

## 2.1 Characterization of KGM

Konjac Glucomannan was selected based on literature review of polymers that could be used for extrusion 3D printing. The profile presented was considered suitable for further investigation. The structure of KGM was primarily characterized through $^{1}$H NMR analysis (Figure 18). Itis reported in the literature that KGM back chain is mainly constituted by mannose and glucose monomers, some of which may be acetylated [73]. In the $^{1}$H NMR spectrum it is possible see the peaks corresponding to the protons of the monomeric units that compose the polymeric chain. Peaks attributed to the glycosidic moiety have been observed in the range 5.5 ppm-3.2 ppm, marked as H-1, H-2,H-6 and H-8 in the Figure 18, in accordance with what has been reported in the literature [74], [75]. Because KGM is partiality acetylated, in the monomer represented in Figure 18B the R's group can be either a hydrogen atom or an acetylated group. The presence of an acetylated moiety was observed by the appearance of a broad singlet at 2.20 ppm, attributed to the methyl protons ($CH_3$) of the acetylated moieties [74]. Through the ratio of the integral between this peak and the one corresponding to proton 1, it was possible to determine the acetylation degree of KGM, which was calculated to be around 8% (Determination of acetylation degree on Supplementary material). This means that 8% of the monomeric units of KGM are acetylated. The calculated acetylation degree is in well concordance with the range of acetylation degrees reported in the literature for KGM [52], [76].

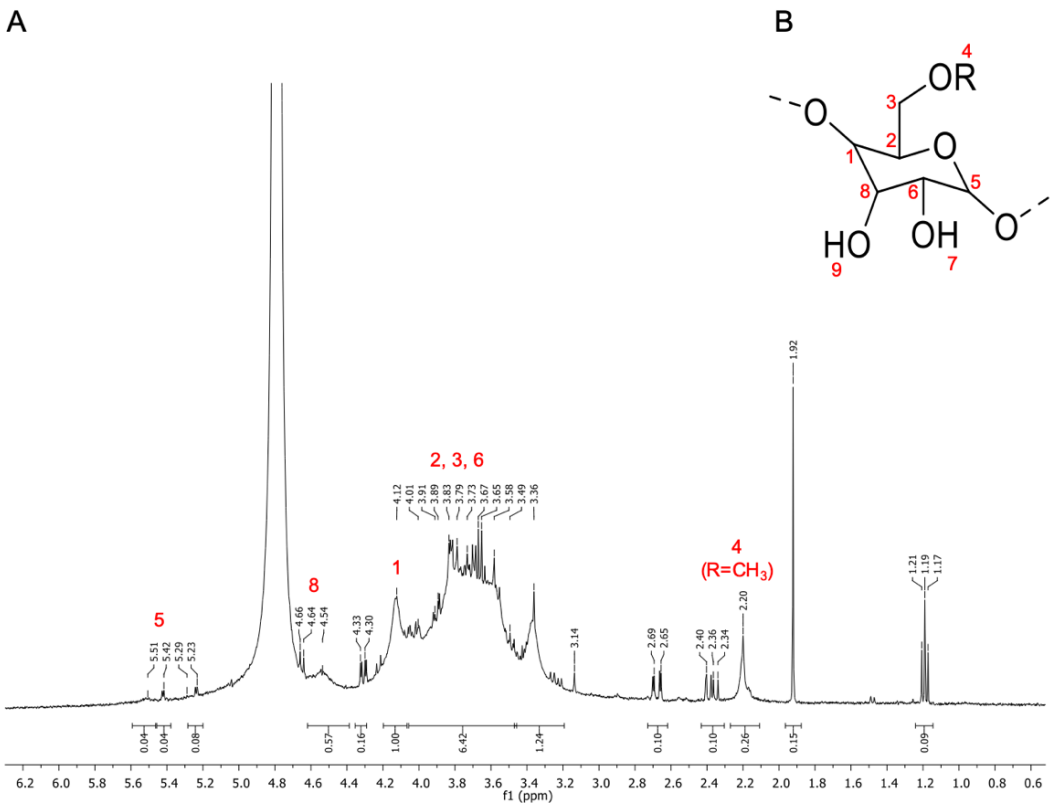


**Figure 18 - $^{1}$H NMR Spectrum of Konjac Glucomannan in $D_2O$.** A) In this spectrum it is possible to identify the different peaks corresponding to the protons of the KGM monomer. Analysing the spectrum, it is possible to identify the majority of the protons of the glycosidic unit belonging to KGM monomer. B) Chemical structure of the KGMs' monomeric units. R= H or $CH_3$.

Analysis of KGM by ATR-FTIR provided important information about some groups present in the polymer structure (Figure 19). The peak between 3600 $cm^{-1}$ - 3000 $cm^{-1}$ is attributed to stretching vibration of the O-H bond in OH groups, while the peak at 2900 $cm^{-1}$ is characteristic of C-H stretching in methylene moieties [27], [74], [75]. Important peaks have been also observed at 1735 $cm^{-1}$, characteristic of the acetyl groups (C=O stretching vibration) present in some units of the molecular chain, as well as in the region of 1500 $cm^{-1}$ – 1000 $cm^{-1}$ (1384 $cm^{-1}$, 1159 $cm^{-1}$, 1058 $cm^{-1}$ and 1024 $cm^{-1}$) associated with C-C, C-O and C-H stretching vibrations in the glycosidic units of the polymeric chain. Finally, the peaks at 875 $cm^{-1}$ and 805 $cm^{-1}$ are characteristic peaks of mannose (one of the sugars which composes the main chain of KGM) [27], [73]–[75].

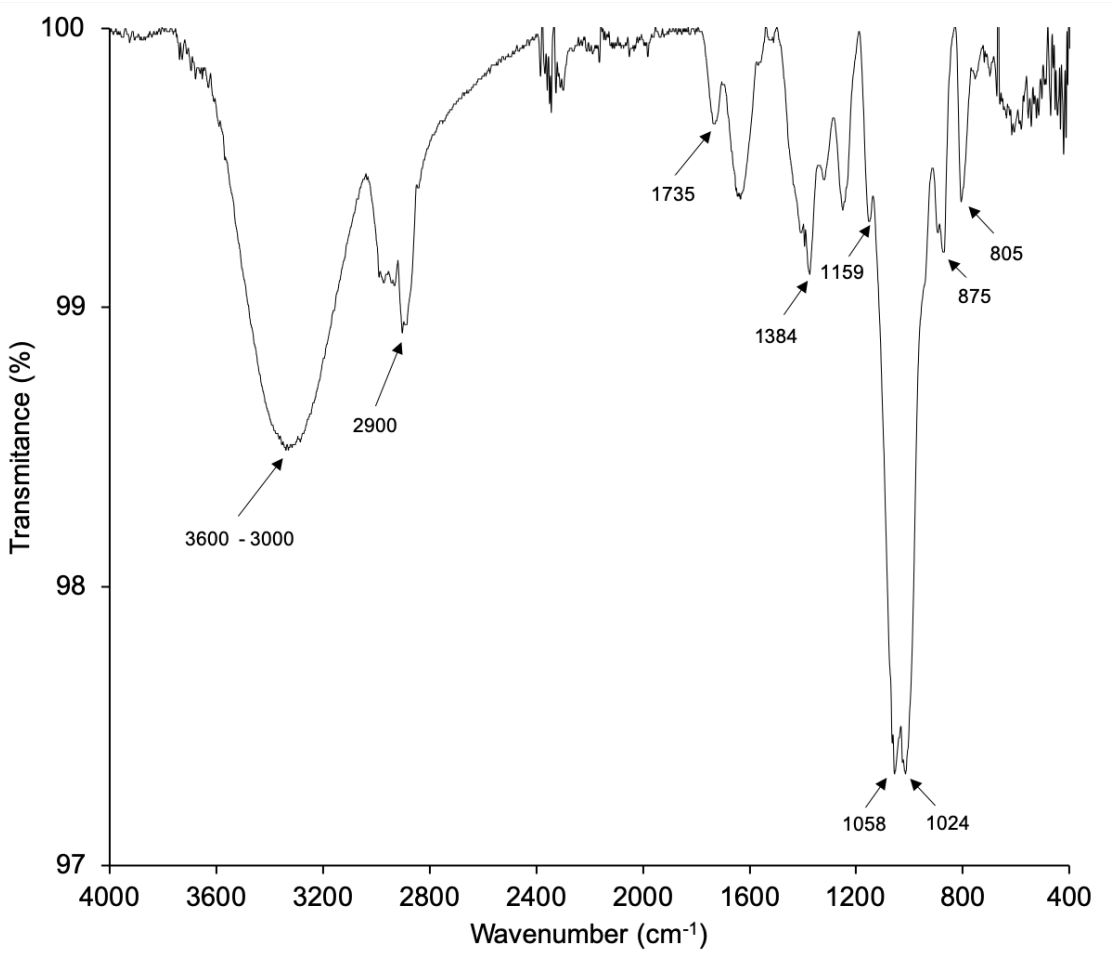


**Figure 19 - ATR-FTIR Spectrum of Konjac Glucomannan.** In the spectrum it is possible to see the appearance of peaks characteristic of functional groups present in the structure of KGM.

Size exclusion chromatography was performed in order to assess molecular weight distribution of KGM (Figure 20). The polymer exhibited a mean value Mw= 1740,073 ± 61,305 kDa with a polydispersity index of 1,170. The molecular weight distribution approaches a normal distribution, and the obtained polydispersity index showed that the relative concentration of molecular weight distribution of KGM was representative of a relatively homogeneous polysaccharide [77]. The value obtained for molecular weight is in accordance with the values reported in the literature, approaching the highest value of the typical range of molecular weight reported to this polysaccharide [76]. Such high molecular weight constitutes an important characteristic to allow the fabrication of a good structural base for the ink and achievement of good rheological properties [77]. The monomeric composition of the polysaccharide and the low acetylation degree allows the dissolution of the polymer in $dH_2O$, which is a great advantage since it can act as a support organic matrix for the inorganic powders.

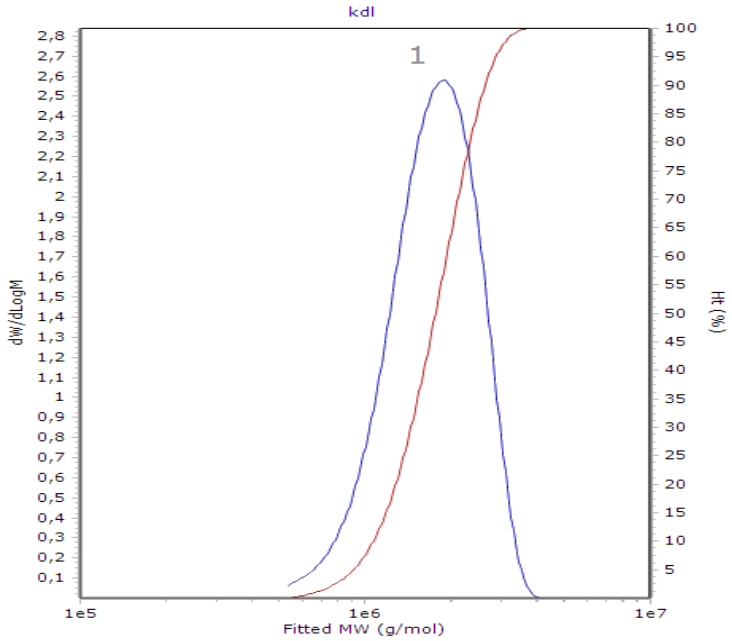


**Figure 20 – Konjac Glucomannan molecular weight.** Molecular weight distribution of the polymer with a mean value Mw=1740,03 kDa and a polydispersity index of 1,170.

## 2.2 Characterization of the ceramic BCP powders

The amorphous/crystalline nature of the BCP powders, as well as their phase composition has been investigated by powder X-ray diffraction (Figure 21). Results suggests that the supplied powders were crystalline and presented a biphasic composition. The XRD patterns, reveal that both powders consist essentially of well-crystallized HA and β-TCP phases in different proportions, as previously reported. By comparing the pattern of each powder with reference patterns for pure HA (PCPDF: 04-015-7245) and β-TCP (PCPDF: 04-06-9376), it was observed a superposition of the three more intense peaks in the powders with the corresponding reference files (Figure 21). While for HA the peaks of HA crystalline phase were more intense, for TCP powder the peaks corresponding β -TCP phase prevail over the ones corresponding to HA crystalline phase. It was possible to determine the quantitative composition of each powder through the relative intensities of the peaks corresponding to each crystalline phase. While HA powder presented higher content in HA than in β-TCP, the TCP powder exhibited a higher content in β-TCP. Thus, the HA powder was composed of 96% of HA and 4% of β-TCP, while TCP powder was composed by 38% of HA and 62% of β-TCP.

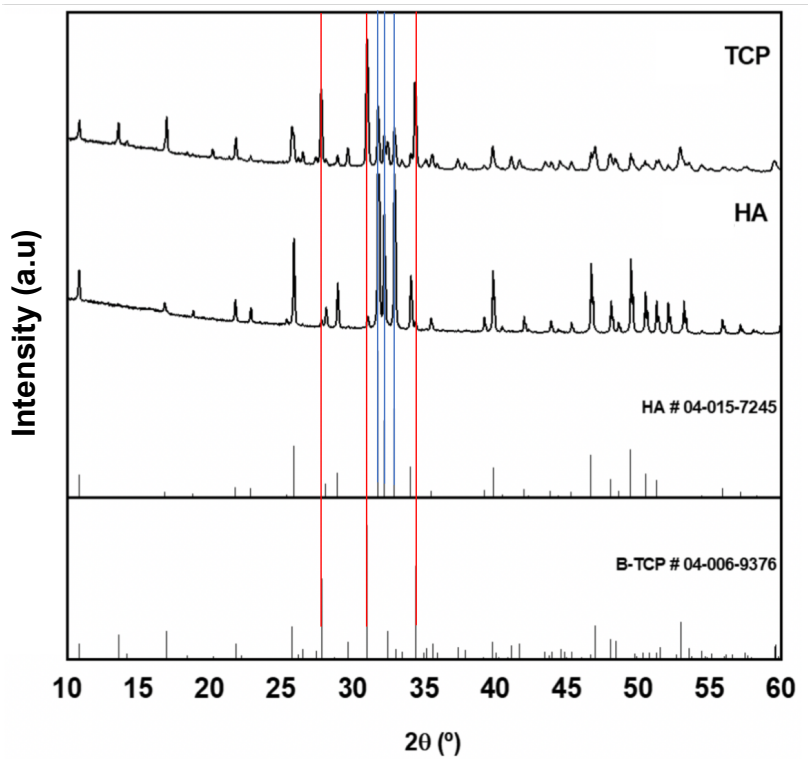


**Figure 21 - XRD analysis of BCP powders.** XRD patterns of the BCP powders and the crystallographic information files used to characterize the powders. The patterns showed that both powders are biphasic and constituted by a HA phase and a β-TCP phase in different proportions. Blue lines – three more intense peaks of HA; Red lines – three more intense peaks of β-TCP.

The powders were structurally characterized by ATR-FTIR (Figure 22). By analyzing the spectrum of each powder, it was possible to identify characteristic peaks of the functional groups of HA and TCP – hydroxyl groups ($OH^-$) and phosphate groups ($PO_4^{3-}$), being the latter characteristic of both HA and tricalcium phosphates.

On the spectrum of HA powder (Figure 22) it was possible to identify two intense peaks at 3570 $cm^{-1}$, 630 $cm^{-1}$, characteristic of O-H stretching vibration and liberation vibration of hydroxyl groups, which together with the peak at 475 $cm^{-1}$ arising from O-P-O bending vibration constitute the characteristic peaks of hydroxyapatite. In the same spectrum it was also possible to observe peaks at 574 $cm^{-1}$ and 609 $cm^{-1}$ attributable to symmetric and asymmetric bending vibrations of phosphate groups. Additional peaks were found at 966 $cm^{-1}$ and 1040 $cm^{-1}$ and 1090 $cm^{-1}$, characteristic of symmetric and asymmetric P-O stretching vibration.

On the other hand, in the spectrum of TCP powder (Figure 22) it was possible to observe characteristic peaks of O-P-O bending vibrations in β-TCP at

435 $cm^{-1}$ and 550 $cm^{-1}$, this last one characteristic of crystalline β-TCP. The presence of this CaP phase is also in accordance with the appearance of characteristic peaks at 940 $cm^{-1}$ and 970 $cm^{-1}$, the latter corresponding to symmetric P-O stretching vibration in crystalline β-TCP. However, an evidence of the biphasic composition of this powder is supported by the presence of a peak at 3570 $cm^{-1}$, attributable to O-H stretching vibration of hydroxyl groups, together with the typical peak at 474 $cm^{-1}$ characteristic of O-P-O bending vibration in hydroxyapatite. The peaks at 574 $cm^{-1}$ and 609 $cm^{-1}$, belong to bending vibrations of phosphate groups and the ones at 1043 $cm^{-1}$, 1079 $cm^{-1}$ and 1111 $cm^{-1}$ correspond to asymmetric P-O stretching vibration, being the last peak characteristic of β-TCP.

Due to the presence of characteristic peaks of each CaP phase, the composition of each powder could be determined by comparing the relative intensities/areas of peaks characteristic of hydroxyapatite (3570 $cm^{-1}$, 475 $cm^{-1}$ and 630 $cm^{-1}$) with the ones characteristic of β-TCP (435 cm-1, 550 cm-1, 940 $cm^{-1}$, 970 $cm^{-1}$ and 1111 $cm^{-1}$). For example, the peak at 435 $cm^{-1}$, characteristic of β-TCP phase is more intense in the spectrum of TCP powder, while in the one of HA powder this peak was not observed. On a similar rational, the peak at 475 $cm^{-1}$ characteristic of hydroxyapatite is more intense in the spectrum of HA powder than in the one of TCP powder (Figure 22). This is in accordance with the results from X-ray diffraction, confirming the biphasic composition of the powders. On both spectra, the peaks found were in accordance with the ones reported in literature for similar calcium phosphate based materials [60], [78]–[80].

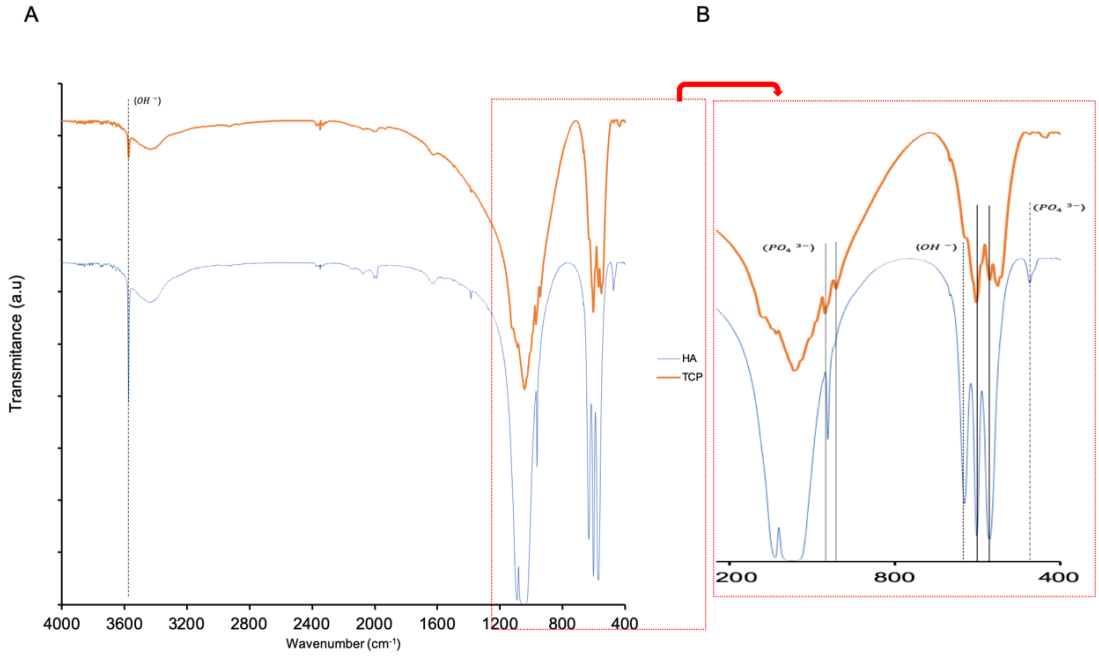


**Figure 22 – ATR-FTIR Spectra of the ceramic powders.** A) ATR-FTIR spectra of HA (blue) and TCP (orange) powders plotted in the same graph; B) zoom of the region between 1200 $cm^{-1}$-400 $cm^{-1}$ – region of the spectrum where the main peaks of calcium phosphates appear. It is possible to observe the appearance of the characteristic peaks of calcium phosphates in both spectra, but with some differences – the different proportion of HA and β-TCP phases in each powder.

The particle size (PS) and particle size distribution (PSD) are extremely important parameters in the formulation of printable inks. As a result, the PSD (Figure 23) was determined for both powders. The size distribution curves present some differences. For HA powder, the majority of the particles represent a population measuring less that 1.4 μm, while the TCP powder has a more heterogenous distribution. Results show that TCP powders can be divided in 2 populations, one constituted by smaller particles (until ~ 1μm) and other composed by particles with higher diameter, probably aggregates.

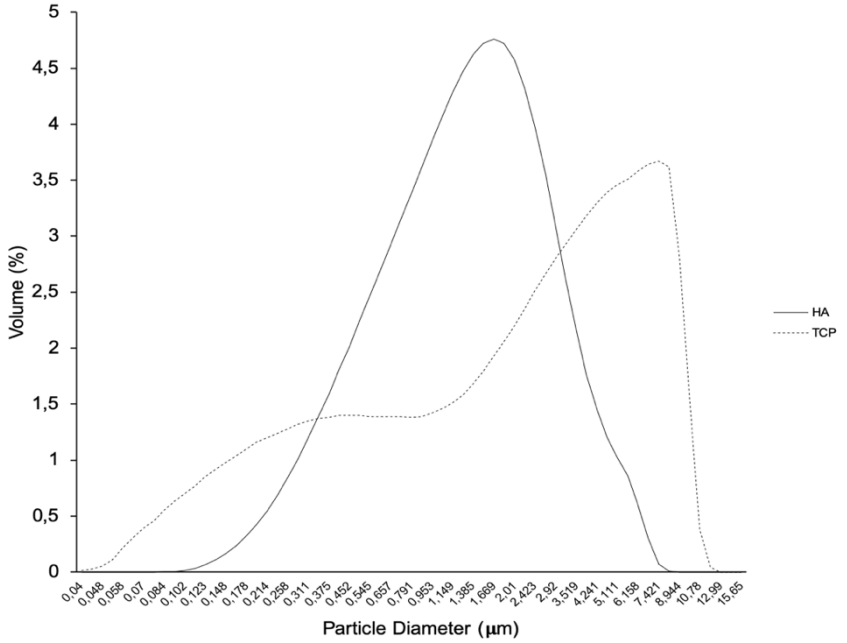


**Figure 23- Particle Size Distribution (PSD) of the powders.** The PSD of the powders isn't similar, being the HA powder PSD more centered and homogeneous. The PSD of TCP powder show the presence of two populations.

For each powder the mean and the median values ($D_{50}$) of the particle size distribution were calculated. For HA powder the PSD has a mean value of 1.724 µm and a $D_{50}$ of 1.396 µm. For the TCP powder the values obtained were 3.237 µm for the mean value and 2.429 µm for $D_{50}$. While for the HA powder the mean value of PSD is relatively similar to the one of $D_{50}$, for TCP powder these two values present higher discrepancy.

A powder with a heterogeneous PSD can be advantageous. Small size particles expose higher surface areas and are more prone to form agglomerates. On the other hand, a PSD with a suitable packing behaviour would allow the preparation of suspensions with high solid loading, with the finer powders occupying the interstitial spaces left by the coarser ones [71]. By having two powders with different size distributions, we can have the best of the two situations, achieving an ink with high packing behaviour and consequently with high solid content.

The main goal is to develop scaffold following a suitable strategy to be applied in BTE. The material has to mimic the bone structural features. Such similarity should be provided by the use of inorganic ceramic powders. HA is considered the material most similar to the mineralized constituents of hard tissue

and is osteoconductive [81]. β-TCP has been used extensively in bone regeneration due to its osteoconductive and osteoinductive properties [82].

It was demonstrated by XRD that both powders supplied consisted essentially of well-crystallized HA and β-TCP phases in different proportions, thus exhibiting a biphasic composition. The qualitative biphasic composition of the powders has also been proven by ATR-FTIR. While hydroxyapatite would mimic the natural bone composition, the β-TCP would provide resorbability to the material [81], [83]. Furthermore, the high volume fraction of powder is one of the most important parameters to develop an extrudable ink [43]. The production of an ink with high solid content may avoid the occurrence of shrinkage and improve the mechanical integrity of the final scaffolds [60].

## 2.3 Hybrid organic-inorganic KGM-BCP extrudable ink

In order to obtain a printable KGM-BCP ink it was necessary characterize and optimize several issues. We must firstly guarantee a good polymeric solution that can act as the organic support of the inorganic powders.

After initial macroscopic evaluation of solutions with different KGM concentrations, the viscosity of a 3 wt% KGM aqueous solution was characterized by rheology (Figure 24A). Results displayed in Figure 24A showed that the shear viscosity of the polymeric solution increases until a value of shear stress of 10 Pa, reaching a *plateau* afterwards. From 20 Pa to 100 Pa the shear viscosity decreases as it can be observed with more detail on Figure 24B.

The final ink formulation was obtained by mixing the 3 wt% KGM solution with 40 wt% of powders, from which 70% is HA powder and 30% TCP powder. Preliminary tests showed that formulations with less than 40 wt% of solids did not fill the criteria necessary to produce an extrudable ink, presenting less mechanical integrity and viscosity. On the other hand, formulations with more than 40 wt% solids did not render an ink but a brittle, non-fluid paste. Taking into consideration the results obtained from XRD (Figure 21), the ink has a final concentration of 78.6% of HA and 21.4 % of β-TCP.

The viscosity of the ink was characterized by rheology (Figure 24C). The obtained results suggest that the shear viscosity of the ink increases until a value

of shear stress of 20 Pa. From 50 Pa until 100 Pa the shear viscosity decreases. This behavior is clearly observed on Figure 24D. Moreover, it could be observed on the graph of the Figure 24D that for all the values of shear stress applied the shear viscosity increases with time reaching a *plateau*.

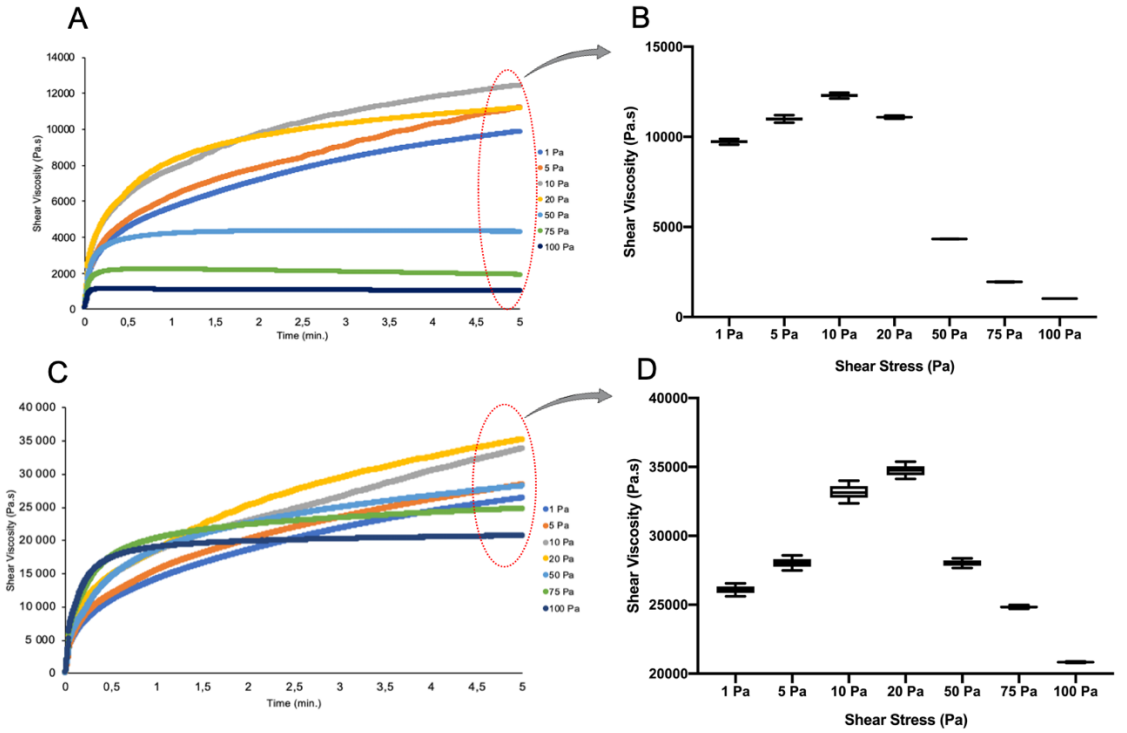


**Figure 24 - Rheological characterization of KGM solution and Ink.** A) and C) Evaluation of shear viscosity with time for different shear stress values of KGM solution and ink, respectively. On the graphs it is possible to observe the shear thinning behaviour – an important feature of solutions that are extruded. B) and D) Graphic representation of plateau value of infinite shear viscosity – another characteristic of the extrudable solutions.

On Figure 25 it was plotted the changing of the shear viscosity with time (on a total of 5 min.) for the different shear stress applied on the KGM and ink formulations. Although the patterns were similar, the values of shear viscosity achieved for the ink are much higher than the ones achieved for the KGM solution alone. The addition of solids leads to an increase of shear viscosity on a range of 60%-90%. This increase in viscosity was clearly observed for higher values of shear stress.

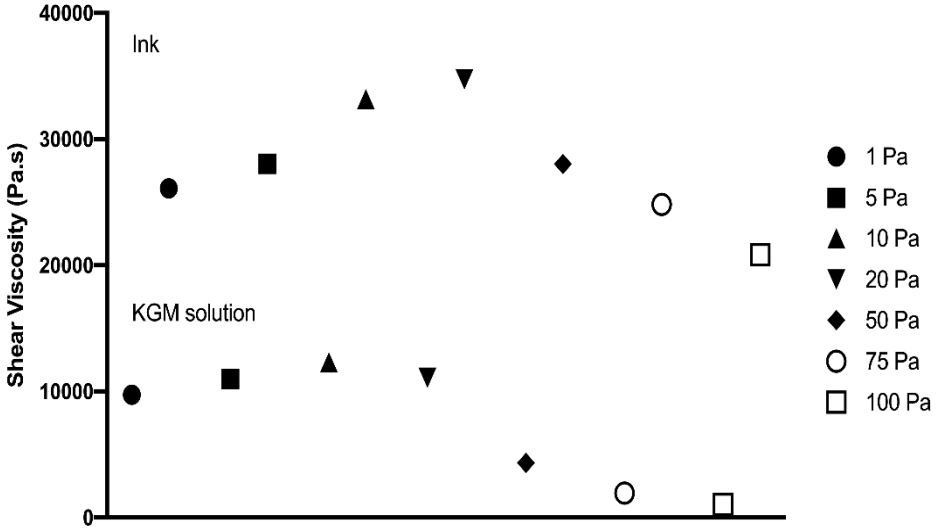


**Figure 25 - Shear Viscosity pattern of the Ink and KGM solution**. Through the analysis of the graph it is possible to observe the influence of the addition of the powders to the KGM solution, leading to an increase of 60 % in the shear viscosity. For higher shear stress values, the shear viscosity can increase to a difference of 90 % - Stability of the ink in relation to KGM solution for higher shear stress values.

The rheological behavior of the ink in robocasting is one of the most important aspects for achieving successful printing [42]. An ink to be used in robocasting should be depositable and printable [84]. Analysis of the Figure 24A and C suggests that the polymeric solution by itself present a desirable behavior and that behavior isn't lost after the addition of the ceramic powders [42]. By analyzing the graphs of the Figure 24A and C, three different phases can be observed. It starts by an initial phase, where low values of shear stress are applied and the shear viscosity increase. On polymeric based inks, this situation can be explained by the conformation of the molecules - when no shear is applied, some molecules have a complex entangled spherical form, while others are partially disentangled. When a low shear is applied, the molecular collisions increase the viscosity, and the entangled molecules collisions contribute to molecular disentanglement [85]. The second phase starts with the increment of shear rate. In this phase, disentanglement and orientation in the shear direction happens for more and more molecules, and resistance to shear and viscosity decreases, constituting the desirable behavior of an extrudable ink. When this phenomenon is observed, the formulation has a shear-thinning behavior. An ink for robocasting should steadily flow under the applied shear stress without clogging the nozzle. Furthermore, it should become thinner under shear to facilitate extrusion [85], [86].

By the analysis of Figure 24A and C, the formulation developed on this work has the desirable behavior for robocasting. From a value of shear stress of 20 Pa until 100 Pa the viscosity of the ink decrease. Although the polymeric solution presents a similar trend, in this case the viscosity stars decrease from the 10 Pa until to 100 Pa. The last phase occurs when the viscosity doesn't change with the time. After reaching a certain shear rate value, the population of macromolecules achieve a state of maximum disentanglement. This is called plateau value of infinite shear viscosity. This phenomenon was observed in both situations – KGM solution an ink – and is demonstrated in more detail in the Figure 24B and D. For each value of shear stress there is a maximum state of orientation of the molecules, reaching a plateau of the shear viscosity for that shear stress [85].

When the ink exhibits a phase of shear thinning behavior, it is able to be extruded by an Additive Manufacturing machine (i.e. the viscosity remains below a certain threshold) [84]. A 'printable' ink should have a given viscosity so that tracks of material remain their shape during processing, but also slump a certain amount to assure connection between the tracks. This aspect is crucial to maintain adequate dimensional control [84], since the ink should be capable of maintaining its shape after printing, supporting its owner weight [43]. This last condition is largely influenced by the addition of solids [84].

A higher content of solids turns the formulation more stable, and such stability is perceptible on the three phases described above (Figure 25):

- With the addition of powders, the viscosity increases until the value of shear stress of 20 Pa, meanwhile for the KGM solution this situation occurs until 10 Pa;
- The values achieved in each shear stress value are much higher after the addition of powders - the maximum value increase from 13 000 Pa.s to 36 000 Pa.s
- When the viscosity starts to decrease, this phenomenon is more accentuated in the KGM solution when compared with the ink formulation. While on the ink formulation, the viscosity decreases around 46%, from 36 000 Pa.s to 21 000 Pa.s, for the KGM solution there is a decrease of approximately 92%, achieving very low viscosity values. Thus, it can be concluded that the polymeric solution *per se* is not an adequate printable formulation. The addition of the

maximum content of solids without compromising the viscosity was fundamental to render a printable ink formulation.

It is well known that the addition of solids increases the viscosity of the formulation. Therefore, the optimal solids volume fraction should consist in a balance between these two desirable but incompatible features: a maximum solid loading, and a relatively low viscosity that determines the easiness of preparation, handling and casting of the suspensions. In this work, the addition of solids increases the viscosity of the formulation in 60% (this value can achieve the 90% due the instability of the KGM solution when exposed to higher shear stress values), but the ink maintains the adequate rheological properties. Thus, it can be concluded that we were able to obtain a KGM-based ink with high shear thinning behavior, able to be extruded through fine nozzles, and to retain a degree of strength and stiffness to be self-supporting following printing, offering mechanical support to the subsequent layers [43], [86].

## 2.4 Production and characterization of the hybrid organic-inorganic KGM scaffolds

After obtaining an ink with adequate characteristics, the scaffolds were obtained by robocasting. This technique allowed a layer-by-layer deposition of the ink, building a 3D hybrid organic-inorganic scaffold that could be stabilized after immersion in ethanol. The scaffolds were characterized by SEM to investigate their macro and microstructural features (Figure 26). By analyzing the pictures of macro scale (lower magnifications), it was possible to determine the real value of the pore size and fiber diameter, which were 494 ± 31 μm and 372 ± 39 μm, respectively. A good regularity of the structure of the scaffold has been observed, as well as a straight geometry of the rods and their mutual extensive adhesion. Deformations of the rods were not observed. These morphological features are important to obtain scaffolds with a reasonable mechanical strength for tissue engineering applications [60]. Although we were not able to perform compressive tests to further characterize the mechanical properties of the scaffolds due to time constrains, those experiments are currently being prepared. At a micro scale it was possible observe that the ink isn't homogeneous, exhibiting the presence of agglomerates (Figure 26B i) and iii)). We could

successfully see the interface between the polymer and the powder grains on Figure 26B iv). The powders exhibited a smooth morphology and seem clearly involved by the polymeric support.

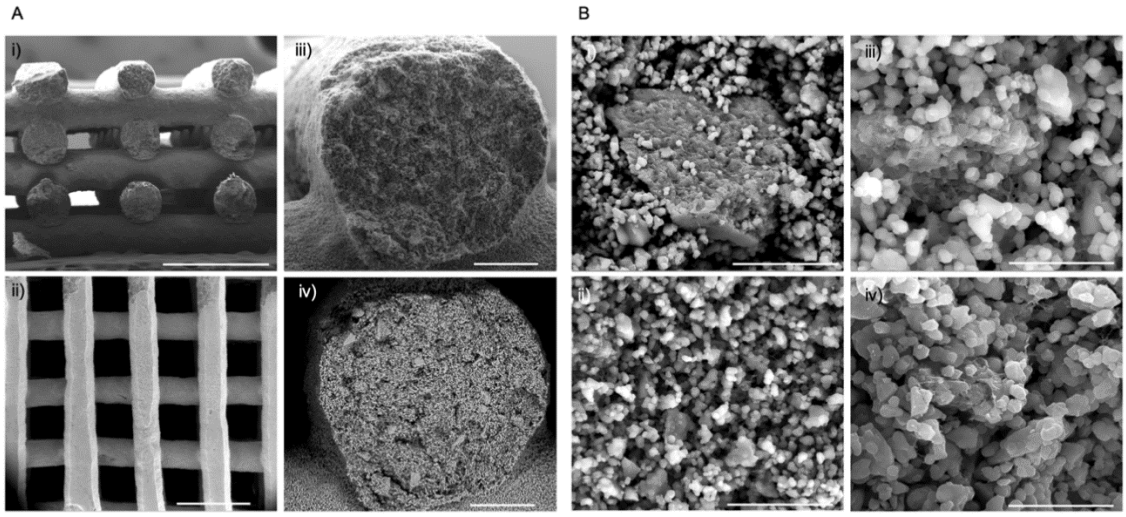


**Figure 26 - SEM images of KGM scaffolds.** A) Macro characterization of the scaffolds: i) lateral view; ii) top view; iii) and iv) rod detail obtained through secondary and backscattered electrons, respectively. On this last one it is possible to observe the presence of two phases in the structure of the scaffold. B) Micro characterization of the scaffolds: rods' inner fractured cross sections where it is possible to observe in more detail the 2 phases: i) and iii) formation of agglomerates were observed in all the scaffold. On pictures ii) and iv) it can be visualized the size and shape of the grains of the powders and interaction with the polymer. Scale bar: A) i) and ii): 1mm; iii) and iv): 100 µm; B) i) and ii): 10 µm; iii) and iv) 5 µm. Magnification: A) i): 100x; ii): 70x; iii) and iv): 600 x; B) i) and ii): 10000 x; iii) and iv) 20000 x.

Moreover, the grain size and shape could be measured by the analysis of Figure 26B iv). The grains had a size between 0.53 µm and 1.167 µm, giving a mean value of 0.743 ± 0.21 µm. The values obtained are in accordance with the ones measured in PSD of the powders. Although the non-homogeneity of the ink can be problematic for its extrusion by robocasting [42], some roughness that is conferred to the surface of scaffolds can have great benefits for their performance in *in vitro* studies. Surface topography is a parameter crucial for cell over-survival and proliferation. It is very well described on literature that the quality of cell attachment influences the cell morphology as well as their proliferation and differentiation ability and that is related with the surface texture [60], [87]. Different studies suggest that as the roughness and disorder of surfaces increase, differentiation and/or extracellular matrix synthesis increases [87]. Thus, the obtained heterogeneity of the ink can be a key feature for a successful application of KGM scaffolds in *in vitro* studies. Assessment of surface topography will be performed in future experiments.

The pore size introduced on the CAD software (500 μm) was relatively similar to the real value measured through SEM images. This situation was expectable because no drops of the rods are observed in SEM images.

A scaffold for osteogenesis should mimic bone morphology, structure and function in order to optimize integration into surrounding tissue. Bone is a tissue that naturally is porous and pores and very important for a healthy tissue and all the functions of them being ensured. Then, pores are necessary for the formation of bone tissue and allow migration and proliferation of osteoblasts and mesenchymal cells, as well as vascularization. In addition, a porous surface improves mechanical interlocking between the implant biomaterial and the surrounding natural bone, providing greater mechanical stability at this critical interface [88]. Several studies show the influence of the pore size in *in vivo* osteogenesis [88], [89]. The minimum requirement for pore size is considered to be 100 μm due to cell size, migration requirements and transport. However, pore sizes > 300 μm are recommended, due to enhanced new bone formation and the formation of capillaries. Because of vascularization (a very important process during *in vivo* osteogenesis), pore size has been shown to affect the progression of osteogenesis. Small pores favored hypoxic conditions and induced osteochondral formation before osteogenesis, while large pores, that are well-vascularized, lead to direct osteogenesis (without preceding cartilage formation) formed bone [88]. The choice of 500 μm as the pore size of the constructed scaffolds in this work was based in previous results obtained in an unpublished work performed in our lab, where the effect of the porosity of biphasic calcium phosphate scaffolds on osteogenic differentiation of hMSCs was investigated. In this work the better results were obtained in the scaffolds with 500 μm of pore size. The results proved that these scaffolds have osteoinductivity properties without the addition of osteoinductive exogenous factors, corroborating reports from the literature [90]. In relation to the fiber diameter, the situation isn't very different. The real value is near to the theoretical value of 410 μm.

## 2.5 KGM scaffolds *In vitro* behavior assessment

After the production and physico-chemical characterization of the developed 3D KGM scaffolds, it is essential to investigate some important parameters such as the stability on culture conditions, possible cytotoxic effects and the ability to allow and support long-term cell attachment and proliferation.
We used hMSCs since they represent promising cell sources for bone engineering because of its osteogenic capacity under certain conditions [91]. Several studies demonstrate the osteogenic capability of MSCs cultured on calcium phosphate ceramics (CaPs), as well as showing that adhesion, localization, ECM deposition and cell differentiation is affected by design and pore geometry of the scaffolds [92].

### 2.5.1 Cytotoxicity of KGM scaffolds

Calcium phosphate based and materials are well established in literature as high potential biomaterials for bone regeneration [93], [94]. However, when developing new scaffolds to be used in TE, assessing their cytotoxicity is essential. For that, direct and indirect contact tests were performed according to the ISO 10993-5 standard practice. Figure 27 presents the metabolic activity for KGM scaffolds developed in this study. The constructs proved to be non-cytotoxic as both direct and indirect contact assays showed cell metabolic activity values above the required 70% of the control's (normalized to 100%) measured value.

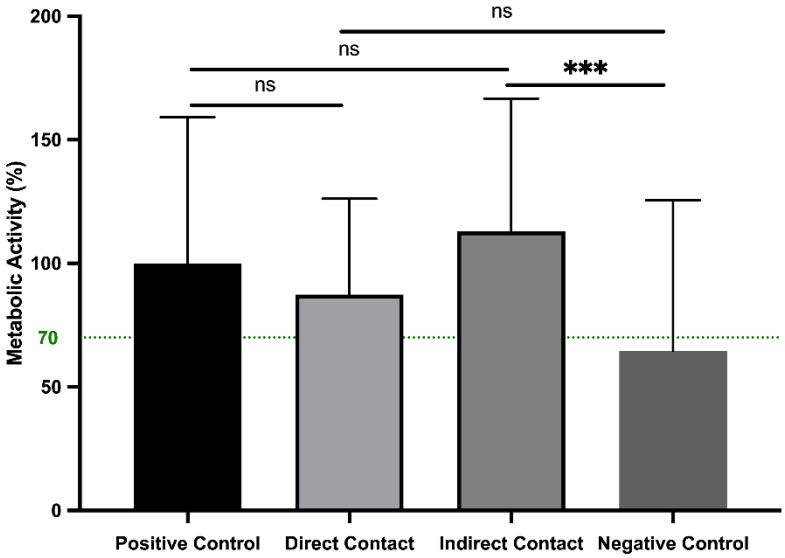


**Figure 27 - Metabolic cell activity of the cytotoxicity tests.** The tests performed are resazurin based assays and values above 70 % were obtained for direct and indirect contact. Statistically significant differences are marked with * ($p < 0.05$), ** ($p < 0.01$), *** ($p < 0.001$) or **** ($p < 0.0001$), ns. means not statistically significant.

Moreover, the metabolic activity for the indirect contact test was higher (an increase of about 12%) than that of the control. Indirect contact test assesses the leachables effects on the cells and it is not surprising that CaP could be enhancing cell metabolic activity of hMSCs. Negative control is higher than expected since an experimental error calculating DMSO concentration to use was detected. These positive results seem promising for further future biological studies.

### 2.5.2 hMSC differentiation on KGM scaffolds

#### 2.5.2.1 Metabolic cell activity of hMSC on KGM scaffolds

After scaffold sterilization, previously optimized cell density was used to perform the initial seeding. Briefly, 13600 hMSC cells concentrated in a 20 µL droplet was added to each scaffold and cells were let to adhere on top of KGM scaffolds for 30 min. and only after this time, culture media was added to the individual scaffolds. hMSCs were cultured on KGM scaffolds for 28 days under basal and osteoinductive media after an initial 7 days period to allow cell proliferation. After defined timepoints, samples were evaluated for cell metabolic activity and morphology (Figure 28).

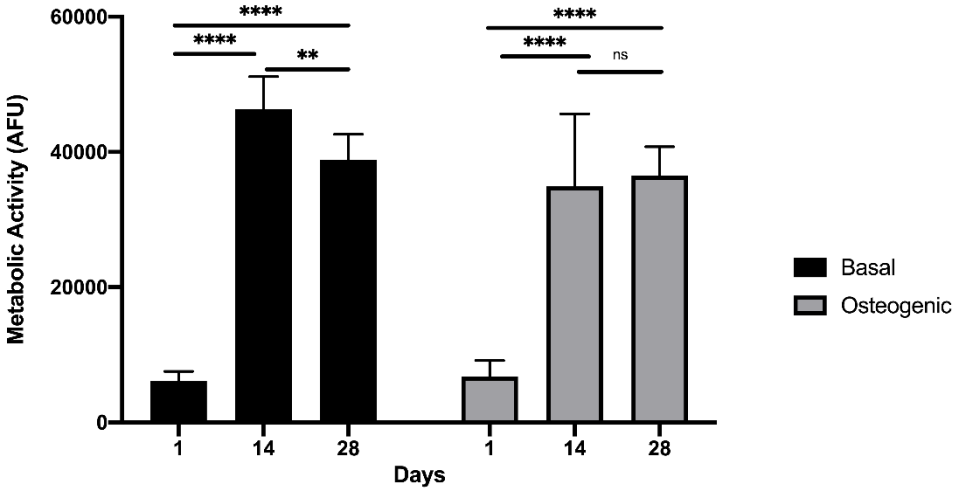


**Figure 28 – Metabolic cell activity of hMSC on KGM scaffolds.** An increase on the metabolic cell activity from day 1 to day 14 is verified for both conditions. From day 14 to day 28 a little decrease is verified for osteogenic condition, being non-significant. For basal conditions, there are an accentuated decrease on the value of the metabolic activity. However, the value achieved on the day 28 in this condition is similar to the values of osteogenic condition. Statistically significant differences are marked with * ($p < 0.05$), ** ($p < 0.01$), *** ($p < 0.001$) or **** ($p < 0.0001$), ns. means not statistically significant.

The metabolic activity of hMSCs cultured on scaffolds was measured using the resazurin-based method after 1, 14 and 28 days. On Figure 28 we can observe that comparing the metabolic cell activity of Day 1 in both conditions, the values are very similar and no significant differences are verified. This result may indicate a homogeneous and efficient seeding of the hMSCs on the scaffolds.

The hMSCs remained viable and metabolically active throughout the 28 days of culture in all scaffolds, with a continuous increase in cells metabolic activity for both basal and osteogenic conditions up until the 14$^{th}$ day. However, a decrease in metabolic activity values was detected from 14 to 28 days in both basal and osteogenic conditions (Figure 28). This decrease was not statistically significant for the osteogenic condition, probably due to the already lower value for metabolic activity level at day 14 at but the decrease detected in basal condition from 14 to 28 days was considered statistically significantly lower. The statically significance between the two conditions for the different timepoints is on Table S3 in the Supplementary Material.

It is reported that in the presence of differentiation inductors, there is a metabolism-shift on hMSCs and them proliferate less on osteogenic conditions when compared with basal conditions, probably due to the metabolic shift [94]. After 14 days in culture this tendency was verified. Moreover, as was mentioned previously, with the differentiation process, there are a decrease on cell proliferation [87]. Though no proliferation marker was used in this study at this point, it can clearly be observed the difference on the number of cells throughout time in culture (Figure 28, Figure 29) justifying the increase of the scaffold occupancy by the hMSCs.

We can hypothesize that the lower resazurin levels after 28 days compared to the levels of metabolic activity for 14 days in culture can be due to limitations of the resazurin assay. After 28 days an intricate mesh of extracellular matrix proteins is deposited on the structure of the scaffold, the cells and the secreted matrix are occupying not only the scaffold fibers but also the pores. This causes constrains to the free flowing of resazurin solution and the retrieved solution after the 3h incubation could not get into the interior part of the pores/scaffold.

#### 2.5.2.2 hMSCs morphology on KGM scaffolds

Cells attach and spread when in contact with an adequate surface through adhesion proteins-dependent processes. The quality of cell attachment affects the cell morphology as well as their proliferation and differentiation ability [87]. Microscopic analyses were used to evaluate the distribution of hMSCs on the KGM scaffolds after 1, 14 and 28 days in culture (Figure 29) and revealed that cells were well were able to adhere to the scaffold surfaces (Figure 29 Day1). An increase on cell density from day 1 to day 14 can be observed since after 14 days the side of scaffolds was completely covered with cells, indicating their survival, on both basal and osteogenic. Moreover, seeing in detail the morphology of the cells 24 h after the seeding, it is possible to observe that cells exhibit a nearly polygonal shape with a multiple filopodia attached to the scaffolds (Figure 29 day 1).The absorption of proteins integrins (major cell receptors involved in the cell-binding-to-matrix) from culture mediums determines the early non-specific stage of cell adhesion, enabling cell spreading on the scaffolds through the formation of a conditioning protein layer that promotes this adhesion [43],[44]. Moreover, the surface area (total of porosity and microporosity (Figure 26)) facilitate the wettability of the scaffolds and provide much more contact points for protein anchorage. Visual inspection at 7 days in culture (data not shown) showed that in some areas of the scaffolds, cells were already disposed in a monolayer with cell-to-cell contact, partially coating the materials surface. After 14 days in culture, hMSCs were visible on the top surface of the 500 μm pore size scaffold, linking the structure´s filaments.

The morphology of the hMSCs on the scaffolds is shown in confocal images of Figure 29 and assessed by labelling f-actin filaments (green) and nuclei (blue), in basal and osteogenic medium, after 14 and 28 days in culture.

Collagen type I was also assessed by immunocytochemistry and visualized by confocal microscopy. We could detect a dense collagen-enriched matrix network as it is depicted in Figure 30 increasing along time.

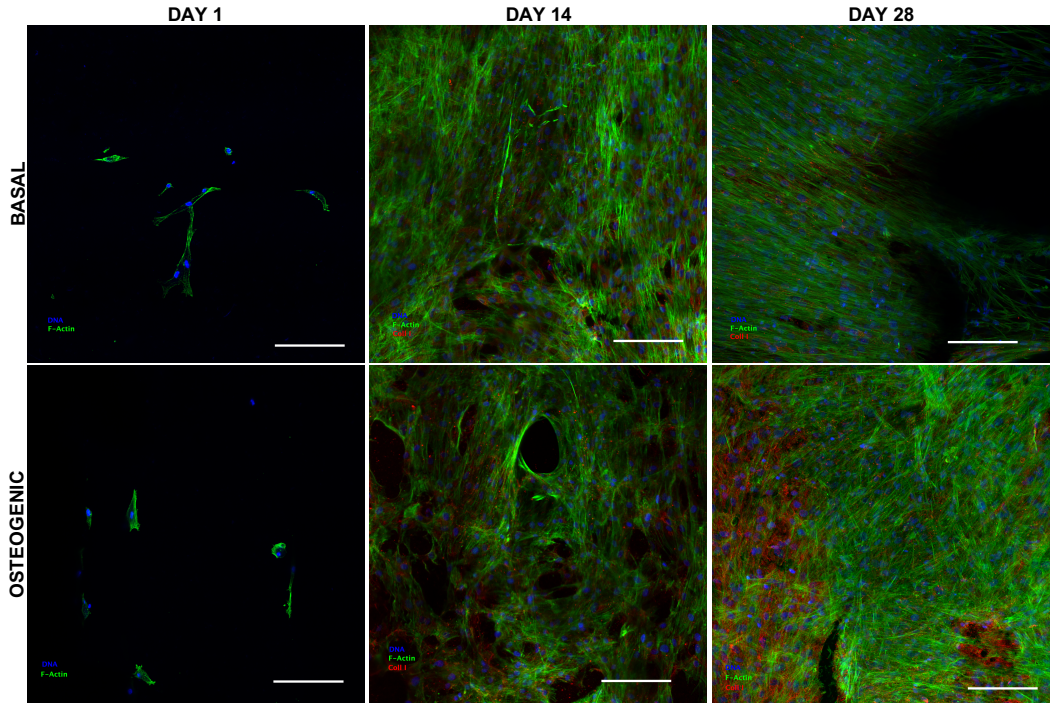


**Figure 29 - hMSCs morphology on KGM scaffolds.** Representative confocal microscopy images from the different timepoints, for both conditions, stained for nuclei (blue), F-actin (green) and Collagen type I (red). Analyzing the images is possible verify the proliferation and migration of the cells. A big difference is verified from day 1 to day 1, for both conditions. The cells proliferated and occupied all the scaffolds. At day 28 this cellular increase is even more evident. Moreover, the expression of Collagen type I is verified from day 14. (Scale bars: 100 μm)

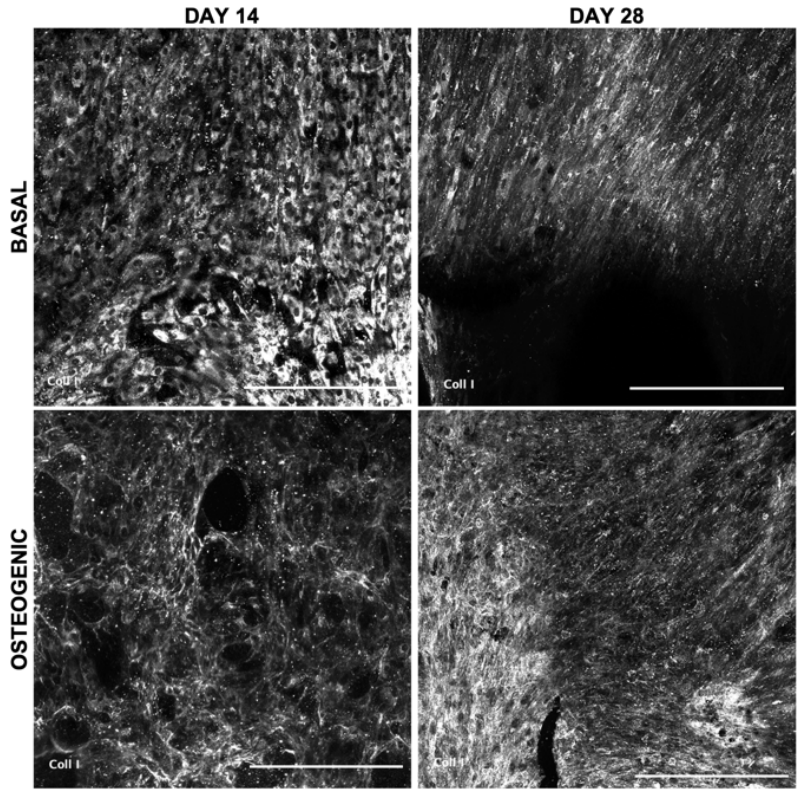


**Figure 30 – Collagen type I expression on KGM scaffolds.** Representative confocal microscopy images from the different timepoints, for both conditions, stained for Collagen type I. The expression of Collagen type I is verified from day 14 in both conditions. At this time point in basal conditions collagen is intracellular, but at day 28 is forming a dense matrix such as in osteogenic condition. (Scale bars: 100 μm)

Total protein content was also quantified using the BCA assay. The results depicted in Figure 31 highlight the increase on protein content from 1 day to 14 days in culture, but surprising results of total protein content for 28 days aren't achieved. From the immunostainings is evident that the amount of protein increases from the day 14 to the day 28 in culture. However, results obtained for this timepoint are lower than the obtained for the 14 days by the BCA assay. The same trend was detected for the DNA quantification by PicoGreen assay (not shown).

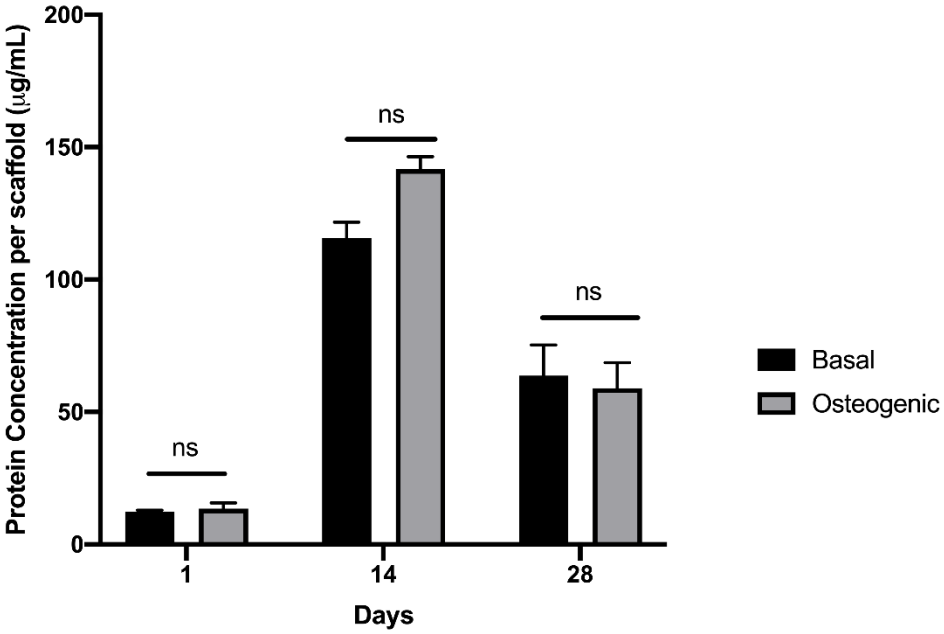


**Figure 31 – Total Protein concentration during the differentiation assay**. At day 1 the values are very similar, what is expectable. From day 1 to day 14 there are an increase for both conditions and a decrease from day 14 to day 28. However, significant differences aren't verified between the conditions and the different time points. ns means not statistically significant.

The problem detected is related to the detaching of the cells and ECM solubilization from the scaffold. This procedure is extremely important for the performance of various tests, such as those mentioned above.

However, there are several parameters that need to be optimized in this procedure, such as the type of enzymes, concentrations and incubation times that are necessary to use. These aspects are specific for each system and the difference between systems and inside of a system are reported in the literature [95], [96].

The non-significant differences found in the total protein content during the assay (data not shown) aren't surprising and may be explained by the fact that a cell in the different phases (proliferation, differentiation, etc) have to produce

different proteins. When is in the differentiation process, it will produce more matrix related proteins, meanwhile when in the proliferation phase will produce more intracellular proteins and proteins enough to the mitotic process.

But, in all cellular processes proteins are necessary and as in this type of assay isn't possible to distinguish the exact protein present, the total protein content tends to stabilize, because when the production of a certain type of protein related to one phase finishes, the production of other type of proteins starts.

#### 2.5.2.3 ALP quantification

In scaffolds containing CaP components standard colorimetric stainings such as Alizarin red, and Von Kossa colorations are not the ideal approach to test the differentiation into the osteogenic lineage. In this study we used ALP enzymatic assay to validate the osteogenic differentiation. A successful differentiation is usually revealed by their capacity to express ALP, as well as type I procollagen [89].

ALP is a functional enzyme, which plays a key role in bone formation and mineralization and has always been related to osteoblast differentiation [97]. In order to evaluate the efficiency of the osteogenic differentiation we performed an enzymatic ALP assay produced from hMSCs (Figure 32).

Extracellular matrix production occurs immediately following the proliferation of pre-osteoblasts (after 14 days in culture [98]). It is also at this point that ALP reaches its peak of activity, as it is necessary for the last stage of differentiation - mineralization. In other words, ALP activity should increase until day 14 or just before and then begin to decrease as described in the literature [95]. Therefore, time points between day 7 and day 14 will eventually be needed to determine from which day type I collagen expression begins and ALP reaches its peak.

By day 28 and given the time reported for *in vitro* osteogenic differentiation, there will already be mineralization of the matrix produced (last step and marking the end of the development of an osteogenic phenotype), the pre-osteoblasts will have already reached a complete phenotype of osteoblast and ALP activity will already have much lower values [95], [98].

The results we obtained are not reliable but represent a step forward into the optimization of these assays to use in future experiments. Our results are not conclusive since many scaffolds were lost due to the difficulties retrieving the cells, optimization of calibration curves among other technical difficulties.

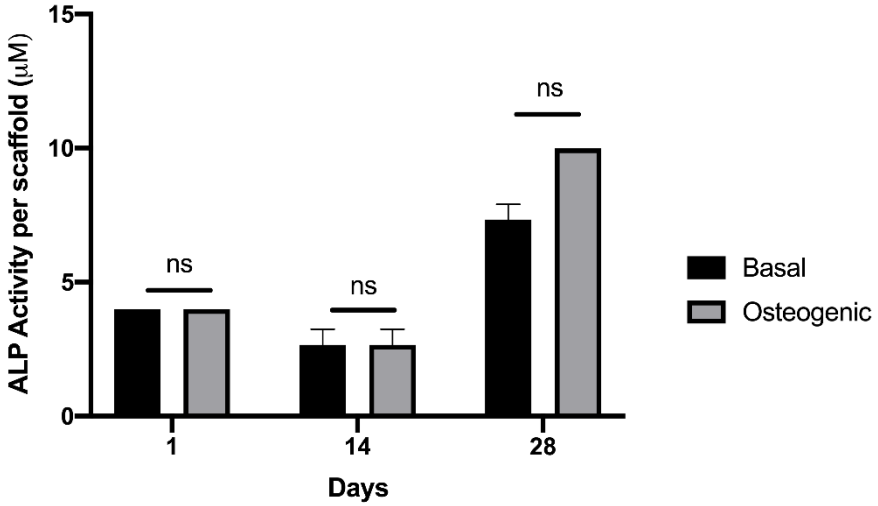


**Figure 32 – ALP concentration during the differentiation assay.** The results obtained are affected by the technical difficulties mentioned above and they aren't reliable. In this assay there aren't significant differences between the different time points and conditions. ns means not statistically significant.

KGM scaffolds produced in this work seems to have the capacity to promote the adherence, survival and proliferation of hMSCs during 28 days of culture both in basal or osteogenic inductive conditions.

With our experiments is possible corroborate the adequate pore size of the produced scaffolds in order to promote all the processes mentioned above and referred in the section of the macro characterization of the scaffold, namely for a further *in vivo* application. Some studies reported in the literature suggest that the pore size doesn't affect the *in vitro* osteogenic differentiation. They suggest, however, that higher pore size promote cell proliferation due to the facilitated oxygen and nutrients transports, making pore size a critical feature for successful *in vivo* implantation [89], [94].

In fact, this system seems to have good potential for osteogenic differentiation to occur, but all of the above inferred timings and suggestions have to be verified and validated. For such optimization of certain procedures, as mentioned above, are extremely necessary for the validation of a successfully related osteogenic differentiation in this system.

# 3. KGM functionalization with photothermal moieties

After the validation of the KGM scaffolds in an *in vitro* setup, the next step consisted in providing these scaffolds with photothermal properties. Thus, we decided to follow two different strategies:

1- Coupling of dopamine to KGM backbone;
2- Development of dopamine particles to include in future ink formulations;

## 3.1 KGM functionalization with dopamine

### 3.1.1 Carboxylation of KGM

Before coupling dopamine to KGM it was necessary modify the structure of the polymer with succinic anhydride - SAC0. This modification allowed the addition of carboxylic groups to KGM through nucleophilic attack of the hydroxyl moieties present in the polymeric chain (Figure 33A).

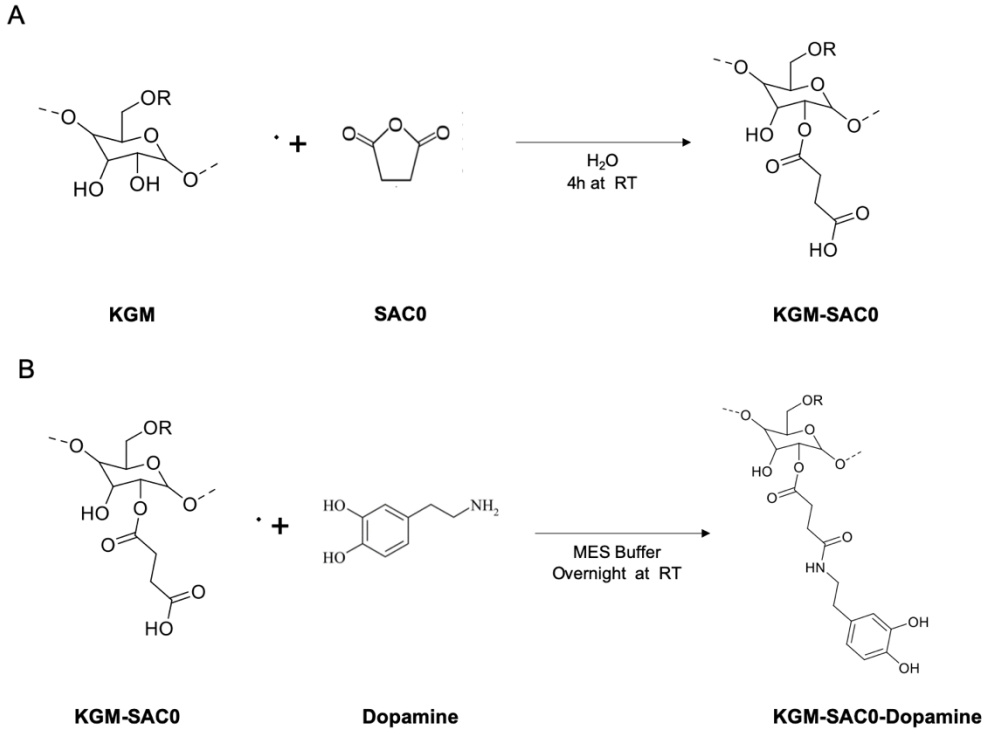


**Figure 33 - Synthetic route for the conjugation of dopamine to KGM.** A) Reaction between KGM and SAC0, in order to functionalize the structure of the polymer with carboxylic groups. These functional groups were introduced for the coupling of the Dopamine with KGM – Reaction B). R= H or $CH_3$.

The success of this first reaction was demonstrated by $^{1}H$ NMR (Figure 34), through the appearance of new peaks at 2.72 ppm and 2.59 ppm corresponding to the hydrogens 9 and 10 from SAC0 moiety (Figure 34A-B). Additionally, the protons corresponding to the glycosidic moiety of the monomer of KGM were also observed. Inclusively, it was well observed the peak corresponding to the hydrogen of the acetylated groups at 2.25 ppm, characteristic of some monomers of KGM.

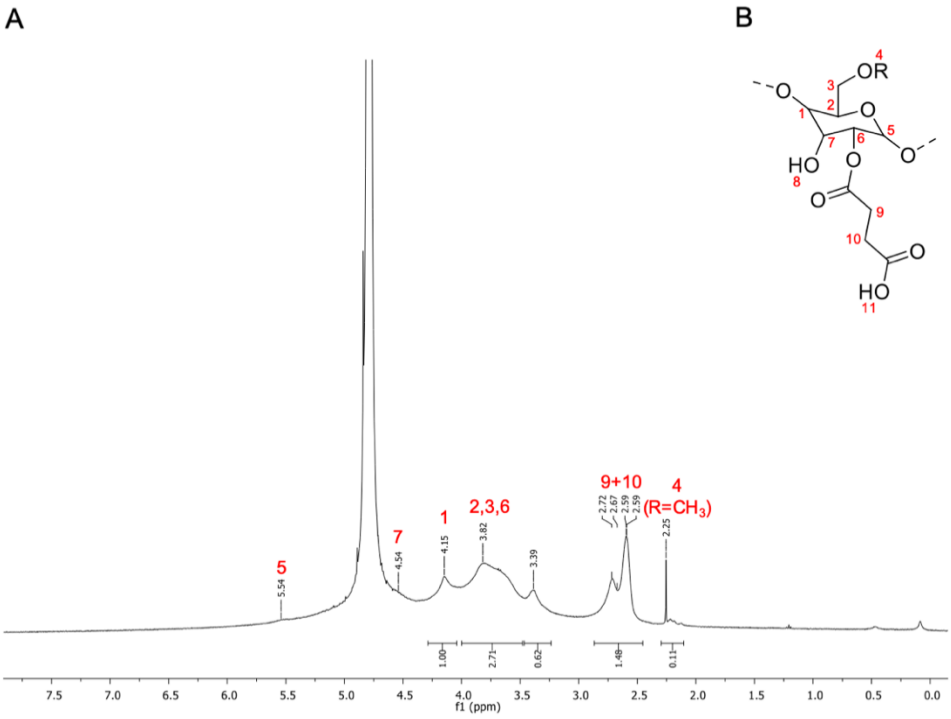


**Figure 34- Incorporation of SAC0 through analysis of $^{1}H$-NMR.** A) KGM-SAC0 spectrum in $D_2O$. Visualization and identification of peaks corresponding to hydrogen groups of the glycosidic unit of the main monomer of KGM and of the hydrogen groups of the aliphatic chain due to presence of the SAC0 molecule (hydrogens 9 and 10). B) Chemical structure of the KGM-SAC0 conjugate.

The amount of conjugated SAC0 was determined by comparison between the peaks integrals corresponding to hydrogens 9 and 10 with the one corresponding to hydrogen 1 of monomeric unit of KGM. It was calculated that 27% of SAC0 could be successfully conjugated to the KGM polymer backbone (Determination of conjugation efficiency on Supplementary material). The relatively low incorporation yield is probably related with the fact that SAC0 is sensible to water and starts degrading in aqueous medium. In a first visual assessment, the final compound KGM-SAC0 was soluble in water and was able

to form a stable pH-sensitive hydrogel, since this hydrogel become soluble at alkaline pH.

The success of this conjugation was also confirmed by ATR-FTIR (Figure 35).

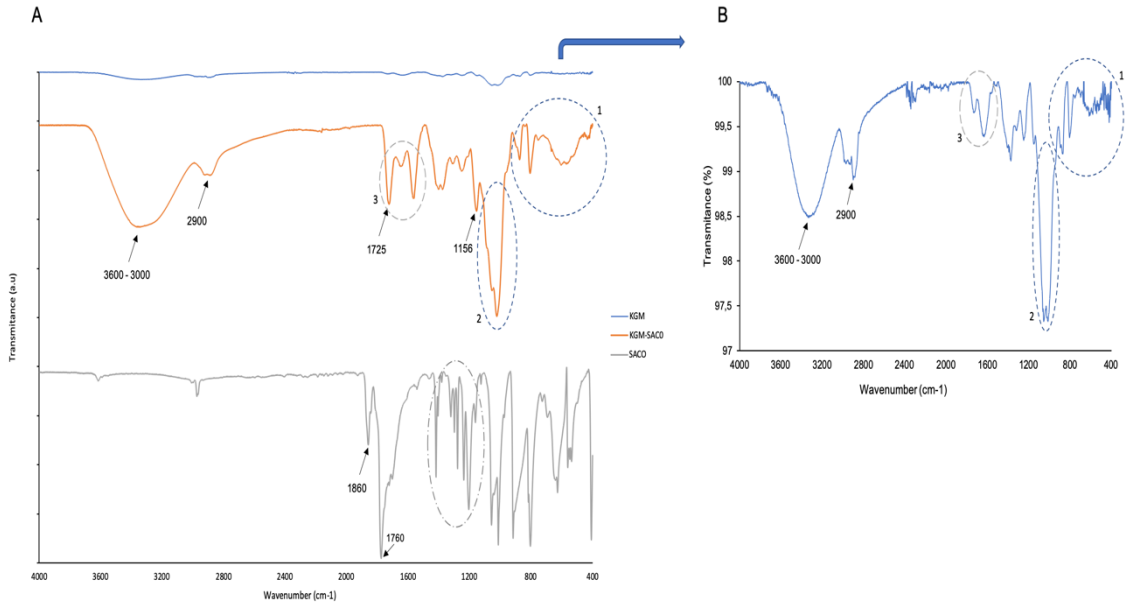


**Figure 35 – Incorporation of SAC0 through analysis of ATR-FTIR.** A) Spectra of KGM, KGM-SAC0 and SAC0 plotted in the same graph. B) KGMs' spectrum in detail. Analyzing all the spectra it is possible to observe similar patterns between the KGMs spectrum and KGM-SAC0 spectrum. On SAC0 spectrum it is visible a set of peaks characteristic of the C=O stretching vibration – characteristic bond of the molecule. A new peak on the KGM-SAC0 spectrum at 1725 $cm^{-1}$ can be due to incorporation of the SAC0 molecule; esters and carboxylic acids presents in the conjugated are responsible for the appearance of the new peak.

KGM-SAC0 spectrum present similar patterns and peaks to the ones of KGM spectrum (Figure 35B), what would be expected. In both KGM-SAC0 and KGM spectra it could be observed a peak between 3600 $cm^{-1}$ - 3000 $cm^{-1}$ (O-H stretching vibration in hydroxyl groups), as well as a peak at 2900 $cm^{-1}$ (C-H stretching vibration in methylene and methyl moieties). In a lower wavenumber region, it was possible to observe a similar pattern between 1100 $cm^{-1}$ to 980 $cm^{-1}$, where peaks characteristic of glycosidic monomeric units (1058 $cm^{-1}$ and 1024 $cm^{-1}$) could be found (Figure 35A-2). Finally, it could be observed in both spectra a similar pattern in the fingerprint region of the compounds, namely between 936 $cm^{-1}$ and 400 $cm^{-1}$. In this range it could be found peaks characteristics of mannose units at 875 $cm^{-1}$ and 805 $cm^{-1}$ (Figure 35A-1).

On SAC0 spectrum is possible verify the presence of peaks that correspond to the functional groups characteristics of the compound: peaks at 1860 $cm^{-1}$ and 1760 $cm^{-1}$ that corresponds to symmetric and asymmetric C=O

stretching vibration in anhydrides; a region between 1418 $cm^{-1}$ and 1156 $cm^{-1}$ (marked region on SAC0 spectrum – Figure 35A gray spectrum) which is attributed to in-plane and out-of-plane C-H bending vibrations of $CH_2$ and C-O stretching vibration in anhydrides.

Taking into account the chemical structure of the final conjugate (Figure 34B), the incorporation of SAC0 should be followed by the appearance of peaks characteristics of esters, aliphatic chains and carboxylic acids in the ATR-FTIR spectrum. In the KGM-SAC0 spectrum it was observed the appearance of a new peak at 1725 $cm^{-1}$, which can result from the contribution of the esters and carboxylic acids. This new peak is the most intense of the set of peaks marked on the spectrum as number 3 (Figure 35A-3). In KGM spectrum this peak isn't present in the marked region. In this spectrum the most intense peak that appear is shifted to lower wavenumbers, at 1640 $cm^{-1}$, which corresponds to C=O stretching vibration in amides and can be related with impurities in KGMs composition. On the region marked as 3 on the KGM-SAC0 spectrum (Figure 35A-3) there is the appearance of another new peak at 1560 $cm^{-1}$ that corresponds to asymmetric C=O stretching in carboxylates. This peak can be related with the dialysis procedure, where some carboxylic groups can deprotonate. This is supported by the differences observed on the region between 1420 $cm^{-1}$ and 1300 $cm^{-1}$ in KGM-SAC0 spectrum when compared with the one of KGM, where peaks characteristic of symmetric C=O stretching vibration in carboxylates usually appear. Moreover, the peak at 1156 $cm^{-1}$ on the KGM-SAC0 spectrum is shifted in relation to KGM spectrum. This peak corresponds to C-O stretching vibration in esters, arising from the functionalization of the polymer. Overall, these findings allowed us to conclude that SAC0 was successfully conjugated to KGM.

As mentioned in the section of KGM characterization (2.1), all the peaks observed and described, related with KGM, are in accordance with the literature [73]. Regarding SAC0 and KGM-SAC0, the peaks observed are in concordance with the ones described in the literature for the appearance of the functional groups described above [99]–[105].

### 3.1.2 KGM-SAC0 dopamine coupling

After successful incorporation of SAC0 in the polymer backbone, we proceeded to the functionalization of KGM with Dopamine. The carboxylated product KGM-SAC0 reacted with the primary amine present in the Dopamine structure through carbodiimide chemistry. This reaction involves the activation of carboxylic moiety through EDC/NHS followed by nucleophilic attack from the primary amine of the dopamine to the activated ester ending in the formation of an amide bond (Figure 33B).

The success of this reaction was demonstrated by $^{1}$H NMR (Figure 36), through the appearance of new peaks corresponding to characteristic protons of Dopamine (Figure 36B). Between them, it is important to highlight the appearance of three peaks at 8.82 ppm, 6.96 ppm and 6.71 ppm attributed to the hydrogens 14,17 and 18 from the aromatic ring of dopamine molecule; and 2 peaks at 3.27 ppm and 2.92 ppm characteristic of hydrogens 12 and 13 from the aliphatic chain of the dopamine molecule.

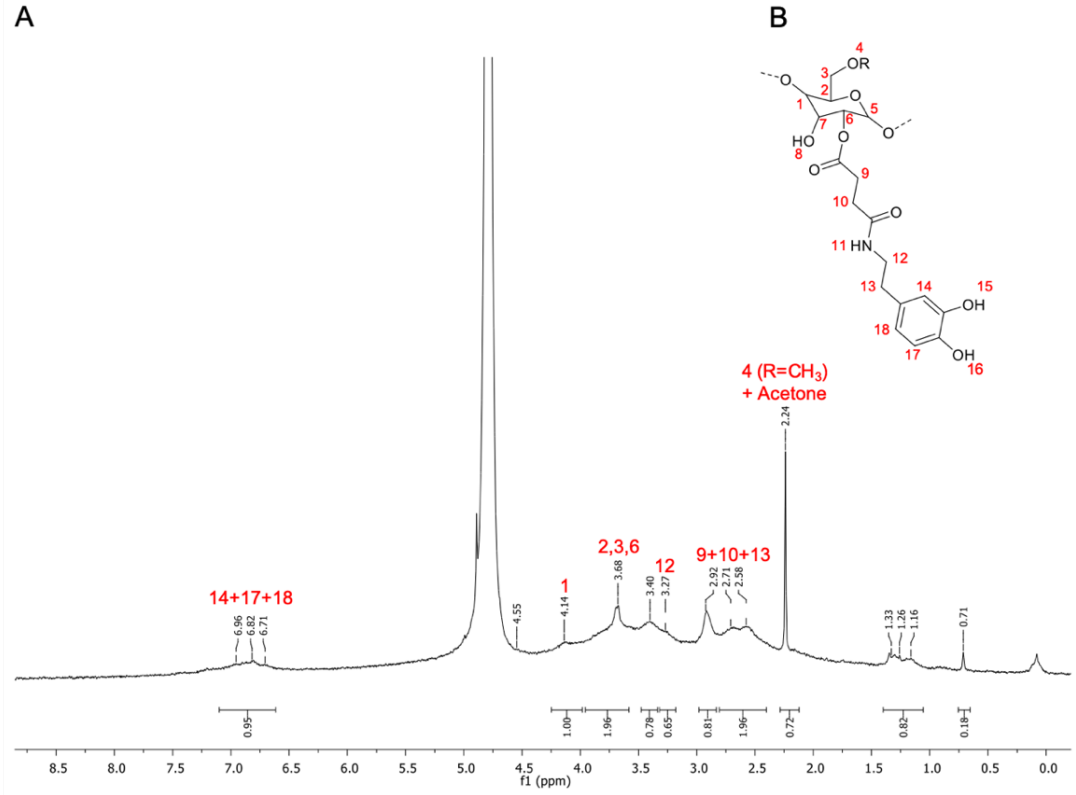


**Figure 36- Incorporation of Dopamine through analysis of $^{1}$H-NMR.** A) KGM-SAC0-Dopamine spectrum in $D_2O$. Visualization and identification of peaks corresponding to hydrogens of the glycosidic unit of the main monomer of KGM, to hydrogens of the aliphatic chain due to presence of the SAC0 molecule (hydrogens 9 and 10) and to protons of the aromatic ring of the Dopamine molecule (hydrogens 14, 17 and 18). Moreover, peaks of the protons corresponding to the aliphatic chain of the Dopamine molecule are also visible (hydrogens 12 and 13). B) Chemical structure of the conjugated KGM-SCA0-Dopamine.

Through the comparison of the integrals of hydrogens 14,17 and 18 from the aromatic ring with the integral of hydrogen 1 from monomeric unit of KGM, it was possible calculate the percentage of Dopamine incorporated on the compound. It was determined that 24% of dopamine could be successfully conjugated to the KGM polymer backbone (Determination of conjugation efficiency on Supplementary material). Around 24% of dopamine has been conjugated to the polymer, which considering the 27% of carboxylic groups available for reaction means an 88% reaction yield. This means a very good coupling efficiency, taking into account that carbodiimide coupling is sensitive to water and provides most of the times low reaction yields [106].

The success of this conjugation was also confirmed by ATR-FTIR (Figure 37).

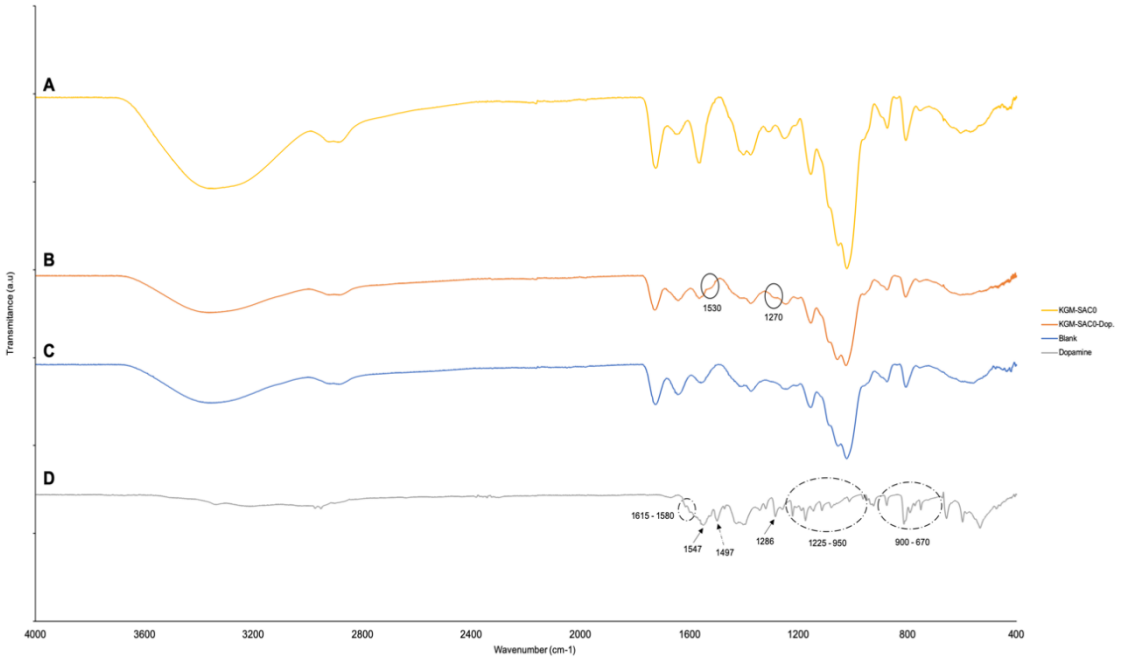


**Figure 37 - Incorporation of Dopamine through analysis of ATR-FTIR.** ATR-FTIR spectrum of KGM-SAC0 (A), KGM-SAC0-Dopamine (B), Blank of the coupling reaction between KGM-SAC0 (C) and dopamine (D) are plotted on the same graph. In relation to the spectrum of KGM-SAC0 and the blank of the coupling reaction on the KGM-SAC0-Dopamine spectrum are visible two shoulders. These shoulders correspond to two peaks of highest intensity on the Dopamine molecule – full arrows on the dopamine spectrum.

In the spectrum of the functionalized polymer KGM-SAC0-Dopamine it was possible to observe the appearance of two shoulders at 1530 $cm^{-1}$ corresponding to combination of N-H bending vibration and C-N stretching vibration in secondary amides, and at 1270 $cm^{-1}$ characteristic of C-O stretching vibration in phenols (Figure 37B-circles), which can be compared with the two

most intense peaks appearing in the dopamine spectrum at 1547 $cm^{-1}$, corresponding to N-H bending vibration in amines, and at 1286 $cm^{-1}$ assigned to C-OH stretching vibration in phenols (Figure 37D-full arrows). Such peaks are absent in the KGM-SAC0 and in the blank of the reaction performed in parallel. This highlights the successful incorporation of dopamine in the polymer backbone.

In the Dopamine spectrum (Figure 37D-circles) it was also possible to observe additional characteristic peaks of the molecule, which appear in the region1615 $cm^{-1}$-1580 $cm^{-1}$ and at 1497 $cm^{-1}$, corresponding to C=C-C stretching vibration in aromatic ring, and in the range 1225 $cm^{-1}$-950 $cm^{-1}$, related with C-N stretching vibration in primary amines. Finally, peaks in the region between 900 $cm^{-1}$ and 670 $cm^{-1}$ are related with C-H bending vibration in aromatics. All the peaks described in both techniques, $^{1}$H-NMR and ATR-FTIR, are in accordance with values reports in the literature [105], [107]–[109].

Although differences in the ATR-FTIR spectrum were not so clear in comparison with the starting compound KGM-SAC0, the appearance of new peaks in the aromatic region of KGM-SAC0-Dopamine $^{1}$H-NMR spectrum allowed to conclude that dopamine has been successfully incorporated on the polymer backbone. The functionalization of this polymer with dopamine provides an important material for the development of hybrid organic-inorganic scaffolds with dual regenerative/therapeutic effect.

## 3.2. Synthesis of Polydopamine particles

The synthesis of polydopamine particles was achieved through alkaline polymerization of dopamine hydrochloride. Polydopamine particles were characterized by TEM (Figure 38). It was possible to observe that the particles exhibited spherical shape with a diameter around 150 nm.

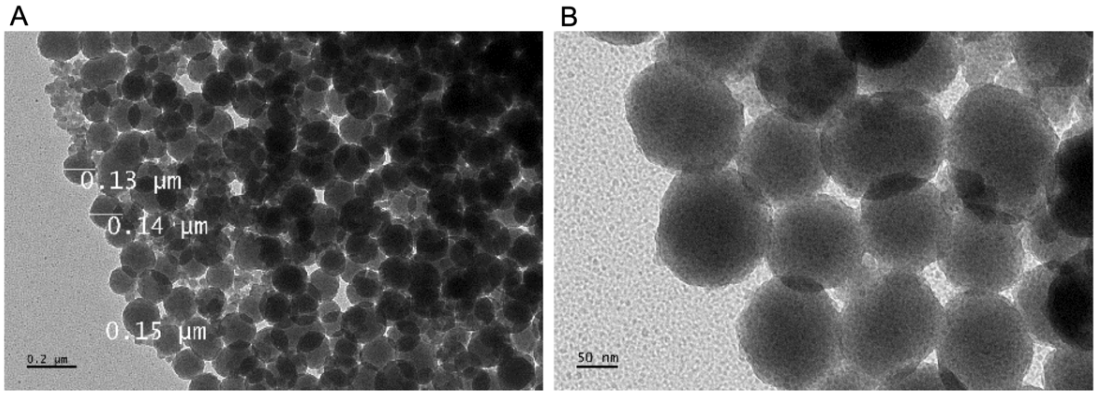


**Figure 38- TEM images of Polydopamine particles at different scales.** On the images it is possible to observe a perfect spherical shape of the particles. A mean value of 150 nm was calculated through analysis of the imagens. Scale bars: A) 0.2 µm; B) 50 nm.

The mean value of the diameter of particles is in accordance, or inclusively is lower, to some works reported in the literature which followed the same protocol [57], [110]. The value of the diameter is good for the use of the particles in the formulation of an ink to be extruded by a robocasting. The nozzle has a diameter of 410 µm, so the particles do not clog the nozzle and the ink can be extruded.

By UV-Vis spectroscopy it was possible to see that the synthetized particles (Figure 39) exhibit a strong optical absorption in the NIR region (600 to 1000 nm). Dilution (1:3) of the particles solution suggest a proportional relationship between absorbance and concentration.

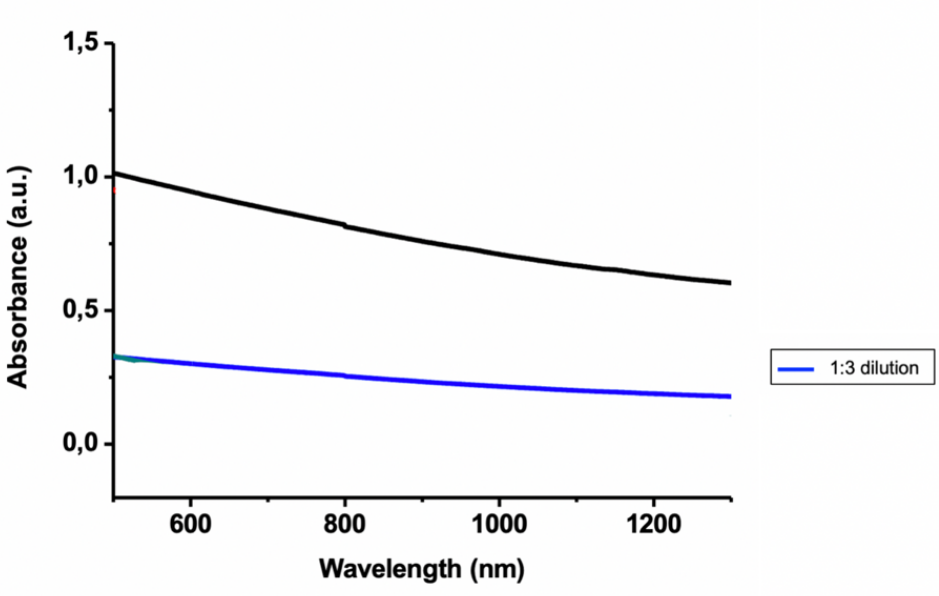


**Figure 39 - Uv-Vis spectrum of Polydopamine particles.** Through the analysis of the spectrum it is possible to see a good absorbance capacity of the particle in the NIR region (600 to 1000 nm). A dilution of the solution is accompanied by a decrease on the absorbance capacity of the particles.

This strong absorbance of this particles in the NIR region (λ= 600-1000 nm) opens good perspectives to their use as promising agents for photothermal cancer therapy. The photothermal therapy employs photosensitizing agents to generate heat at the target sites. Such agents should have ability to absorb light and convert it into heat. To avoid damaging healthy cells effectively, photosensitizing agents must have high absorption in the NIR region of the electromagnetic spectrum, owing to both the deep penetration of NIR and its low absorption by tissues [57]. However, an evaluation of their photothermal conversion capability should be performed. The conversion of light into heat has to be done rapidly, preventing exposure of the tissues to radiation for long time periods, which might damage the healthy cells [57]. In this perspective, additional assays are being carried out. In conclusion, we have successfully synthesized spherical polydopamine particles that could absorb in the NIR region. The synthetized particles seem to be promising photosensitizing agents, but more characterization have to be done in order to ensure that the particles are safe and good agents to be used in photothermal therapy.

The obtained results are very important since the objective, in both strategies, was the use of dopamine as a photosensitive agent to induce a hyperthermia therapeutic effect on the regions affected by a tumor mass,

promoted by the irradiation of the affected areas with a laser emitting on the NIR region. Dopamine has attractive properties in comparison with other agents [28], [57]. Finally, the preferential choice of the photothermal therapy is related with the high selectivity and minimal invasiveness of this therapy. Moreover, its therapeutic effects occur only at the tumor sites, provided by the accumulation of the photothermal therapeutic agent and localized NIR laser irradiation, avoiding the risks of killing normal cells, destruction of the immune system, and preventing the appearance of derived cancers.

# Conclusions and Future work

In the first approach explored in this work, the MNPs scaffolds, the results did not allow the validation of the strategy proposed of the induction of beneficial effects on hMSC culture and differentiation in the presence of MNPs, iron ions or static magnetic field presence since it wasn't possible to establish any influence of a magnetic field on the hMSCs metabolic activity, ECM production or differentiation. The results suggest a positive influence of the iron ions in the proliferation of hMSCs. However, as future work more differentiation assays have to be performed to allow any conclusions about the influence of the application of a magnetic field on the differentiation of hMSCs. In addition, other experiments are also crucial to rule out possible experimental errors that led to conflicting results, particularly in the assay of metabolic cell activity.

As was mentioned previously, these scaffolds showed a poor stability under culture medium conditions and the manipulation is extremely difficult leading to sample loss which is expensive and time consuming. Alternative crosslinking methods to genipin could be an alternative to increase the robustness of the MNPs scaffolds or even post-processing methodologies could allow the production of scaffolds with better outcomes. According to literature available, an alternate magnetic field could be more effective, but at the time of the execution of this work, no such system was available. The development of these scaffolds was assessed in this thesis for bone regeneration proposes evaluating hMSC behavior parameters but the induction of magnetothermal properties was not assessed.

The inconclusive results obtained in the first part of this thesis led us to develop a new approach– the use of KGM as the polymeric base of the scaffold. To the best of our knowledge, no previous 3D printed scaffolds were produced using KGM and this represents an interesting output of this thesis.

With all the characterization made in this work, KGM shows to have quite attractive features. Its high molecular weight and the excellent gelation properties enhance the potential of this natural polysaccharide to be applied on tissue engineering, namely BTE. KGM seems to have optimal properties to obtain a good structural base for the ink and achieve good rheological properties. In fact,

KGM acts as a good “carrier” of the powders which led to a formulation with the desirable characteristics to be used on robocasting technique.

The powders used showed to have the adequate particle size and particle size distribution to be possible achieve an “extrudable” and “printable” ink. Moreover, one more time, they seem to be the optimal choice to bone regeneration, with literature supporting the hMSCs differentiation stimulating effect of the biphasic powders used in this study.

Having a good base solution and powder with adequate properties, the obtained formulation/ink showed to be optimal to be used in the robocasting technique. With that, stable structures with enhanced mechanical properties could be obtained.

With this work, it was demonstrated that we successfully developed hybrid organic-inorganic scaffolds suitable for BTE. They show attractive characteristics such as cytocompatibility, stability under culture medium conditions (being a manageable material, with no samples lost upon manipulation), which can be correlated with the good ink formulation achieved (the scaffolds don’t suffer a high shrinkage and maintain their structure) and adequate pore size to promote the hMSCs adhesion and proliferation, vascularization, and bone formation inside the scaffold. This 500 μm macroporosity is also able to provide transport pathways for nutrients, oxygen, and wastes necessary to maintain living cells within the scaffold. Moreover, their composition is free of organic compounds (such as proteins) and crosslinking agents, being easy and cheap of obtain.

In relation to the osteogenic differentiation more assays need to be done in order to optimize different procedures. For now, the scaffolds seem to have potential to induce the differentiation of hMSCs in osteoblast, but more data, namely biochemical results, are necessary to validate this property. However, with the studies carried out, the scaffolds already show a great potential for future investment in their optimization, namely in the validation of a material to be used in BTE. Further characterizations of the KGM scaffolds are needed such as degradation studies, compressive strength and viscoelastic properties measurements in dry and wet states.

Differentiation into the osteogenic lineage must be well characterized, using ALP enzymatic assays, gene expression, mineralization assays.

*In vitro* tests with osteoblasts and co-cultures of cells (namely bone cancer and osteoblast cells) - in order to simulate the environment in a bone tissue affected by a tumor - are also necessary to verify the effect of the scaffolds on already differentiated cells and if there is any kind of positive effect when in a co-culture situation.

In addition, as they are sintering-free scaffolds, the future will make these scaffolds even more attractive by enriching them with other components. We already started the development of approaches to functionalize KGM with dopamine and the production of polydopamine particles. As the strategy of incorporate dopamine in the KGMs' structure was concluded with success and the production of the polydopamine particles seems to be well executed and the results seem promising, in the future it will be possible to have two different approaches in a scaffold with photosensitive properties.

However, validating both approaches as safe and efficient photosensitive strategies is the first step to follow. Investing in particle characterization, studying their conversion rate, are the first tasks to accomplish. A scale up of the reaction of functionalization of KGM with dopamine will also be necessary, making the procedure more robust, faster and cheaper.

As stated in this thesis, the appearance of localized infections at the bone tumor site, fractures with prolonged healing times is quite common. For this reason, incorporation of drugs, growth factors, among other agents is also an attractive perspective for KGM scaffolds.

# References


[1] OpenStax, *Anatomy and Physiology*. OpenStax, 2013.

[2] R. Florencio-Silva, G. R. D. S. Sasso, E. Sasso-Cerri, M. J. Simões, and P. S. Cerri, "Biology of Bone Tissue: Structure, Function, and Factors That Influence Bone Cells," *Biomed Res. Int.*, vol. 2015, 2015.

[3] J. P. Bilezikian, L. G. Raisz, and T.J. Martin, "Principles of Bone Biology," *3rd Ed. Acad. Press*, 2008.

[4] C. Gao, S. Peng, P. Feng, and C. Shuai, "Bone biomaterials and interactions with stem cells," *Bone Res.*, vol. 5, no. October, pp. 1–33, 2017.

[5] A. S. Mistry and A. G. Mikos, "Tissue Engineering Strategies for Bone Regeneration BT - Regenerative Medicine II: Clinical and Preclinical Applications," pp. 1–22, 2005.

[6] D. Sommerfeldt and C. Rubin, "Biology of bone and how it orchestrates the form and function of the skeleton," *Eur. Spine J.*, vol. 10, no. SUPPL. 2, pp. 86–95, 2001.

[7] D. King, "Bone Remodelling," 2004. .

[8] P. A. Downey and M. I. Siegel, "Bone biology and the clinical implications for osteoporosis," *Phys. Ther.*, vol. 86, no. 1, pp. 77–91, 2006.

[9] Y. Shiwaku *et al.*, "The crosstalk between osteoclasts and osteoblasts is dependent upon the composition and structure of biphasic calcium phosphates," *PLoS One*, vol. 10, no. 7, pp. 1–17, 2015.

[10] J. Green, S. Schotland, D. J. Stauber, C. R. Kleeman, and T. L. Clemens, "Cell-matrix interaction in bone: Type I collagen modulates signal transduction in osteoblast-like cells," *Am. J. Physiol. - Cell Physiol.*, vol. 268, no. 5 37-5, 1995.

[11] R. Zohar, "Signals Between Cells and Matrix Mediate Bone Regeneration," *Bone Regen.*, vol. 7, 2012.

[12] S. Uzawa *et al.*, "Spindle Pole Body Duplication in Fission Yeast Occurs at the G1/S Boundary but Maturation Is Blocked until Exit," *Mol. Biol. Cell*, vol. 15, no. December, pp. 5219–5230, 2004.

[13] Y. Wang, L. M. McNamara, M. B. Schaffler, and S. Weinbaum, "A model for the role of integrins in flow induced mechanotransduction in

osteyocytes," *Bioeng. Proc. Northeast Conf.*, vol. 104, no. 40, pp. 39–40, 2007.

[14] A. G. Robling, A. B. Castillo, and C. H. Turner, "Biomechanical and Molecular Regulation of Bone Remodeling," *Annu. Rev. Biomed. Eng.*, vol. 8, no. 1, pp. 455–498, 2006.

[15] K. Kapinas and A. M. Delany, "MicroRNA biogenesis and regulation of bone remodeling," *Arthritis Res. Ther.*, vol. 13, no. 3, pp. 1–11, 2011.

[16] Y. Shiwaku, K. Tsuchiya, L. Xiao, and O. Suzuki, "Effect of calcium phosphate phases affecting the crosstalk between osteoblasts and osteoclasts in vitro," *J. Biomed. Mater. Res. - Part A*, pp. 1001–1013, 2019.

[17] T. C. A. Phan, J. Xu, and M. H. Zheng, "Interaction between osteoblast and osteoclast: Impact in bone disease," *Histol. Histopathol.*, vol. 19, no. 4, pp. 1325–1344, 2004.

[18] L. B. Michaud and S. Goodin, "Cancer-treatment-induced bone loss, part 1," *Am. J. Heal. Pharm.*, vol. 63, no. 5, pp. 419–430, 2006.

[19] E. Verron, H. Schmid-Antomarchi, H. Pascal-Mousselard, A. Schmid-Alliana, J. C. Scimeca, and J. M. Bouler, "Therapeutic strategies for treating osteolytic bone metastases," *Drug Discov. Today*, vol. 19, no. 9, pp. 1419–1426, 2014.

[20] E. Jimi, S. Hirata, K. Osawa, M. Terashita, C. Kitamura, and H. Fukushima, "The current and future therapies of bone regeneration to repair bone defects," *Int. J. Dent.*, no. March, 2012.

[21] R. G.A. and M. T.J., "Therapeutic Approaches to Bone Diseases," *Science (80-. ).*, vol. 289, no. September, pp. 1508–1514, 2000.

[22] J. A. Sterling and S. A. Guelcher, "Biomaterial Scaffolds for Treating Osteoporotic Bone," *Curr. Osteoporos. Rep.*, vol. 12, no. 1, pp. 48–54, Mar. 2014.

[23] F. D. Cojocaru, V. Balan, I. M. Popa, A. Munteanu, A. Anghelache, and L. Verestiuc, "Magnetic Composite Sca olds for Potential Applications in Radiochemotherapy of Malignant Bone Tumors," *Medicina (B. Aires).*, vol. 55, no. 153, pp. 1–14, 2019.

[24] G. Falkowski, "Prevent Osteoporosis with 6 Bone Health Boosters," 2016. [Online]. Available: https://msfocus.org/Magazine/Magazine-

Items/Prevent-Osteoporosis-with-6-Bone-Health-Boosters.

[25] Y. Zhang, D. Zhai, M. Xu, Q. Yao, J. Chang, and C. Wu, “3D-printed bioceramic scaffolds with a Fe3O4/graphene oxide nanocomposite interface for hyperthermia therapy of bone tumor cells,” *J. Mater. Chem. B*, vol. 4, no. 17, pp. 2874–2886, 2016.

[26] H. Ma *et al.*, “A Bifunctional Biomaterial with Photothermal Effect for Tumor Therapy and Bone Regeneration,” *Adv. Funct. Mater.*, vol. 26, no. 8, pp. 1197–1208, 2016.

[27] H. Wang *et al.*, “Biocompatibility and osteogenic capacity of borosilicate bioactive glass scaffolds loaded with Fe3O4 magneticmagnetic nanoparticles,” *J. Mater. Chem. B*, vol. 3, no. 21, pp. 4377–4387, 2015.

[28] H. Ma *et al.*, “3D printing of biomaterials with mussel-inspired nanostructures for tumor therapy and tissue regeneration,” *Biomaterials*, vol. 111, pp. 138–148, 2016.

[29] T. P. Cloake and L. M. Jeys, “How important are surgical margins in Osteosarcoma?,” *J. Bone Soft Tissue Tumors*, vol. 2, no. 1, pp. 22–26, 2016.

[30] R. Dimitriou, E. Jones, D. McGonagle, and P. V Giannoudis, “Bone regeneration: current concepts and future directions,” *BMC Med.*, vol. 9, no. 66, pp. 1–10, 2011.

[31] S. M. Olhero, H. R. Fernandes, C. F. Marques, B. C. G. Silva, and J. M. F. Ferreira, “Additive manufacturing of 3D porous alkali-free bioactive glass scaffolds for healthcare applications,” *J. Mater. Sci.*, vol. 52, no. 20, pp. 12079–12088, 2017.

[32] J. R. Perez, D. Kouroupis, D. J. Li, T. M. Best, L. Kaplan, and D. Correa, “Tissue Engineering and Cell-Based Therapies for Fractures and Bone Defects,” *Front. Bioeng. Biotechnol.*, vol. 6, no. July, pp. 1–23, 2018.

[33] T. Matsuno, K. Omata, Y. Hashimoto, Y. Tabata, and T. Satoh, “Alveolar bone tissue engineering using composite scaffolds for drug delivery,” *Jpn. Dent. Sci. Rev.*, vol. 46, no. 2, pp. 188–192, 2010.

[34] M. Schicker, H. Seitz, I. Drosse, S. Seitz, and W. Mutschler, “Biomaterials as scaffold for bone tissue engineering,” *Eur. J. Trauma*, vol. 32, no. 2, pp. 114–124, 2006.

[35] Q. Fu, E. Saiz, M. N. Rahaman, and A. P. Tomsia, “Toward strong and

tough glass and ceramic scaffolds for bone repair," *Adv. Funct. Mater.*, vol. 23, no. 44, pp. 5461–5476, 2013.

[36] S. Ioan and L. I. Buruiana, "Biodegradable polymers in tissue engineering," *Handb. Compos. from Renew. Mater.*, vol. 1–8, no. September, pp. 145–182, 2017.

[37] C. Z. Liu and J. T. Czernuszka, "Development of biodegradable scaffolds for tissue engineering: A perspective on emerging technology," *Mater. Sci. Technol.*, vol. 23, no. 4, pp. 379–391, 2007.

[38] J. J. Li, D. L. Kaplan, and H. Zreiqat, "Scaffold-based regeneration of skeletal tissues to meet clinical challenges," *J. Mater. Chem. B*, vol. 2, no. 42, pp. 7272–7306, 2014.

[39] B. TW, "Bone graft materials. An overview of the basic science.," *Clin. Orthop. Relat. Res.*, vol. 37, pp. 10–27, 2000.

[40] R. A. Revia and M. Zhang, "Magnetite nanoparticles for cancer diagnosis, treatment, and treatment monitoring: Recent advances," *Mater. Today*, vol. 19, no. 3, pp. 157–168, 2016.

[41] Y. Wu *et al.*, "A novel calcium phosphate ceramic-magnetic nanoparticle composite as a potential bone substitute," *Biomed. Mater.*, vol. 5, no. 1, 2010.

[42] E. Feilden, *Additive manufacturing of ceramics and ceramic composites via robocasting*. 2017.

[43] E. Feilden, E. G. T. Blanca, F. Giuliani, E. Saiz, and L. Vandeperre, "Robocasting of structural ceramic parts with hydrogel inks," *J. Eur. Ceram. Soc.*, vol. 36, no. 10, pp. 2525–2533, 2016.

[44] C. Shi, Z. Yuan, F. Han, C. Zhu, and B. Li, "Polymeric biomaterials for bone regeneration," *Ann. Jt.*, vol. 1, pp. 27–27, 2016.

[45] X. Chen, Q. Chen, T. Yan, and J. Liu, "Characterization of konjac glucomannan-gelatin IPN physical hydrogel scaffold," *IOP Conf. Ser. Mater. Sci. Eng.*, vol. 207, no. 1, 2017.

[46] X. Du, S. Fu, and Y. Zhu, "3D printing of ceramic-based scaffolds for bone tissue engineering: An overview," *J. Mater. Chem. B*, vol. 6, no. 27, pp. 4397–4412, 2018.

[47] N. C. Silva, S. Silva, B. Sarmento, and M. Pintado, "Chitosan nanoparticles for daptomycin delivery in ocular treatment of bacterial

endophthalmitis," *Drug Deliv.*, vol. 22, no. 7, pp. 885–893, 2015.

[48] R. Chi, F. Cheung, T. B. Ng, J. H. Wong, and W. Y. Chan, *Chitosan: An Update on Potential Biomedical and Pharmaceutical Applications*. 2015.

[49] J. Tang, J. Chen, J. Guo, Q. Wei, and H. Fan, "Construction and evaluation of fibrillar composite hydrogel of collagen/konjac glucomannan for potential biomedical applications," *Regen. Biomater.*, vol. 5, no. 4, pp. 239–250, 2018.

[50] C. Wu *et al.*, "Preparation and characterization of konjac glucomannan-based bionanocomposite film for active food packaging," *Food Hydrocoll.*, vol. 89, pp. 682–690, 2019.

[51] Z. Gang *et al.*, "The study of tri-phasic interactions in nano-hydroxyapatite/konjac glucomannan/chitosan composite," *J. Mater. Sci.*, vol. 42, no. 8, pp. 2591–2597, 2007.

[52] L. Huang, R. Takahashi, S. Kobayashi, T. Kawase, and K. Nishinari, "Gelation behavior of native and acetylated konjac glucomannan," *Biomacromolecules*, vol. 3, no. 6, pp. 1296–1303, 2002.

[53] D. Yang *et al.*, "A review on konjac glucomannan gels: Microstructure and application," *Int. J. Mol. Sci.*, vol. 18, no. 11, 2017.

[54] B. Hildebrandt *et al.*, "The cellular and molecular basis of hyperthermia," *Crit. Rev. Oncol. Hematol.*, pp. 33–56, 2002.

[55] F. K. Storm, W. H. Harrison, and R. S. Elliott, "Normal Tissue and Solid Tumor Effects of Hyperthermia in Animal Models and Clinical Trials," *Cancer Res.*, vol. 39, no. June, pp. 2245–2251, 1979.

[56] J. van der Zee, "Heating the patient: A promising approach?," *Ann. Oncol.*, vol. 13, no. 8, pp. 1173–1184, 2002.

[57] Y. Liu, K. Ai, J. Liu, M. Deng, Y. He, and L. Lu, "Dopamine-melanin colloidal nanospheres: An efficient near-infrared photothermal therapeutic agent for in vivo cancer therapy," *Adv. Mater.*, vol. 25, no. 9, pp. 1353–1359, 2013.

[58] S. Bose, G. Fielding, S. Tarafder, and A. Bandyopadhyay, "Understanding of dopant-induced osteogenesis and angiogenesis in calcium phosphate ceramics," *Trends Biotechnol.*, vol. 31, no. 10, pp. 594–605, 2013.

[59] E. Boanini, M. Gazzano, and A. Bigi, "Ionic substitutions in calcium phosphates synthesized at low temperature," *Acta Biomater.*, vol. 6, no. 6,

pp. 1882–1894, 2010.

[60] A. Catarina, “Desenho e Processamento de Estruturas Porosas de Fosfatos de Cálcio por Robocasting para Engenharia de Tecido Ósseo Design and processing of porous scaffolds based on calcium phosphates by robocasting for bone tissue engineering Fernandes Marques Desenho ,” 2017.

[61] Y. J. Seol, T. Y. Kang, and D. W. Cho, “Solid freeform fabrication technology applied to tissue engineering with various biomaterials,” *Soft Matter*, vol. 8, no. 6, pp. 1730–1735, 2012.

[62] E. Sachlos and J. T. Czernuszka, “Making tissue engineering scaffold work. Review on the application of solid freeform fabrication technology to the production of tissue engineering scaffolds,” *Eur. Cells Mater.*, vol. 5, pp. 29–40, 2003.

[63] E. L. W. de Mulder, P. Buma, and G. Hannink, “Anisotropic porous biodegradable scaffolds for musculoskeletal tissue engineering,” *Materials (Basel).*, vol. 2, no. 4, pp. 1674–1696, 2009.

[64] D. W. Hutmacher, “Scaffold designed fabrication technologies for engineering tissues-state of art and future perspectives,” *J Biomater. Sci. Polym. Ed.*, vol. 12, no. 1, pp. 107–124, 2001.

[65] Y.-J. Seol, T.-Y. Kang, and D.-W. Cho, “Solid freeform fabrication technology applied to tissue engineering with various biomaterials,” *R. Soc. ofChemistry, Soft matter*, vol. 8, pp. 1730–1735, 2012.

[66] A. Gleadall, D. Visscher, J. Yang, D. Thomas, and J. Segal, “Review of additive manufactured tissue engineering scaffolds: relationship between geometry and performance,” *Burn. Trauma*, vol. 6, no. 1, pp. 1–16, 2018.

[67] C. F. Marques *et al.*, “Novel sintering-free scaffolds obtained by additive manufacturing for concurrent bone regeneration and drug delivery: Proof of concept,” *Mater. Sci. Eng. C*, vol. 94, no. March 2018, pp. 426–436, 2019.

[68] T. P. Chen, T. Liu, T. L. Su, and J. Liang, “Self-polymerization of dopamine in acidic environments without oxygen,” *Langmuir*, vol. 33, no. 23, pp. 5863–5871, 2017.

[69] Z. Hedayatnasab, F. Abnisa, and W. M. A. W. Daud, “Review on magnetic nanoparticles for magnetic nanofluid hyperthermia application,”

*Mater. Des.*, vol. 123, pp. 174–196, 2017.

[70] A. Roy, J. A. De Toro, V. S. Amaral, P. Muniz, J. M. Riveiro, and J. M. F. Ferreira, “Exchange bias beyond the superparamagnetic blocking temperature of the antiferromagnet in a Ni-NiO nanoparticulate system,” *J. Appl. Phys.*, vol. 115, no. 7, 2014.

[71] C. F. Marques *et al.*, “Biphasic calcium phosphate scaffolds fabricated by direct write assembly: Mechanical, anti-microbial and osteoblastic properties,” *J. Eur. Ceram. Soc.*, vol. 37, no. 1, pp. 359–368, 2017.

[72] L. Malaval, F. Liu, P. Roche, and J. E. Aubin, “Kinetics of osteoprogenitor proliferation and osteoblast differentiation in vitro,” *J. Cell. Biochem.*, vol. 74, no. 4, pp. 616–627, 1999.

[73] S. Wang, B. Zhou, Y. Wang, and B. Li, “Preparation and characterization of konjac glucomannan microcrystals through acid hydrolysis,” *Food Res. Int.*, vol. 67, pp. 111–116, 2015.

[74] B. Xia *et al.*, “Preparation and characterization of a poly(ethylene glycol) grafted carboxymethyl konjac glucomannan copolymer,” *Carbohydr. Polym.*, vol. 79, no. 3, pp. 648–654, 2010.

[75] E. Audebeau, E. K. Oikonomou, S. Norvez, and I. Iliopoulos, “One-pot synthesis and gelation by borax of glycopolymers in water,” *Polym. Chem.*, vol. 5, no. 7, pp. 2273–2281, 2014.

[76] L. Ji, Y. Xue, D. Feng, Z. Li, and C. Xue, “Morphology and gelation properties of konjac glucomannan: Effect of microwave processing,” *Int. J. Food Prop.*, vol. 20, no. 12, pp. 3023–3032, 2017.

[77] C. Wang, M. Xu, W. Lv, P. Qiu, Y. Gong, and D. Li, “Study on Rheological Behavior of Konjac Glucomannan,” *Phys. Procedia*, vol. 33, pp. 25–30, 2012.

[78] H. Ye, X. Y. Liu, and H. Hong, “Characterization of sintered titanium/hydroxyapatite biocomposite using FTIR spectroscopy,” *J. Mater. Sci. Mater. Med.*, vol. 20, no. 4, pp. 843–850, 2009.

[79] L. Berzina-Cimdina and N. Borodajenko, “Research of Calcium Phosphates Using Fourier Transform Infrared Spectroscopy,” in *Infrared Spectroscopy - Materials Science, Engineering and Technology*, vol. 6, 2012, pp. 123–148.

[80] A. Jillavenkatesa and R. A. Condrate, “The Infrared and Raman Spectra

of β-and α-Tricalcium Phosphate (Ca3(Po4)2)," *Spectrosc. Lett. An Int. J. Rapid Commun.*, vol. 31, no. 8, pp. 1619–1634, 2006.

[81] K. Ogata *et al.*, "Comparison of osteoblast responses to hydroxyapatite and hydroxyapatite/soluble calcium phosphate composites," *J. Biomed. Mater. Res. - Part A*, vol. 72, no. 2, pp. 127–135, 2005.

[82] M. Bohner and J. Lemaitre, "Can bioactivity be tested in vitro with SBF solution?," *Biomaterials*, vol. 30, no. 12, pp. 2175–2179, 2009.

[83] J. Franco, P. Hunger, M. E. Launey, A. P. Tomsia, and E. Saiz, "Direct write assembly of calcium phosphate scaffolds using a water-based hydrogel," *Acta Biomater.*, vol. 6, no. 1, pp. 218–228, 2010.

[84] M. Faes, H. Valkenaers, F. Vogeler, J. Vleugels, and E. Ferraris, "Extrusion-based 3D printing of ceramic components," *Procedia CIRP*, vol. 28, pp. 76–81, 2015.

[85] M. Khatibi, N. Potokin, and R. W. Time, "Experimental investigation of effect of salts on rheological properties of non-Newtonian fluids," *Nord. Rheol. Soc.*, vol. 24, no. May, 2016.

[86] B. A. E. Ben-Arfa, A. S. Neto, I. M. Miranda Salvado, R. C. Pullar, and J. M. F. Ferreira, "Robocasting: Prediction of ink printability in solgel bioactive glass," *J. Am. Ceram. Soc.*, vol. 102, no. 4, pp. 1608–1618, 2019.

[87] C. J. Wilson, R. E. Clegg, D. I. Leavesley, and M. J. Pearcy, "Mediation of biomaterial-cell interactions by adsorbed proteins: A review," *Tissue Eng.*, vol. 11, no. 1–2, pp. 1–18, 2005.

[88] V. Karageorgiou and D. Kaplan, "Porosity of 3D biomaterial scaffolds and osteogenesis," *Biomaterials*, vol. 26, no. 27, pp. 5474–5491, 2005.

[89] M. Persson *et al.*, "Osteogenic Differentiation of Human Mesenchymal Stem cells in a 3D Woven Scaffold," *Sci. Rep.*, vol. 8, no. 1, pp. 1–12, 2018.

[90] L. Zhang *et al.*, "Porous hydroxyapatite and biphasic calcium phosphate ceramics promote ectopic osteoblast differentiation from mesenchymal stem cells," *Sci. Technol. Adv. Mater.*, vol. 10, no. 2, 2009.

[91] F. N. Syed-Picard, G. A. Shah, B. J. Costello, and C. Sfeir, "Regeneration of periosteum by human bone marrow stromal cell sheets," *J. Oral Maxillofac. Surg.*, vol. 72, no. 6, pp. 1078–1083, 2014.

[92] Y. Li, W. Weng, and K. C. Tam, “Novel highly biodegradable biphasic tricalcium phosphates composed of α-tricalcium phosphate and β-tricalcium phosphate,” *Acta Biomater.*, vol. 3, no. 2, pp. 251–254, 2007.

[93] M. Cicuéndez, M. Malmsten, J. C. Doadrio, M. T. Portolés, I. Izquierdo-Barba, and M. Vallet-Regí, “Tailoring hierarchical meso-macroporous 3D scaffolds: From nano to macro,” *J. Mater. Chem. B*, vol. 2, no. 1, pp. 49–58, 2014.

[94] S. N. Rath *et al.*, “Osteoinduction and survival of osteoblasts and bone-marrow stromal cells in 3D biphasic calcium phosphate scaffolds under static and dynamic culture conditions,” *J. Cell. Mol. Med.*, vol. 16, no. 10, pp. 2350–2361, 2012.

[95] H. Hanna, L. M. Mir, and F. M. Andre, “In vitro osteoblastic differentiation of mesenchymal stem cells generates cell layers with distinct properties,” *Stem Cell Res. Ther.*, vol. 9, no. 1, pp. 1–11, 2018.

[96] T. K. P. Goh *et al.*, “Microcarrier culture for efficient expansion and osteogenic differentiation of human fetal mesenchymal stem cells,” *Biores. Open Access*, vol. 2, no. 2, pp. 84–97, 2013.

[97] T. Jiang *et al.*, “Andrographolide exerts pro-osteogenic effect by activation of Wnt/β-catenin signaling pathway in vitro,” *Cell. Physiol. Biochem.*, vol. 36, no. 6, pp. 2327–2339, 2015.

[98] T. Heino and T. Hentunen, “Differentiation of Osteoblasts and Osteocytes from Mesenchymal Stem Cells,” *Curr. Stem Cell Res. Ther.*, vol. 3, no. 2, pp. 131–145, 2008.

[99] M. Falkeborg, P. Paitaid, A. N. Shu, B. Pérez, and Z. Guo, “Dodecenyl succinylated alginate as a novel material for encapsulation and hyperactivation of lipases,” *Carbohydr. Polym.*, vol. 133, pp. 194–202, 2015.

[100] J. D. Sudha and C. K. S. Pillai, “Synthesis and properties of amphotropic hydrogen bonded liquid crystalline (LC) poly(ester amide)s (PEA): Effect of aromatic moieties on LC behavior,” *Polymer (Guildf).*, vol. 46, no. 18, pp. 6986–6997, 2005.

[101] A. A. Ishak and J. Salimon, “Optimization Process for Esterification of Rubber Seed Oil ( RSO ) with Trimethylolpropane ( TMP ),” *J. Sci. Technol.*, vol. 4, pp. 1–10, 2012.

[102] Y. Hase, C. U. Davanzo, K. Kawai, and O. Sala, “The vibrational spectra of phthalic anhydride,” *J. Mol. Struct.*, vol. 30, no. 1, pp. 37–44, 1976.

[103] W. G. Dauben and W. W. Epstein, “Infrared Spectra of Some Cyclic Anhydrides,” *J. Org. Chem.*, vol. 24, no. 10, pp. 1595–1596, 1959.

[104] J. Oomens and J. D. Steill, “Free carboxylate stretching modes,” *J. Phys. Chem. A*, vol. 112, no. 15, pp. 3281–3283, 2008.

[105] F. S. Parker, “Amides and Amines BT - Applications of Infrared Spectroscopy in Biochemistry, Biology, and Medicine,” F. S. Parker, Ed. Boston, MA: Springer US, 1971, pp. 165–172.

[106] J. V. Staros, R. W. Wright, and D. M. Swingle, “Enhancement by N-hydroxysulfosuccinimide of water-soluble carbodiimide-mediated coupling reactions,” *Anal. Biochem.*, vol. 156, no. 1, pp. 220–222, 1986.

[107] T. López *et al.*, “Treatment of parkinson’s disease: Nanostructured sol-gel silica-dopamine reservoirs for controlled drug release in the central nervous system,” *Int. J. Nanomedicine*, vol. 6, no. 1, pp. 19–31, 2011.

[108] A. Lagutschenkov, J. Langer, G. Berden, J. Oomens, and O. Dopfer, “Infrared spectra of protonated neurotransmitters: Dopamine,” *Phys. Chem. Chem. Phys.*, vol. 13, no. 7, pp. 2815–2823, 2011.

[109] H. D. Bist, J. C. D. Brand, and D. R. Williams, “The vibrational spectrum and torsion of phenol,” *J. Mol. Spectrosc.*, vol. 24, no. 1–4, pp. 402–412, 1967.

[110] R. Zheng *et al.*, “Polydopamine-Coated Magnetic Composite Particles with an Enhanced Photothermal Effect,” *ACS Appl. Mater. Interfaces*, vol. 7, no. 29, pp. 15876–15884, 2015.

*Page intentionally left in blank*

# Supplementary material

## 1. Supporting tables of the experiment with MNPs scaffolds

**Table S1 - Statistical analysis of data from Figure 16, for the Influence of the application of an external magnetic field on the Metabolic cell activity**. Statistically significant differences are marked with * ($p < 0.05$), ** ($p < 0.01$), *** ($p < 0.001$) or **** ($p < 0.0001$), ns. means not statistically significant.

| | |
|---|---|
| BMNPs Day 1 basal VS BMNPs w/ magnets Day 1 basal | ns |
| BMNPs Day 21 basal Vs BMNPs w/ magnets Day 21 basal | ns |
| BMNPs Day 1 osteogenic Vs BMNPs w/ magnets Day 1 osteogenic | *** |
| BMNPs Day 21 osteogenic Vs BMNPs w/ magnets Day 21 osteogenic | ns |
| FeMNPs Day 1 basal Vs FeMNPs w/ magnets Day 1 basal | ns |
| FeMNPs Day 21 basal Vs FeMNPs w/ magnets Day 21 basal | ns |
| FeMNPs Day 1 osteogenic Vs FeMNPs w/ magnets Day 1 osteogenic | ns |
| FeMNPs Day 21 osteogenic Vs FeMNPs w/ magnets Day 21 osteogenic | * |

**Table S2 - Statistical analysis of data from Figure 16, for the Influence of iron ions on the Metabolic cell activity**. Statistically significant differences are marked with * ($p < 0.05$), ** ($p < 0.01$), *** ($p < 0.001$) or **** ($p < 0.0001$), ns. means not statistically significant.

| | |
|---|---|
| BMNPs Day 1 basal Vs FeMNPs Day 1 basal | ns |
| BMNPs Day 21 basal Vs FeMNPs Day 21 basal | ns |
| BMNPs Day 1 osteogenic Vs FeMNPs Day 1 osteogenic | ns |
| BMNPs Day 21 osteogenic Vs FeMNPs Day 21 osteogenic | *** |
| BMNPs w/ magnets Day 1 basal Vs FeMNPs w/ magnets Day 1 basal | ns |
| BMNPs w/ magnets Day 21 basal Vs FeMNPs w/ magnets Day 21 basal | ** |
| BMNPs w/ magnets Day 1 osteogenic Vs FeMNPs w/ magnets Day 1 osteogenic | ns |
| BMNPs w/ magnets Day 21 osteogenic Vs FeMNPs w/ magnets Day 21 osteogenic | ns |

## 2. Supporting table of the experiment with KGM scaffolds

**Table S3 - Statistical analysis of data from Figure 28, for the metabolic activity of hMSCs on KGM scaffolds for basal and osteogenic condition**. Statistically significant differences are marked with * ($p < 0.05$), ** ($p < 0.01$), *** ($p < 0.001$) or **** ($p < 0.0001$), ns. means not statistically significant.

| | |
|---|---|
| Day 1 basal Vs Day 14 basal | **** |
| Day 14 basal Vs Day 28 basal | ** |
| Day 1 basal Vs Day 28 basal | **** |
| Day 1 osteogenic Vs Day 14 osteogenic | **** |
| Day 14 osteogenic Vs Day 28 osteogenic | ns |
| Day 1 osteogenic Vs Day 28 osteogenic | **** |
| Day 1 basal Vs Day 1 osteogenic | ns |
| Day 14 basal Vs Day 14 osteogenic | * |
| Day 28 basal Vs Day 28 osteogenic | ns |

## 3. Calculation of the acetylated degree of KGM:

$$Acetylation\ degree\ = \frac{\frac{0{,}26}{3}}{\frac{1{,}00}{1} + \frac{0{,}26}{3}} \times 100 = 8\%$$

## 4. Calculation of the amount of SAC0 incorporated:

$$Conjugation\ Efficiency = \frac{\frac{1{,}48}{4}}{\frac{1{,}00}{1} + \frac{1{,}48}{4}} \times 100 = 27\%$$

## 5. Calculation of the amount of Dopamine incorporated:

$$Conjugation\ Efficiency = \frac{\frac{0{,}95}{3}}{\frac{1{,}00}{1} + \frac{0{,}95}{3}} \times 100 = 24\%$$

*Page intentionally left in blank*